Alma Mater Studiorum
Università degli Studi di Bologna

Dottorato di Ricerca in Fisica
Ciclo XXVI

Laser driven proton acceleration and beam shaping

Settore Concorsuale di Afferenza: 01/A4

Settore Scientifico Disciplinare: MAT/07

Coordinatore: Prof. Fabio Ortolani

Presentata da:
Stefano Sinigardi

Relatore:
Prof. Giorgio Turchetti

Esame Finale Anno Accademico 2012-2013

Contents

Acknowledgements

I am grateful to many people for the help they provided me in these years. My family, my beloved and my friends first of all, but since this is my PhD thesis I think that I should say thanks at the beginning also to the many people I met and I had the honour to work with.

First of all my supervisor, Prof. Giorgio Turchetti, that gave me several suggestions, ideas and guided me during these years of hard work.

Other people here with me now, that I feel grateful to, are Prof. Graziano Servizi and Dr. Pasquale Londrillo. Grazie.

An extremely sincere どうもありがとうございました goes to Prof. Paul Bolton. He has been not just a second supervisor during my months spent in Japan, he was also a great friend and a superlative lunch mate. In Japan I remember also many other friends. When I left, I promised them it was not a farewell, just a goodbye.

I also want to thank Alessandra Lombardi at CERN and all the people I met there belonging to her group. I felt at home there. Also I feel grateful to Prof. Ingo Hofmann, at GSI, that gave me the opportunity to work with some talented people. Danke schön.

Many other people should be thanked, with more words and more passion. Since I hope to have the opportunity to see them in person, as soon as possible, I prefer to be grateful to them with some spoken words. I hope they can understand.

merci, eshghe man ♡

Introduction

Particle accelerators are wonderful instruments. They are used for fundamental physics research and for a variety of applications including medical imaging and radiotherapy. The first accelerators were built in the 30s using electrostatic generators; the merits for the first prototype go to Van de Graaff (1931) [1], followed by works by Cockcroft and Walton [2]. More recent tandem version allowed to double the potential and reached proton energies above 10 MeV.

Higher energies have been reached with the linear accelerators, first proposed by Rolf Widerøe in his thesis [3] where the use of alternating fields and multiple elements on a straight line allowed to overcome the limitations of the electrostatic accelerators.

In parallel, circular accelerators were developed first by Lawrence [4] with his cyclotron (1930), capable of producing a high intensity monoenergetic beam.

In the middle of last century particle accelerators got a substantial boost with the synchrotron, first built by Edwin McMillan (1945) to accelerate electrons. The first synchrotron for protons was designed by Sir Marcus Oliphant and built (1952) , see E. J. N. Wilson for a nice review [5].

Synchrotron are the basic devices for modern ring storage and accelerators, such as the state-of-the-art Large Hadron Collider at CERN, in Geneva. This device is enormous and the largest ring, 27 km, is only the last of a sequence of interconnected smaller rings where the protons or ions energy is progressively increased. At maximum design parameters, 7 TeV protons circulate in the largest ring in both directions and collide with extremely high luminosity. The design of the future TeV electron positron linear colliders (like the International Linear Collider or the Compact LInear Collider), if realized with traditional technology, would be limited by the maximum achievable electric field in conventional cavities ($\sim$ 60 MV/m), so that the length would be several tens of km.

Since the size of and cost of accelerators for high energy physics have been continuously growing and the limits of technical and economical feasibility are almost reached at present, scientists started to look for new technologies to drive particle acceleration.

In this context was born the idea of using lasers. In 1979, Tajima and Dawson wrote a paper [6] in which they proposed the idea of a wake field generated by a light packet within an under-dense plasma. The plasma itself is produced by the laser beam and electron beam are accelerated by the wake field to high energies in very short distances. This idea grew in subsequent years, with also the very famous "Dream Beam" 2004 Nature cover [7, 8, 9].

The most recent achievements, using this technique, are related to multi-GeV electrons production over distanced ranging from a few mm to a few cm [10, 11].

Similar ideas were developed for proton and ion acceleration and in the latest years few tens of MeV protons were produced in different laboratories around the world. Starting from the famous experiment performed by Snavely et al. [12], many other experiments were performed and theoretical models were developed. The Target Normal Sheath Acceleration (TNSA) mechanism, in which the protons are accelerated by the electrostatic field created (by charge separation) by the displaced electrons, is now well established, but is not satisfactory because of the low quality of the produced ions or protons beams. Other mechanisms like Radiation Pressure Acceleration or Magnetic Vortex Acceleration are presently investigated with theoretical modeling, numerical simulations and, whenever possible and technically feasible, also from the experimental point of view. Comprehensive reviews on laser-driven proton acceleration can be found in [13].

In this thesis I will describe the basic aspects of laser plasma interaction for the acceleration of protons and the techniques developed to diagnose and enhance the beam quality. Even though the starting point is based on analytical models, the numerical methods, and the software in which they have been implemented, play a key role to simulate and reproduce laser-plasma acceleration experiments in High Performances Computing (HPC), massively parallel computing environments. At present this is the only way to understand the underlying physical mechanisms and to develop new theoretical models.

The driving line of this thesis will be the study and design of a compact system to extract a high quality beam out of the bunch of protons produced by the interaction of a sub PW laser beam with a thin solid target in the TNSA regime, which is experimentally quite reliable. Such a system would be of interest for applications if the final energy and intensity are sufficiently high. Applications to radiobiology require energies in the 30 MeV range, whereas the threshold of interest for therapy is 60 MeV and the required dose is achieved with $\sim 10^7$ protons per bunch at repetition rate of 10 Hz.

With start to end 3D simulations of acceleration and transport, we will show that a beam with at least 10^8 protons at 30 MeV, having a small energy spread and a small divergence, can be selected from an initial proton bunch generated by a laser beam whose intensity is the $1 - 2\,10^{21}$ W/cm^2 range. This is compatible with some recent experiments. The key idea for beam shaping is to exploit the chromaticity of a magnetic lens, since a collimator placed on the focus of particles with the desired energy allows to select a monochromatic beam.

In this thesis different transport lines are proposed and analyzed. The first is based on a high field solenoid, some collimators and, for perfect filtering and post-acceleration, a high-field high-frequency compact linac originally designed to accelerate a 30 MeV beam extracted from a cyclotron.

The second one is based on a quadruplet of permanent magnetic quadrupoles: thanks to its grater simplicity and reliability, it has a great interest for experiments, but the effectiveness is lower than the one based on the solenoid and the final beam intensity drops by an order of magnitude.

An additional order of magnitude in intensity is lost if the energy selection is achieved with a chicane, the third beamline design, because of its very low efficiency for off axis protons.

The proposed schemes have a solid computational support, even though the space charge effects during the transport have been neglected, and could guide a near term experiment.

A hybrid scheme is of great interest to merge the two worlds of laser-plasma and conventional accelerators, trying to bring out the best of both, but the work in future must be adapted to future acceleration regimes, like RPA. Also, full optical shaping of the proton

beam may be achieved with new technologies. However, since these full optical scenarios are not expected to be available within a decade or two, a big motivation for this thesis was the development of near-term strategies for applications to biomedicine and material physics.

Laser based accelerators can provide not only protons but also electrons of hundreds of MeV and secondary X beams. Due to their moderate cost and size and high flexibility they would be ideally suited for small laboratories or academic research environments.

In the first chapter, I will briefly describe history of laser development, from the theoretical foundations at the beginning of the 20^{th} century, to the first experiments in the Sixties, and to recent achievements, like the many petawatt facilities already built or being developed. I will also discuss analytical treatment and description of a laser pulse.

In the second chapter, the attention will be given to laser-plasma acceleration. The implementation of this mechanism in a computer simulation is also briefly described. A quick overview of electron acceleration is proposed: this technology is already well established and the research community is now mainly focused on building multi-stage devices, or complex solutions coupling different radiation sources. Ion acceleration, on the other hand, is still in its early infancy from the development point of view. Since the interaction between the laser pulse and protons is mediated by electrons, we are still unable to have laser-driven monochromatic and collimated proton sources. We have broad spectra, in energy (exponential spectrum thanks to the thermal equilibrium with electrons) and in angle (flat or Mexican hat spectrum).

In the third chapter, I will describe all the devices that we studied to design beamlines that control the emittance, reduce the size and perform an energy selection for a laser-driven proton bunch. From the simple chicane, built around a collection of magnetic dipoles, to quadrupoles, solenoids, RF cavities and other new plasma-based strategies, I will describe their analytical treatment that is the basis that was used to build their numerical representation in our simulation tools.

In the fourth chapter, I will briefly describe our results that came out from this research. Starting from two of the papers that we published, I will explain pros and cons about using solenoids, RF cavities, quadrupoles and chicanes when applied to real experiments, in a description completely driven by fully 3D simulations done using our software. The chapter concludes with a description of a recent experiment to which we could apply those results.

In the appendices, dedicated to detectors, de-neutralization and INFN projects it's possible to find some details about the detectors currently used in experiments, how to reproduce them in our simulations, techniques designed to remove the comoving electrons from the proton bunch and, finally, an extremely quick description of Italian experiments and Italian important participation in international laser experiments, through INFN.

Please download the latest version of this thesis from
`http://stefano.sinigardi.it/PhD_thesis.pdf`

1 Laser development

Light from laser is extremely peculiar: it has unmatched coherency in space and time.

Laser was born in 1917 with the theoretical foundations by Albert Einstein [14], but its serious life started in 1957 at Bell Labs, with the work of Charles Hard Townes and Arthur Leonard Schawlow [15, 16], as a development of the maser concept.

When atoms have been induced into an excited energy state, they can amplify radiation at the proper frequency. By putting such an amplifying medium in a resonant cavity, feedback is created that can produce coherent radiation.

Modern compact systems, based for example on titanium doped sapphire crystals (Ti:Sa) as the active media, are able to compress up to tens of joules of energy in a spot of few squared micrometers and tens of femtoseconds, making available powers at the level of the petawatt and intensities of 10^{22} Watts per squared centimeter.

Another possibility is to use neodymium doped YAG crystals (YAG is yttrium aluminum garnet, $Y_3Al_5O_{12}$). While the wavelength is modestly increased with respect to Ti:Sa crystals, from $\lambda_0 = 800$ nm to $\lambda_0 = 1$ μm, the main difference in this case is that the pulse is extremely energetic (can be more than 100 J), while also being much longer ($\tau \sim 1$ ps).

The laser maximum intensity grew to these levels through many different leaps, with the most recent one being the chirped pulse amplification (CPA) invention, recently coupled with optical parametric amplifiers (OPCPA) [17].

An important and unavoidable characteristic of these kinds of pulses is the so called pre-pulse. The manipulation of the pulse inside the elements, in fact, creates this extremely short and intense light packet, but there's a pedestal, before the main signal, whose duration can be in the nanosecond scale order and whose intensity is a characteristic that is measured through a very important parameter: the contrast. Contrast is the ratio between the peak and the prepulse intensities and even if it can be up to ten orders of magnitude, like a micrometric thickness when measuring a tens of kilometers height, it might be not enough for some experiments. In fact, assuming a 10^{10} contrast ratio, if we are using a petawatt-class laser with intensities up to 10^{22} W/cm^2 (which is excellent), we have for few nanoseconds an intensity that is in the order of 10^{12} W/cm^2, enough to modify the shape of a target or even destroy it (if it is dramatically thin). In fact, dealing with the prepulse problem will be one of the topic of this thesis, discussed mainly in section 4.1.2.

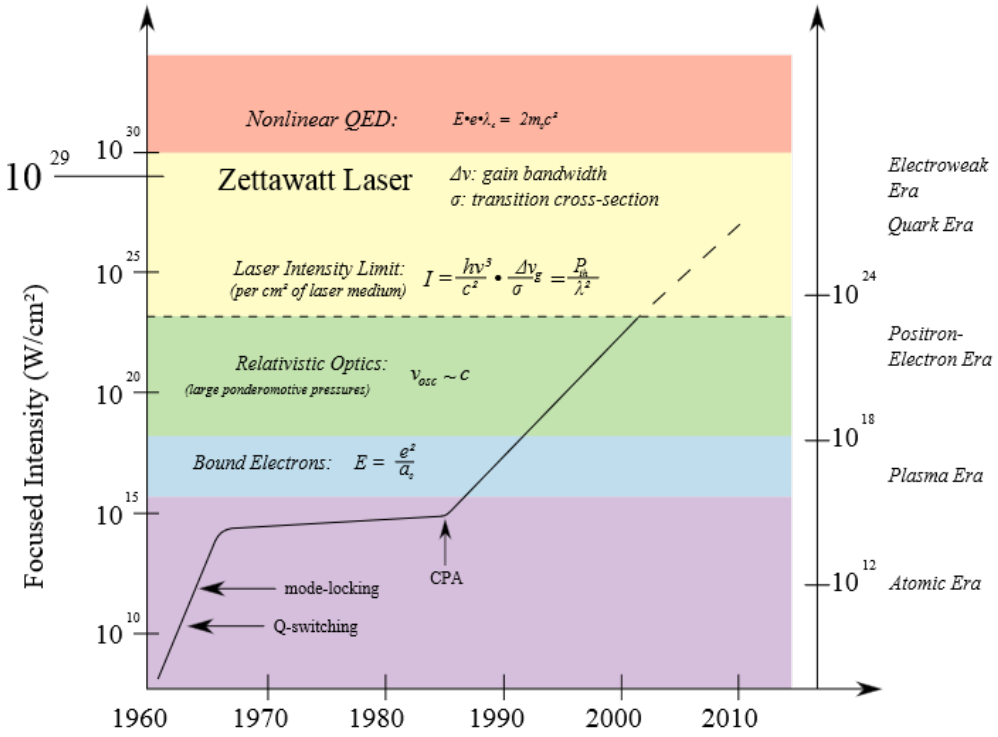

Figure 1.1: Graph showing the history of maximum laser pulse intensity throughout the past 50 years as commonly found in many laser-plasma textbooks. Note that for today and for the future, the line is extremely optimistic. We are well below those values!

Laser	τ [fs]	E [J]	I [W/cm^2]	ℓ [μm]	$E_{\max}$ [MeV]	T [MeV]	ϵ
LOA [18]	40	0.8	6×10^{19}	6	8	—	—
CRIEPI [19, 20]	60	0.1	$\sim 1 \times 10^{19}$	5	1.2	0.2	0.2%
ASTRA [21]	60	0.2	7×10^{18}	20	1.5	—	0.7%
JanUSP [22]	100	10	$\sim 10^{20}$	3	24	3.2	1%
MPQ [23]	150	0.7	$\sim 10^{19}$	10	2.5	—	—
LULI100 [24, 25]	320	30	6×10^{19}	20	20	3	1%
CUOS [26]	400	5	5×10^{19}	12.5	12	—	—
GEKKO [27]	450	25	5×10^{18}	5–25	10	3.4	—
NOVA PW [12]	500	500	3×10^{20}	100	58	6	12%
RAL PW [28, 29]	700	400	2×10^{20}	100	44	—	7%
RAL Vulcan [30]	1000	90	$\sim 10^{20}$	10	36	4.5	5%

Table 1.1: Parameters of some of the laser systems used for high energy proton acceleration experiments and typical parameters of the proton beams produced as reported in the references. Taken from [31]

1.1 An analytical model

In order to study the laser pulse generated by modern devices, and to reproduce it faithfully inside our simulation tools, it's better first of all to give an analytical description of it.

1.1.1 Maxwell equations

$$\operatorname{rot} E = -\frac{1}{c}\frac{\partial}{\partial t}\mathbf{B} \tag{1.1}$$

$$\operatorname{div} B = 0 \tag{1.2}$$

$$\operatorname{rot} B = \frac{4\pi}{c}\mathbf{j} + \frac{1}{c}\frac{\partial}{\partial t}\mathbf{E} \tag{1.3}$$

$$\operatorname{div} E = 4\pi\rho \tag{1.4}$$

Scalar ϕ and vector $\mathbf{A}$ potentials are defined through:

$$\mathbf{B} = \operatorname{rot}\mathbf{A} \qquad\qquad \mathbf{E} = -\operatorname{grad}\phi - \frac{1}{c}\frac{\partial}{\partial t}\mathbf{A} \tag{1.5}$$

This common choice of potentials makes it trivial to satisfy Maxwell equations 1.1 and 1.2. If we choose also a gauge in which

$$\operatorname{div}\mathbf{A} + \frac{1}{c}\frac{\partial}{\partial t}\phi = 0 \tag{1.6}$$

then equations 1.3 and 1.4 become wave equations for the two potentials:

$$\left(\frac{\partial^2}{\partial x^2} + \frac{\partial^2}{\partial y^2} + \frac{\partial^2}{\partial z^2} - \frac{1}{c^2}\frac{\partial^2}{\partial t^2}\right)\mathbf{A} = -\frac{4\pi}{c}\mathbf{j}$$

$$\left(\frac{\partial^2}{\partial x^2} + \frac{\partial^2}{\partial y^2} + \frac{\partial^2}{\partial z^2} - \frac{1}{c^2}\frac{\partial^2}{\partial t^2}\right)\phi = -4\pi\rho$$

in which ρ and $\mathbf{j}$ are density charge and current.

If we are in vacuum, there are no sources and we can choose, of course, $\phi = 0$. In this case the gauge becomes $\nabla \cdot \mathbf{A} = 0$. The relationship with the fields becomes

$$\mathbf{B} = \operatorname{rot}\mathbf{A} \qquad\qquad \mathbf{E} = -\frac{1}{c}\frac{\partial}{\partial t}\mathbf{A}$$

The vector potential $\mathbf{A}$ then satisfy the homogeneous wave equation:

$$\left(\frac{\partial^2}{\partial x^2} + \frac{\partial^2}{\partial y^2} + \frac{\partial^2}{\partial z^2} - \frac{1}{c^2}\frac{\partial^2}{\partial t^2}\right)\mathbf{A} = 0$$

Find a solution using Fourier transforms

Let's consider an assigned field $E(x, y, z; 0) = E(x, y, z; t_0)$ at $t_0 = 0$ (that could be an electric field component, a magnetic field one, or a component of the vector potential). In order to find its evolution, that obeys to the wave equation in the vacuum

$$\left(\frac{\partial^2}{\partial x^2} + \frac{\partial^2}{\partial y^2} + \frac{\partial^2}{\partial z^2} - \frac{1}{c^2}\frac{\partial^2}{\partial t^2}\right)E(x, y, z, t) = 0$$

we can use the Fourier transform

$$E(x,y,z,t) = \frac{1}{(2\pi)^3}\int_{-\infty}^{+\infty} dk_x dk_y dk_z \hat{E}(k_x,k_y,k_z) e^{i(k_x x + k_y y + k_z z - \omega t)} \tag{1.7}$$

where

$$\omega = c\sqrt{k_x^2 + k_y^2 + k_z^2}$$

and $\hat{E}(k_x,k_y,k_z)$ is the Fourier transform of the initial condition

$$\hat{E}(k_x,k_y,k_z) = \int_{-\infty}^{+\infty} dxdydz E(x,y,z,0) e^{-i(k_x x + k_y y + k_z z)}$$

The laser pulse

In order to analyze a monochromatic of finite time duration laser pulse we have to use another representation, as customary in the literature.

$$E(x,y,z,t) = \frac{1}{(2\pi)^3}\int_{-\infty}^{+\infty} dk_x\, dk_y\, dk_z\, \hat{E}(k_x,k_y,k_z) e^{i(xk_x + yk_y + z\sqrt{k_z^2 - k_x^2 - k_y^2} - \omega t)} \tag{1.8}$$

where the frequency is $\omega = ck_z$.

In this case $\hat{E}(k_x,k_y,k_z)$ is the Fourier transform of the pulse at $z = 0$, where we may assume to be located the focus of the pulse.

$$E(k_x,\hat{k}_y,k_z) = \int_{-\infty}^{+\infty} dx\, dy\, d(ct)\, E(x,y,0,t) e^{-i(xk_x + yk_y - ct\, k_z)}$$

In order to write this representation we must know the pulse shape in $z = 0$ at any time, and consequently its Fourier transform.

A laser pulse is an electromagnetic wave which propagates in a given direction (we choose it to be the z axis) and which is determined by the knowledge of its behavior at the focal plane $z = 0$.

In the simplest case we can represent the pulse at $z = 0$ as a Gaussian in the transverse coordinates times a function $f(t)$ which determines its temporal profile

$$E(x,y,0,t) = \exp\left(-\frac{x^2 + y^2}{w_0^2}\right) f(-ct)\, e^{-ik_0 ct} \tag{1.9}$$

where $\omega_0 = c\, k_0$ is the carrier laser frequency.

The corresponding Fourier transform is given by

$$\hat{E}(k_x,k_y,k_z) = \pi w_0^2 \exp\left(-\frac{\left(k_x^2 + k_y^2\right) w_0^2}{4}\right) \hat{f}(k_z - k_0) \tag{1.10}$$

where $\hat{f}(k_z)$ is the Fourier transform of $f(z)$. In the monochromatic case $f = 1$ and the pulse has an infinite time extension so that its Fourier transform reduces to $\hat{f}(k_z) = 2\pi\, \delta(k_z)$. For a beam with a Gaussian temporal profile we write

$$f(ct) = \exp\left(-c^2 t^2 / w_z^2\right)$$

where w_z/c is the a measure of its time extension. Its Fourier transform is given by

$$\hat{f}(k_z) = w_z\sqrt{\pi}\exp\left(-k^2\, w_z^2/4\right)$$

so that $\hat{f}(k_z - k_0)$ has as a limit $2\pi\delta(k_z - k_0)$ for $w_z \to \infty$ and we are back to the monochromatic pulse.

Another type of frequently used temporal profile is given by

$$\begin{cases} f(ct) = \cos^2\left(\frac{\pi}{2}\frac{ct}{w_z}\right) & \text{if } |ct| \le w_z \\ f(ct) = 0 & \text{if } |ct| > w_z \end{cases}$$

and its Fourier transform is given by

$$\hat{f}(k_z) = \frac{\sin(k_z w_z)}{k_z w_z}\frac{\pi^2}{\pi^2 - k_z^2 w_z^2}$$

also in this case we recover the monochromatic pulse in the limit $w_z \to \infty$.

In this Gaussian model for the laser pulse the main parameters are the following:

the central wavelength

$$\lambda_0 = \frac{2\pi}{k_0}$$

the central frequency

$$\omega_0 = ck_0 = 2\pi\frac{c}{\lambda_0}$$

the Rayleigh length

$$z_R = \frac{w_0^2 k_0}{2} = \frac{\pi w_0^2}{\lambda}$$

the beam aperture

$$\theta = \frac{w_0}{z_R} = \lambda\pi w_0$$

Obviously the other two relevant parameters are the transverse waist w_0 and the pulse duration $\tau = w_z/c$.

A remarkable simplification occurs if $z_R \gg w_0$, since in this case the paraxial approximation can be made. We first consider the case of a monochromatic pulse in the paraxial approximation first and then write the exact solution.

Monochromatic pulse

The solution for a monochromatic pulse with a Gaussian transverse profile can be written as

$$E(x,y,z,t;k_0) = \frac{\pi\, w_0^2}{(2\pi)^2}\int_{-\infty}^{+\infty} dk_x\, dk_y\, e^{-(k_x^2+k_y^2)w_0^2/4}\, e^{i(k_x x + k_y y + \sqrt{k_0^2 - k_x^2 - k_y^2}z - \omega_0 t)} \tag{1.11}$$

The solution can be evaluated exactly by reducing to a single integral after introducing polar coordinates

$$x = \rho\cos\theta \quad y = \rho\sin\theta \qquad k_x = k_T\cos\phi \quad k_y = k_T\sin\phi$$

since the angular integration can be performed analytically and one obtains

$$E(x,y,z,t;k_0) = \frac{\pi w_0^2}{(2\pi)^2}\int_0^\infty k_T\,dk_T\,e^{-w_0^2k_T^2/4}\,e^{i(z\sqrt{k_0^2-k_T^2}-k_0\,ct)}\int_0^{2\pi} d\phi\,e^{ik_T\rho\cos(\phi-\theta)} =$$
$$= \frac{w_0^2}{2}\int_0^\infty k_T\,dk_T\,e^{-w_0^2k_T^2/4}\,e^{i(zk_0\sqrt{1-k_T^2/k_0^2}-k_0\,ct)}J_0(k_T\rho)$$

By expanding the exponential into a series of Hankel functions, the solution can be written as a series. However, for numerical purposes, due to the exponential decay of the integrand, very accurate results can be obtained with standard quadrature methods.

A more manageable solution is obtained if the following condition is satisfied

$$\epsilon = \frac{w_0}{2z_R} = \frac{1}{w_0k_0} = \frac{\lambda_0}{2\pi w_0} \ll 1$$

Indeed we can expand the square root in the exponential by neglecting terms beyond the quadratic ones so that the remaining Gaussian integrals are readily evaluated

$$\sqrt{k_0^2-k_x^2-k_y^2} = k_0\left(1-\frac{k_x^2+k_y^2}{2k_0^2}+\ldots\right) = k_0-\frac{k_x^2+k_y^2}{2k_0}+\mathcal{R}$$

Neglecting the remainder $\mathcal{R}$ we can write

$$E(x,y,z,t;k_0) = \pi w_0^2\;I(x)\,I(y)\,e^{i(k_0z-\omega_0t)}$$

where

$$I(x) = \frac{1}{2\pi}\int_{-\infty}^{+\infty} dk e^{-\frac{k^2}{2\sigma^2}+ikx} = \sqrt{\frac{\sigma^2}{2\pi}}\,e^{-\sigma^2x^2/2} \qquad \sigma^2 = \frac{1}{w_0^2/2+iz/k_0}$$

The final results reads

$$E(x,y,z,t) = w_0^2\frac{\sigma^2}{2}\;e^{-\sigma^2\frac{x^2+y^2}{2}}e^{i(k_0z-\omega_0t)}$$

After separating in σ^2 the real and imaginary part, it can be cast in the standard form

$$E(x,y,z,t;k_0) = \frac{w_0}{w(z)}\exp\left(-\frac{x^2+y^2}{w^2(z)}\right)\exp\left(i(x^2+y^2)\frac{z/z_R}{w^2(z)}-i\delta\right)\;e^{i(k_0z-\omega_0t)} \qquad (1.12)$$

where

$$w(z) = w_0\sqrt{1+\left(\frac{z}{z_R}\right)^2} \qquad \delta = \arctan\left(\frac{z}{z_R}\right)$$

The phase δ is known as Gouy phase.

Envelope equation

The solution for a monochromatic wave can be written as

$$E(x,y,z,t) = E_0(x,y,z)\,e^{i(k_0z-\omega_0t)}$$

where $E_0(x,y,0)$ is determined by the transverse distribution in the focal plane at $t=0$. The equation for E_0 reads

$$\frac{\partial^2 E_0}{\partial x^2} + \frac{\partial^2 E_0}{\partial y^2} + \frac{\partial^2 E_0}{\partial z^2} + 2ik_0 \frac{\partial E_0}{\partial z} = 0$$

One can immediately verify that

$$E_0(x,y,z) = \frac{1}{(2\pi)^2} \int_{-\infty}^{+\infty} dk_x dk_y \overline{E}(k_x,k_y)\, e^{i\left(k_x x + k_y y + z\left(\sqrt{k_0^2 - k_x^2 - k_y^2} - k_0\right)\right)}$$

where

$$\overline{E}(k_x,k_y) = \exp\left[-\frac{\omega_0^2}{4}\left(k_x^2 + k_y^2\right)\right]$$

satisfies this equation. If we perform the scaling

$$x = w_0 x' \qquad y = w_0 y' \qquad z = z_R z'$$

the equation becomes

$$\frac{\partial^2 E_0}{\partial x'^2} + \frac{\partial^2 E_0}{\partial y'^2} + 4\epsilon^2 \frac{\partial^2 E_0}{\partial z'^2} + 2i\frac{\partial E_0}{\partial z} = 0$$

where

$$\epsilon = \frac{1}{k_0 w_0}$$

If $\epsilon \ll 1$ the term proportional to ϵ^2 can be neglected and we obtain the so called envelope equation

$$\frac{\partial^2 E_0}{\partial x^2} + \frac{\partial^2 E_0}{\partial y^2} + 2ik_0 \frac{\partial E_0}{\partial z} = 0$$

It is straightforward to say that

$$E_0 = \frac{1}{(2\pi)^2} \int_{-\infty}^{+\infty} dk_x dk_y \overline{E}(k_x,k_y)\, e^{i\left(k_x x + k_y y - z\left(k_x^2 + k_y^2\right)/2k_0\right)}$$

satisfies exactly the envelope equation. In particular, if we choose

$$\overline{E}(k_x,k_y) = e^{-w_0^2\left(k_x^2 + k_y^2\right)/4},$$

then the envelope E_0 of equation 1.10, namely

$$E_0 = \frac{w_0}{w(z)} \exp\left(-\frac{x^2 + y^2}{w^2(z)} + i\Phi\right)$$

where

$$\Phi = \frac{x^2 + y^2}{w^2(z)} \frac{z}{z_R} - \delta,$$

satisfies exactly the envelope equation.

Finite pulse

Let us consider a pulse with a fixed duration (or at least with a fast decrease in time beyond a given interval) with central wave number k_0 and central frequency $\omega_0 = ck_0$. For example we might choose the pulse in the focal plane $E(x, y, 0, t)$ given by equation 1.9 so that its Fourier transform is given by 1.10. In this case, if we let $w_0 \to \infty$, the pulse becomes one dimensional, its Fourier transform is $\hat{f}(k_z - k_0)\,(2\pi)^2\,\delta(k_x)\delta(k_y)$ and the solution becomes

$$E(z,t) = f(z - ct)e^{i(k_0 z - \omega_0 t)}$$

If we denote for convenience $E(x, y, z, t) = E_{\text{mono}}(x, y, z, t; k_0)$ we have

$$E_{\text{mono}}(x,y,z,t;k_z) = \frac{\pi\, w_0^2}{(2\pi)^2} \int_{-\infty}^{+\infty} dk_x dk_y\, e^{-(k_x^2+k_y^2)w_0^2/4}\, e^{i(xk_x + yk_y + z\sqrt{k_0^2 - k_x^2 - k_y^2} - \omega_0 t)}$$

The solution for a pulse of finite duration can be written as

$$\begin{aligned} E(x,y,z,t) &= \frac{1}{2\pi}\int_{-\infty}^{+\infty} dk_z \hat{f}(k_z - k_0)\, E_{\text{mono}}(x,y,z,t;k_z) = \\ &= \frac{1}{2\pi} E^{(0)}_{\text{mono}}(x,y,z,t;k_0) e^{ik_0(z-ct)} \int_{-\infty}^{+\infty} dk_z \hat{f}(k_z - k_0) e^{i(k_z - k_0)(z-ct)} \end{aligned}$$

In the limit of a monochromatic pulse we have $\hat{f}(k_z - k_0) = (2\pi)\delta(k_z - k_0)$ and we recover the previous solution 1.11. If the paraxial approximation holds for the monochromatic wave, we have the following representation

$$E_{\text{mono}}(x,y,z,t;k_z) = E_0(x,y,z;k_z)\, e^{i\,k_z(z-ct)}$$

If time extension of the pulse is large so that its Fourier transform is sharply peaked around k_0, then in the integral we can replace $E_0(x, y, z; k_z)$ with $E_0(x, y, z; k_0)$ obtaining, after integration on k_z, the following approximation which amounts to a factorization of the monochromatic pulse envelope with one dimensional longitudinal pulse:

$$E(x,y,z,t) = E_0(x,y,z;k_0)\, e^{ik_0(z-ct)} f(z - ct)$$

In order to evaluate the error present in this approximation we assume that it satisfies the wave equation exactly

$$\frac{\partial^2 E_0}{\partial x^2} + \frac{\partial^2 E_0}{\partial y^2} + 2ik_0 \frac{\partial E_0}{\partial z} + \frac{\partial^2 E_0}{\partial z^2} + 2\frac{\partial E_0}{\partial z}\frac{\partial \log f}{\partial z} = 0$$

This reduces to the envelope approximation if the last two terms can be neglected. In order to appreciate their weight, we scale the variables according to $x = w_0 x'$, $y = w_0 y'$ and $z = z_R\, z'$. The term before the last one has a factor ϵ^2 after the scaling. To compute the last term we suppose $f(z) = e^{-z^2/w_z^2}$ which implies $|f'(z)/f(z)| = 2|z|/w_z^2$. As a consequence after the scaling the last term is proportional to w_0^2/w_z^2. If $w_z > z_R$ then we have that the contribution of the last term is of order ϵ^2 and can be neglected.

As an example, we consider a laser pulse with the following parameters expressed in μm:

$$\lambda_0 = 2 \quad w_0 = 4 \quad \longrightarrow \quad z_R = 8\pi \simeq 25 \quad \epsilon = 0.08$$

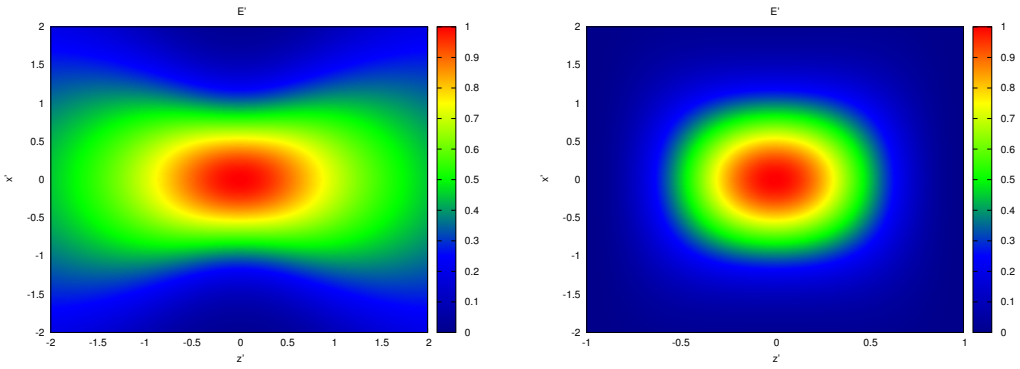

Figure 1.2: Left side: color for the envelope of a monochromatic Gaussian pulse. Right side: color plot for the envelope of the finite pulse $\cos^2(\pi z/2w_z)$ where $w_z = z_R$. The coordinates are scaled: $x' = x/w_0, z' = z/z_R$.

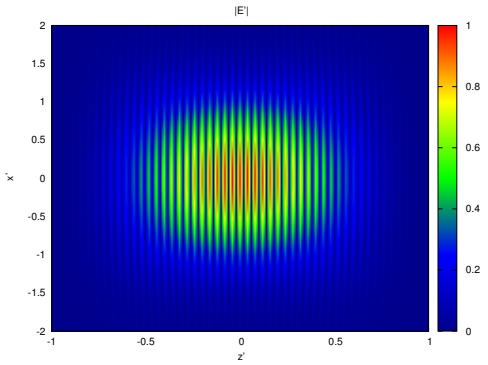

Figure 1.3: Color plot of the absolute value of the field E for a Gaussian pulse of finite duration $\cos^2(\pi z/2w_z)$ where $w_z = z_R$. The coordinates are scaled: $x' = x/w_0, z' = z/z_R$.

In fig. 1.2 we compare the envelope of E for the monochromatic pulse and for a pulse of finite duration where $f(ct) = cos^2(\pi z/2w_z)$ for $|ct| < w_z$ and null elsewhere having chosen $w_z = z_R$.

During my PhD I was the tutor of G. Bondanelli that wrote his bachelor thesis on this topic.

2

Plasma acceleration

In a plasma there are few basic parameters that characterize its dynamic evolution and the propagation of an electromagnetic pulse through it. The first one is the Debye radius, which measures the size of the region on which collisional effects are relevant. This value is obtained by considering a plasma in thermal equilibrium at temperature T and a local deviation from neutrality. By solving Poisson's equation, where the charge density is given by Maxwell's distribution, one finds that the electrostatic field created by the local charge Q vanishes exponentially as

$$V = \frac{Q}{r}\, e^{-r/\lambda_D} \qquad\qquad \lambda_D^2 = \frac{k_B T}{4\pi e^2 n_0}$$

where n_0 is the local charge density. The charge $q(r)$ is a sphere of radius r; it is Q for $r = 0$ and vanishes for $r \to \infty$ according to $q(r) = Q\, e^{-r/\lambda_D}\,(1 + r/\lambda_D)$ since the charge fluctuation is compensated at large distances. Letting $r_c = e^2/m_e c^2$ cm be the classical electron radius, the Debye length can be written as

$$\lambda_D^2 = \frac{1}{4\pi\, r_c\, n_0}\, \frac{k_B\, T}{m_e c^2}$$

The second parameter to be considered is the frequency of the electrostatic oscillations which are created thanks to an electric density fluctuation. Using the linearized fluid equations and the Poisson equation, one finds that the plasma oscillations frequency is given by

$$\omega_p^2 = \frac{4\pi e^2 n_0}{m}$$

As a consequence for the Debye length we can write the following expression

$$\lambda_D^2 = \frac{T}{m\omega_p^2} = \frac{v_T^2}{\omega_p^2}$$

where v_T denotes the thermal velocity.

The plasma is an active medium and when an electromagnetic wave passes through it, it behaves as a medium with a refractive index n. By computing the electric displacement field $\mathbf{D}$ related to the electric field by $\mathbf{D} = n_{\text{ref}}^2\, \mathbf{E}$ we find that

$$n_{\text{ref}} = \left(1 - \frac{\omega_p^2}{\omega^2}\right)^{1/2}$$

where ω is the frequency of a monochromatic electromagnetic wave. If the density is low, then n_{ref} is real and the medium transparent to the wave. If the density is high, then n_{ref} is purely imaginary and the medium is opaque, since the electromagnetic waves does not propagate but becomes evanescent. The transition occurs when $\omega_p^2 = \omega^2$ and the corresponding density value is called critical density

$$n_c = \frac{\omega^2}{4\pi\, c^2\, r_c} = \frac{\pi}{\lambda^2\, r_c}$$

When the medium is overcritical, the wave is damped exponentially as $e^{-z\ell}$ (supposing the propagation is along the z axis) where the damping length, called skin depth, is given by

$$\ell = \frac{\lambda}{2\pi}\left(\frac{\omega_p^2}{\omega^2} - 1\right)^{-1/2}$$

and for $\omega_p \gg \omega$ reduces to $\ell \simeq \frac{c}{\omega_p}$.

Simple analytical models are an important tool to understand the fundamental mechanism underlying complex physical phenomena. This is, of course, valid also in plasma physics and extremely valuable when trying to understand experiments and design new ones.

Unfortunately, laser-plasma interactions are extremely complex in nature and a bare simplification with analytical models are almost impossible except for some uncomplicated situations, still far from experimental conditions, often limited to 1D case. This is the reason why in this field numerical simulations are so important, we can say fundamental, to understand more the evidences and the models.

2.1 Action principle formulations

Our systems can be described determining coordinates, angles or displacements, for every particle. We can denote these generalized coordinates by $q^i(t)$, where $i = 1, 2, \ldots, N$ and N is the number of degrees of freedom of the system. From those we could obtain the Lagrangian $L = T - V$ and from that the action functional as

$$S[q] = \int_{t_0}^{t_1} L(q, \dot{q}, t)dt$$

Thanks to the principle of least action, or its full realization in the Morse theory, we can assume that physical paths are those extremal. It means that the functional derivative of the action vanishes

$$\frac{\delta S[q]}{\delta q^i} = 0$$

and this gives us the Lagrange's equations of motion

$$\frac{\partial L}{\partial q^i} - \frac{d}{dt}\frac{\partial L}{\partial \dot{q}^i} = 0$$

If we prefer the Hamiltonian formulation, we should first calculate canonical momenta using Legendre transformations

$$p_i = \frac{\partial L}{\partial \dot{q}^i}$$

and from them we can write the Hamiltonian as

$$H(q,p) = p_i \dot{q}^i - L$$

where we are using the Einstein notation, so the repeated indices are summed.

Since plasma physics can be described and is governed (in these regimes) by classical physics, the action principle that follows embodies all. It described the dynamics of N relativistic, electrically charged, massive particles, coupled to Maxwell equations to include the electromagnetic fundamental force. As already said, $q_i(t)$ are the particle positions, $\phi(x,t)$ is the electrostatic potential, $A(x,t)$ is the vector potential. It is possible to split the summations into electrons, ions, any number of species that we would like, but this would just make it more cumbersome.

$$\begin{aligned} S[q,\phi,A] = &- \sum_{i=1}^{N} \int_{t_0}^{t_1} dt\, m_i c^2 \sqrt{1 - \frac{\dot{q}_i^2}{c^2}} + \\ &- \int_{t_0}^{t_1} dt \sum_{i=1}^{N} e_i \int dx \left[\phi(x,t) - \frac{\dot{q}_i}{c} A(x,t)\right] \delta\left(x - q_t(t)\right) + \\ &+ \frac{1}{8\pi} \int_{t_0}^{t_1} dt \int dx \left[E^2(x,t) - B^2(x,t)\right] \end{aligned} \tag{2.1}$$

The first term is the kinetic part of the action and involves only the particle variables. The second term represents the coupling between particles and fields. The last term involves only the fields and **E** and **B** should be viewed as the shorthands for their expression in terms of the known potentials: $\mathbf{E} = -\nabla\phi - (\partial\mathbf{A}/\partial t)/c$ and $\mathbf{B} = \nabla \times \mathbf{A}$. As can be seen, it is discarded when calculating the derivative of the action by $q^i(t)$.

Given the great level of generality contained in eq. 2.1 (few minor things are missing, like dissipation, quantum mechanics and general relativistic phenomena, but we can assume their importance is not that much for now in present experimental conditions), we could be tempted to say that we are done, and with a very easy and understandable formalism. However, we have the standard problem that is typically used to motivate statistical mechanics: since N is extremely large, even solving all the equations of motion would be an unuseful task, too great to have any practical avail.

There exist many references for analytical approaches to plasma physics and nice reviews can be found in [32] and [33]. Besides approximations and reductions in the description of our system, this renders explicit the importance of numerical simulations.

2.2 The Maxwell-Vlasov equations

The Vlasov equation determines the phase space distribution f. For a single species, $f(\mathbf{r},\mathbf{v},t)$ defined in $\mathbb{R}^6$ fulfills the Liouville's theorem:

$$\frac{\partial f}{\partial t} + \mathbf{v} \cdot \frac{\partial f}{\partial \mathbf{x}} + \left(\frac{e}{m}\mathbf{E} + \frac{e}{mc}\mathbf{v} \times \mathbf{B}\right) \cdot \frac{\partial f}{\partial \mathbf{v}} = 0$$

E and **B** satisfy Maxwell's equations with sources:

$$\operatorname{div} \mathbf{E} = 4\pi\rho \qquad\qquad \operatorname{rot} \mathbf{B} = \frac{1}{c}\frac{\partial \mathbf{E}}{\partial t} + \frac{4\pi}{c}\mathbf{j}$$

where

$$\rho = Q \int d\mathbf{v} f \qquad\qquad \mathbf{j} = Q \int d\mathbf{v}\, \mathbf{v}\, f$$

and Q is the total charge.

Notice that the function f is normalized:

$$\int d\mathbf{x}\, d\mathbf{v}\, f = 1$$

These equations depend only on the total charge Q and on the ratio e/m. Of course it is necessary to solve them consistently.

If there are s species with charges and masses q_i and m_i, the extension of f is straightforward:

$$\frac{\partial f}{\partial t} + \sum_{i=1}^{s} \left[\mathbf{v}_i \cdot \frac{\partial f}{\partial \mathbf{x}_i} + \left(\frac{q_i}{m_i} \mathbf{E} + \frac{q}{m_i c} \mathbf{v}_i \times \mathbf{B}_i \right) \cdot \frac{\partial f}{\partial \mathbf{v}_i} \right] = 0$$

with sources

$$\rho_i = \sum_{i=1}^{s} Q_i \int d\mathbf{v}_i f \qquad\qquad \mathbf{j}_i = \sum_{i=1}^{s} Q_i \int d\mathbf{v}_i\, \mathbf{v}_i\, f$$

where, as before, Q_i is the total charge for the ith species.

Vlasov system is obtained in the limit $N \to \infty$, keeping total charge and mass constant (and consequently also the ratio e/m).

We can see here just the treatment of the single species case, since the extension to s species is trivial.

After taking the limit, one can introduce any finite value N, e, m for the particle number, charge and mass, just imposing that $Ne = Q_{\text{phys}}$ and $e/m = e_{\text{phys}}/m_{\text{phys}}$. As a consequence, if $N = N_{\text{phys}}$, then $e = e_{\text{phys}}$ and $m = m_{\text{phys}}$.

In the numerical procedure, f is sampled with a finite number of points, namely (referring to a single species)

$$f = \frac{1}{N} \sum_{k=1}^{N} S(\mathbf{x} - \mathbf{x}_k(t)) \delta(\mathbf{v} - \mathbf{v}_k(t)) \qquad\qquad \int S(\mathbf{x}) d\mathbf{x} = 1$$

where $S(\mathbf{x})$ is a positive function, peaked at $\mathbf{x} = 0$. Then N is the number of macroparticles (the numerical particles) and e and m are their charge and mass.

The distribution f is then consequently sampled with N macroparticles with mass and charge

$$m = m_{\text{phys}} \frac{N_{\text{phys}}}{N} \qquad\qquad e = e_{\text{phys}} \frac{N_{\text{phys}}}{N}$$

each one evolving according to the equations of motion

$$\frac{d\mathbf{x}_k}{dt} = v_k \qquad\qquad m \frac{d\mathbf{v}_k}{dt} = e\mathbf{E} + \frac{e}{c} \mathbf{v}_k \times \mathbf{B}$$

where the fields satisfy Maxwell's equation with sources

$$\rho = e \sum_{k=1}^{N} S\left(\mathbf{x} - \mathbf{x}_k(t)\right) \qquad \mathbf{j} = e \sum_{k=1}^{N} S\left(\mathbf{x} - \mathbf{x}_k(t)\right)\, v_k(t)$$

This is the Particle-In-Cell solution of the Vlasov system.

2.3 ALaDyn

As just said, in the PIC technique, the particle phase-space f_s is sampled by a lower number of numerical particles. With this approximation, the characteristics of Maxwell-Vlasov equations are obtained by solving the relativistic equations of motion setting $q_i/m_i = q_s/m_s$, so that the ratio charge over mass is preserved. In this way, we keep constant the main characteristics of the plasma, λ_0 and ω_p. The numerical particles acquire a weight to transform them to physical particles that is governed by the requirement that the total mass and the total charge of the system are preserved.

The other approximation is related to the fields, that are discretized on a spatial grid. The interpolation procedure is done with smoothing functions and their choice is of fundamental importance, since the evaluation of the fields on the particle position is then done through an interpolation.

Spatial integration is done through finite difference algorithms and time integration with usual leapfrog or Runge-Kutta algorithms.

This is the basic foundation for Particle-In-Cell (PIC) algorithms. The fundamental book describing this technique is reported in [34], but also some interesting papers exist on this topic, with a nice review being noted in [35].

The PIC code developed in our group to deal with laser-plasma simulations is called ALaDyn (Acceleration by Laser and Dynamics of charged particles) [36, 37, 38]; while already being under development before 2008, it has been reviewed extensively in the last year thanks to a PRACE (PaRtnership for Advanced Computing in Europe) project that was awarded to a collaboration that involved our group in Bologna and another group in Pisa. This project, called Large Scale Acceleration of Ions by Lasers (PRACE LSAIL), granted us a total of 10M CPU hours and allowed us to do some new studies. The computational requirements were much heavier than any other simulation already done and this project required some development in the I/O routines, in the visualization and in the numerical descriptions of few target models. The result is a faster code, that scales better on new BlueGene/Q architecture and that is much more reliable in general. For the future, other codes are under development. A C++ version is under construction, while a CUDA one [39] is already in production for few cases [40]. The main repository is available online, under request, on GitHub[1].

ALaDyn is already extremely flexible but the user can easily add its own modules. There are many different target shapes and models, different species, laser polarizations, but any new case can be user defined in the code.

Basic Time Cycle

At the core of any Particle-In-Cell code there are very few dynamic variables: at each grid point we have to know **E** and **B** fields, while for each macro-particle we store **r** and **p**. Neglecting the details of the time integration and any possible numerical scheme trick, like the possible time-staggering required by the Leap-Frog algorithm, a basic time cycle can be outlined as described in figure 2.1.

Visualization

Originally the code had just an IDL interface, but since the PRACE project, I developed another custom visualization interface, that does all the analysis on the fly and uses gnuplot

[1] https://github.com/cenit/ALaDyn.git

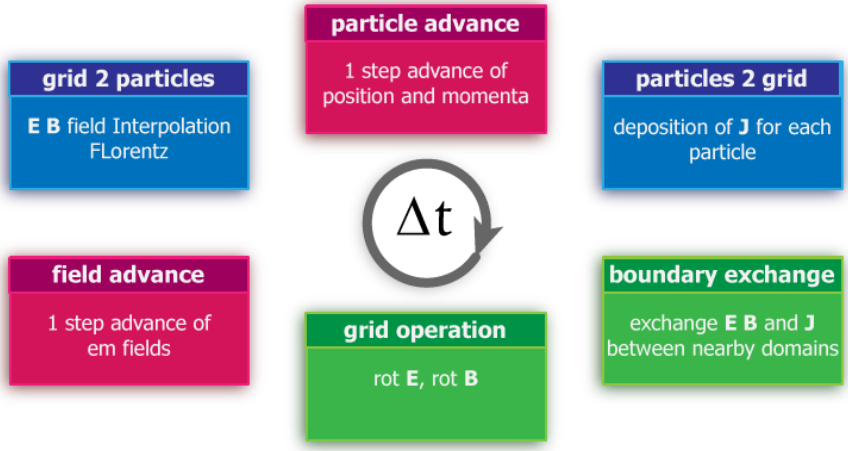

Figure 2.1: Basic PIC cycle scheme

as the drawing interface, since the gigantic (multi-terabytes) output coming from these new massively parallel simulations is not feasible for IDL. The code is available for free on a repository on GitHub[2].

2.4 Electron acceleration

A laser pulse interacting with a underdense gas-jet, $\omega_p \ll \omega_c$ generates a train of electron plasma waves (the wakefield) with wavelength $\lambda_p \gg \lambda_0$. At sufficiently high intensities, $I > 10^{18}$ W/cm^2 the associated longitudinal electrostatic field E_z can attain values in the $1-10$ GV/m range and can then be used as compact linac for electrons acceleration (Tajima and Dawson [6]).

Different acceleration mechanisms have been identified and experimentally investigated, depending on the laser-plasma configurations and on the basic ordering parameters: n_e, the unperturbed plasma electron density, and a_0, the adimensional laser vector potential. For a recent discussion see the V. Malka review paper [41].

In a broad classification of electron acceleration two main configurations have been designed:

i external injection;

ii self-injection.

In the former configuration, a low-charge high-quality electron bunch, with energy $0.1 \div 1.0$ GeV, produced by a conventional linac, is injected in the region where the wakefield attains the maximum acceleration field. To assure significant and stable energy increase, it is then necessary that the witness bunch has a small size and propagates over long distances in phase with the laser-driven wakefield. These conditions require linear or weakly nonlinear laser intensity, which means $a_0 < 1$, low plasma electron density, $n_e = 10^{14} \div 10^{16}$ cm^{-3}, to reduce the laser pulse depletion, and a proper shaping of the plasma channel to control the laser propagation (optical guiding, [42]). In the self-injected configuration, the laser-driven wakefield produces directly bunches of high energy electrons by acceleration of the low energy background electrons.

[2] `https://github.com/cenit/leggi_particelle.git`

A promising and efficient self-injection mechanism, working at high laser intensity $a_0 > 2$ and high plasma density $n_e > 10^{18}$ cm^{-3}, the so called "bubble regime", has been identified. Here, the laser ponderomotive force $\nabla|A|^2/2$ is strong enough to expel all the electrons in the region just behind the main pulse, forming a positively-charged cavity. The strong electrostatic fields produced by this charge separation forms a non-linear wakefield behind the bubble. At the same time, a significant fraction of the electrons, pushed on the boundary of the cavity, are injected and accelerated by the first bucket of the wakefield.

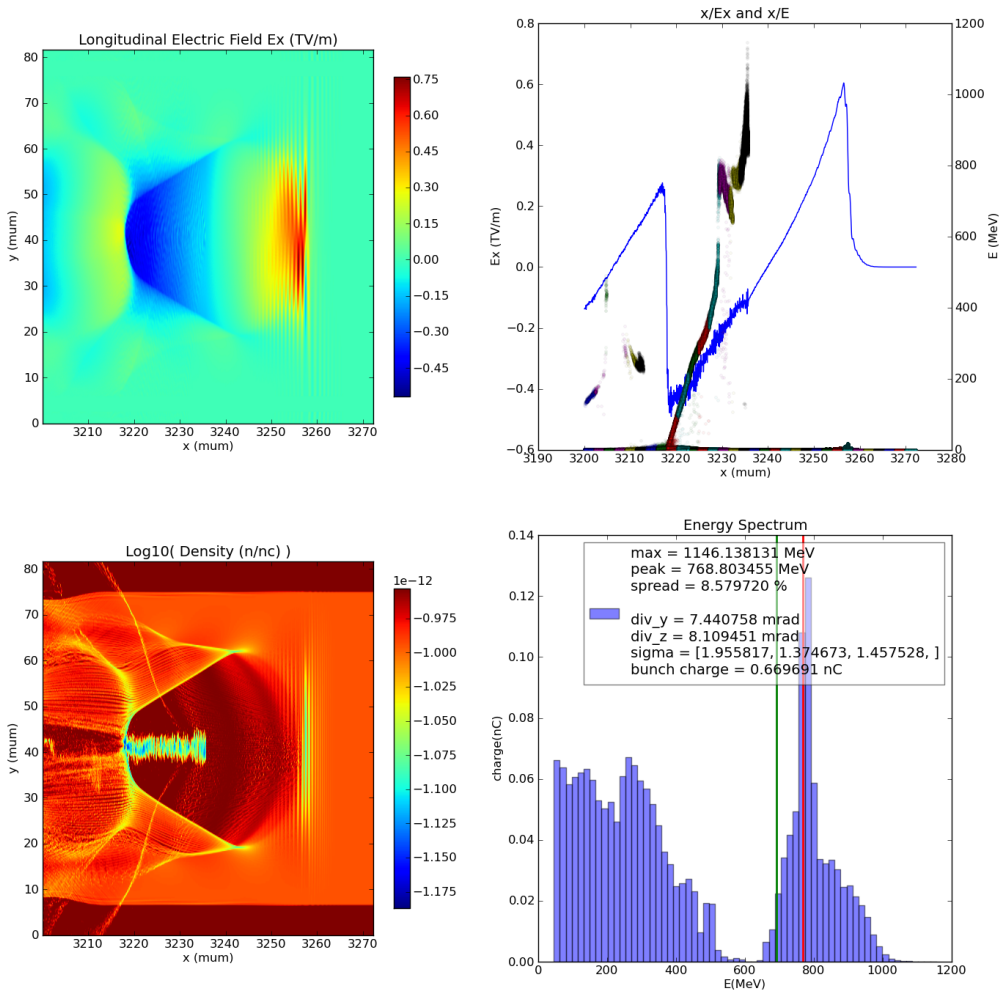

Figure 2.2: "Bubble" regime, electron self-injection and acceleration with lasers. 3D simulation done with `jasmine` .

This mechanism has been investigated numerically in 2002 by Pukhov and Meyer-Ter-Vehn [43], and then and experimentally observed for the first time in 2004 [9, 8, 7]. We can see a simulation result of bubble electron acceleration, obtained with our code `jasmine` , in figure 2.2.

One of the most recent results on laser-plasma acceleration of electrons has been obtained at the Texas Petawatt Laser Facility [11], with 2 GeV electron bunch reported.

2.5 Ion acceleration

Since early 1960's, ions have been accelerated from laser-produced plasmas. One of the first reported papers on this subject [44] describes the results of a single "giant" (for that time) pulse shot on a target plate. In its bibliography we can find the first reports on laser-plasma ion acceleration. Those results, even if based on a 0.2 J laser pulse, with a duration of 40 ns FWHM (5.4 MW of peak power), were already encouraging: ion energies of 1 KeV were obtained and it was already possible to observe that:

- The ion energy on the upstream layer was independent of the thickness of the target
- If the target was not very thick, the energy of ions on both sides are almost the same, or different by a factor of two at most
- It was also found that, on a first analysis, the product of thickness and ion energy on the downstream layer was approximately constant.

As more powerful lasers were built and used as research tools, the amount of pulse energy that was converted into fast ions was determined to be substantial.

When intense laser light is absorbed on a target, producing plasma, we also know that an extremely strong magnetic field appears. This is well known since the 70s [45] and in fact it was proposed that these self-generated fields effectively insulate fast electrons from the surface of the target, and the resulting space charge electric field acts to accelerate large numbers of ions. In the 1986 [46], using a CO_2 laser facility, ions up to the MeV range were observed. A correlation between the fast ion energy, the laser intensity and the electron temperature, as measured from the slope of the bremsstrahlung x-ray spectrum, was already extremely difficult. An interesting point to notice was that they already saw few populations, different for their temperatures, in the x-ray data, a feature that we will see also in recent complex experiments that is difficult to interpret and for which only numerical simulations, most of the times, can give a glimpse on the meaning.

A major breakthrough in laser-driven proton beams was obtained in 2000, at LLNL. In [12], Snavely et al. reported proton energies up to 58 MeV, with the important characteristic of the beam that is the good collimation perpendicular to the rear (un-irradiated) surface.

I will take a short description of this experiment because of its importance and because, differently from many other more recent experiments, they collected a lot of data extremely useful to explain how we then decided to proceed in our analysis.

Snavely et al. used a CPA laser system generating 1 PW pulses of 500 fs duration, focused up to 3×10^{20} W cm^{-2} on a focal spot of 9 μm FWHM, with 30% of the energy inside the first minimum. In the paper there's also an interesting discussion about the prepulse. During the experiment, the amplified spontaneous emission was estimated to be a 4 ns emission, with 10^{-4} of the main pulse energy, followed by a 2 ns prepulse with 3×10^{-4} energy, all before the arrival of the main pulse. In this paper the analysis of the experimental condition was extremely well defined and they measured the effect of this precursor radiation as the generator of a micrometric plasma describable with an exponential density profile having a scale length of 40 μm.

The proton beam was detected with a stack of radiochromic films, and it was recorded as a beam well collimated emitted perpendicular to the rear target surface, so at 45 degrees with respect to the laser axis (the shot was not normal to the target, as almost always, to reduce risks for the reflected light to go back inside the laser optics, destroying them). The reconstruction of the proton energies was calculated as a function of the response of each RC film layer using the SRIM code [47, 48, 49]. As already said, the maximum energy was

recorded as a cutoff at about 58 MeV, fitted by an exponential with a mean energy of 4 MeV and a wonderful conversion fraction of laser energy to protons with kinetic energy higher than 10 MeV at 12%. Similarly corresponding data were also acquired with the magnetic spectrometer, operated via a hole in the RC film detector.

This experiment can be considered as the starting point for the modern laser-plasma acceleration of ions and protons. In fact, the interpretation that they did about the generation of the proton beam was as a planar electrostatic acceleration by a dynamic Debye sheath formed at the rear target surface by hot electrons.

Beyond the following proton/ion acceleration models I'm going to describe, there exists also other mechanisms: the "Coulomb explosion" [50, 51], the "Shock acceleration" [52, 53] and the "Break-Out Afterburner" [54, 55, 56, 57].

2.5.1 Target Normal Sheath Acceleration

The Physical Review Letter by Snavely et al. [12] relies on other papers to give a theoretical explanation of the results they were observing: Y. Kishimoto et al. [58], S. Hatchett et al. [59], and Wilks et al. [60].

As described in the Hatchett paper, the leakage prepulse generate a preformed plasma, measured by interferometry, to have an on-axis electron density of 3×10^{19} cm^{-3} 70 μm away from the target and a density profile exponentially falling to lower densities with a scale length of 40 μm. The interaction of the main laser pulse with the preformed plasma and the underlying solid target generate a source of relativistic electrons directed into and through the target, generating x-rays inside. Laser pulse self-focusing in the preformed low-density plasma [61] also acts to increase the intensity and the mean pulse in this way becomes an intense hot electron source. It is estimated in the paper that 10^{14} hot electrons were generated. This leaves all the ions building the material behind and a great positive charge is created inside the target. Only a very small fraction of these electrons can leave from behind the target before the resulting Coulomb potential traps the rest. They will fly through the target in a broad angular beam as can be seen from bremsstrahlung data in [59], be turned around near the back and then bounce back and forth through the target drifting transversely.

A nice and deep theoretical analysis on the problem has been written by Passoni and Lontano in 2003 [62]. Starting from the work by Hatchett et al. and Wilks et al., they try to describe a one dimensional analytical model to briefly analyze what happens. They call this mechanism Target Normal Sheath Acceleration (TNSA).

In fact, even if many theoretical and numerical studies have been done, the interpretation of the experimental results, often contradictory because of the many parameters that come into play, not to forget also the total lack of stability of these prototypal systems, is absolutely not an easy job.

Before studying in more detail the TNSA model, it's useful to remark that even if lasers are extremely energetic and intensities are very high, their pulse is still not enough to directly accelerate ions. In fact, as clearly explained in [63], the transverse quivering momentum of a charged particle of mass M and charge Ze in an electromagnetic wave is proportional to the adimensional laser parameter a_0. Writing with m_e the mass of the electron, the formula reads:

$$\frac{v_i}{c} = \frac{Zm_e}{M_i} a_0$$

This shows that in order to get a relativistic ion motion from the laser fields, we need an a_0 that is comparable with the ratio of the mass of our particle to the mass of an electron.

For protons, this is ~ 2000, absolutely beyond what is technologically feasible nowadays ($a_0 \sim 30$).

This clearly explains that the ion acceleration is currently mediated by the electrons. Let's see a basic analytic description of the model itself.

For simplicity we consider a one dimensional configuration in which the laser pulse propagates along the z direction, is linearly polarized so that $A_y(z)$ is the only non vanishing component of the vector field and interacts with a particle (electron) of mass m_e and charge e. The conjugate momenta are

$$P_x = 0 \qquad P_y = p_y - m_e c\, a \qquad P_z = p \qquad a = \frac{e\, A_y}{m_e c^2}$$

where we denoted by a the dimensionless vector potential. Since $P_y = p_y - mca$ is conserved and it is initially zero before the laser pulse interacts with the particle we have $p_y = m_e\, c\, a$ and the electron kinetic energy is

$$T = m_e c^2(\gamma - 1) = m_e\, c^2 \left[\left(1 + \frac{p^2}{m_e^2 c^2} + a^2\right)^{1/2} - 1\right]$$

The electron temperature is the average kinetic energy of the electron and supposing that $a \gg p/m_e c$ (and $a \gg 1$) we have

$$T \simeq m_e c^2 a \qquad T[\mathrm{MeV}] = \frac{a}{2}$$

In order to estimate the energy gained by the protons in the electrostatic field created by the charge separation due to hot the electrons diffusion we assume that the electrostatic potential fulfills the Poisson-Boltzmann equation. Letting $-e$ be electron charge the equation reads

$$\frac{d^2V}{dz^2} = 4\pi\, e\, n_0\, e^{eV/T}$$

which in the dimensionless variables $\zeta = z/\lambda_D$ and $\Phi = eV/T$ becomes

$$\frac{d^2\Phi}{d\zeta^2} = e^{\Phi}$$

If the thickness of the layer is h by imposing that $V'(0) = V'(h) = 0$ integrating by parts and letting $\eta = h/\lambda_D$ the solution reads

$$\Phi = \log\left(1 + \tan^2\left(\frac{\zeta - \eta}{\sqrt{2}}\right)\right)$$

The potential $V(z) = T/e\,\Phi(z/\lambda_D)$ is a decreasing function of z so that the energy gained by an ion of charge Z in the transit from $z = 0$ to $z = h$ is

$$E_{\max} = ZeV(0) = ZT\, \log\left(1 + \tan^2\left(\frac{h}{\lambda_D\sqrt{2}}\right)\right)$$

The parameter h represents a Debye length for hot electrons $h^2 = T/(4\pi\, e^2\, n_{0\,\mathrm{hot}})$ so that

$$\frac{h^2}{\lambda_D^2} = \frac{n_0}{n_{0\,\mathrm{hot}}}$$

Some simulations suggest that that $h \simeq 2\lambda_D$ since the density of hot electrons is about 25% of the total electrons density.

Finally for $E_{\max}[\text{MeV}] = E_{\max}/2m_ec^2$ we obtain the following result

$$E_{\max}[\text{MeV}] = \frac{Za}{2} \log\left(1 + \tan^2\sqrt{2}\right) \simeq 2Za$$

For a proton, the maximum energy (expressed in MeV) is $2a$, whereas its temperature, assuming local thermal equilibrium, is equal to the electron temperature $a/2$. The ratio between the proton temperature and its maximum energy for the 1D model is $1/4$, while 3D simulations and experiments suggest a ratio $\sim 1/8$. From 2D simulations a ratio $\sim 1/6$ is obtained. The suggested dependence on the dimension D is

$$\frac{T}{E_{\max}} = \frac{1}{2(D+1)}$$

The model suggests that the proton energy spectrum is exponential (Boltzmann distribution)

$$\begin{cases} \dfrac{dN}{dE} = \dfrac{N_0}{E_0} \dfrac{e^{-E/E_0}}{1 - e^{-E_{\max}/E_0}} & \text{for} E < E_{\max} \\ \dfrac{dN}{dE} = 0 & \text{for} E > E_{\max} \end{cases}$$

and N_0 is the total proton number. For $E_{\max} \gg E_0$ the distribution is fairly well approximated by

$$\begin{cases} \dfrac{dN}{dE} = \dfrac{N_0}{E_0} e^{-E/E_0} & \text{for} E < E_{\max} \\ \dfrac{dN}{dE} = 0 & \text{for} E > E_{\max} \end{cases}$$

The constant E_0 is just the proton temperature T. For an exactly exponential spectrum the average energy is $\langle E \rangle = N_0 E_0$ so that we can write

$$T = E_0 = \frac{\langle E \rangle}{N_0}$$

In simulations and experiments E_0 obtained from the slope of the straight line approximating $\log dN/dE$ and the average energy $\langle E \rangle$ may differ from $N_0 E_0$, since $\log dN/dE$ is not linear on the whole interval $[0, E_{\max}]$. The discrepancy gives a measure of how far we are from thermal equilibrium. In analyzing the data we compute the temperature T by identifying it with E_0 where $1/E_0$ is the slope of the straight line approximating $\log dN/dE$.

Experiments on laser-plasma acceleration of ions clearly show that the electron population produced at the rear target surface can be characterized by at least two temperatures. We can try to limit us to this lower level of just two, one cold and one hot, and try to re-analyze the model [64].

The hot electron population is created directly by the laser heating and its ponderomotive force at the front surface of the target. Electrons in this population form a beam propagating inside the target normally to the surface, even if the laser was impinging non normally and the divergence seems to be not so high, around $\pi/20$. Traditional estimations [64] put the energy conversion at a staggering level of 30%. Nowadays, confirmed also from numerical simulations, this value seem really exaggerate, and we consider a good laser energy conversion efficiency when we talk about 10%. This means, anyway, that the population is extremely big, at the order of 10^{13} electrons, with a density around two orders

of magnitude lower than the solid density. Their motion creates big fields inside the target itself and a noteworthy charge imbalance. Because of this phenomenon, when shooting on metallic targets, the conduction electrons around the spot are put in motion and they form a return current. In insulators, this free electron population is created by the thermal ionization and the fields themselves.

This is the cold electron population and since its density is of the order of the solid density, it's not important that they have a high speed to neutralize the charge imbalance. In fact they're cold, their temperature can be much lower than that of the hot electrons, even if we should understand that the laser interaction itself, mainly if it's a long process, can heat them up anyway.

Let's consider a semi-infinite slab of matter with a step-function density distribution for ions ($n_i = n_{0i}$ for $x = 0$ and $n_i = 0$ for $x > 0$, where x is the normal to the target surface) and two density profiles for the two electron populations, dependent on x, while their temperatures $T_{h/c}$ are constant. Both electron populations follow the Boltzmann distribution]

$$n_{e(h/c)} = n_{0(h/c)} \exp(e\phi/T_{h/c})$$

where $n_{0(h/c)}$ is the initial unperturbed hot/cold electron density. We can describe the electrostatic potential with the Poisson equation, that, imposing as before Ze as the charge for the charged particles (ions or protons, depending on the cases), reads as

$$\partial_x^2 \phi = 4\pi e(n_{eh} + n_{ec} - ZN_i)$$

Since we are considering a semi-infinite slab, on the left side ($x \to -\infty$) we are inside the solid and we can say that reasonable boundary conditions requires no fields: $\partial_x\phi(-\infty) = \phi(-\infty) = 0$. The same applies for the right side, in the vacuum, for $x \to \infty$: $\partial_x\phi(\infty) = \phi(\infty) = 0$, but unfortunately the choice of a Boltzmann distribution collides with it and we have to just accept $\partial_x\phi(\infty) = 0$ and $\phi(\infty) \to -\infty$. Of course this is a problem, since it means that we can have particles with a divergent final kinetic energy, but it is solved in [58, 62].

Applying the previous equation inside the target, it becomes:

$$\partial_x^2 \phi = 4\pi e(n_{0h} e^{(e\phi/T_h)} + n_{0c} e^{(e\phi/T_c)} - ZN_{0i}) \tag{2.2}$$

If we define, for our convenience, the terms

$$\begin{aligned} a &\equiv n_{0c}/n_{0h} \\ b &\equiv T_c/T_h \\ \varphi &\equiv e\phi/T_h \text{ dimensionless potential} \\ \lambda_{dh} &\equiv \sqrt{T_h/\left(4\pi n_{0h} e^2\right)} \text{ unperturbed hot electron Debye length} \end{aligned}$$

knowing the first integral of 2.2 as

$$\lambda_{dh}^2 (\partial_x \varphi)^2 = 2\left[e^\varphi + abe^{\varphi/b} - (1+ab) - (1+a)\varphi\right] \tag{2.3}$$

then the implicit solution can be written as

$$\int_{\varphi(0)}^{\varphi(x)} \frac{d\varphi}{\sqrt{e^\varphi + abe^{\varphi/b} - (1+ab) - (1+a)\varphi}} = -\sqrt{2}\frac{x}{\lambda_{dh}} \tag{2.4}$$

As noted by [64], far from the plasma surface the arguments φ and φ/b are small enough to be not considered and so we can find the explicit solution

$$\varphi \approx \varphi(0) e^{\left[\left(1+\frac{a}{b}\right)^{1/2} \frac{x}{\lambda_{dh}}\right]} \tag{2.5}$$

Outside of the plasma ($x > 0$), the Poisson-Boltzmann equation for the potential φ reads

$$\lambda_{dh}^2 \partial_x^2 \varphi = e^{\varphi} + a e^{\varphi/b} \tag{2.6}$$

that has

$$\lambda_{dh}^2 (\partial_x \varphi)^2 = 2\left[e^{\varphi} + ab e^{\varphi/b}\right] \tag{2.7}$$

as the first integral and

$$\int_{\varphi(0)}^{\varphi(x)} \frac{d\varphi}{\sqrt{e^{\varphi} + ab e^{\varphi/b}}} = -\sqrt{2}\frac{x}{\lambda_{dh}} \tag{2.8}$$

as the implicit solution.

Taking the limits $a \to 0$ and $b \to 1$ in equations 2.4 and 2.8 corresponds physically to consider a single-temperature electron population, a simpler model discussed in [65].

At $x = 0$, that is the interface between the two solutions, we have to require the continuity of the potential and of the electric field. This condition gives us a way to compute them, evaluating 2.3 together with 2.7 at $x = 0$.

This gives us

$$\varphi(0) = -\frac{1+ab}{1+a}$$

or, using original symbols,

$$e\phi(0) = -\frac{T_h n_{0h} + T_c n_{0c}}{n_{0h} + n_{0c}}$$

The maximum electric field $E(0)$ is then given by

$$E(0) = \sqrt{2}\frac{T_h}{e\lambda_{dh}} \sqrt{\left\{e^{-b[(1+ab)/(b+ab)]} + ab e^{(1+ab)/(b+ab)}\right\}}$$

and from it we can infer subsequent details about the maximum energy that we can transmit to protons [64].

In figures 2.3 it is shown the base mechanism in action: the laser pulse hit the target and get reflected.

In figures 2.4 and 2.5 it is shown the effect of the laser pulse on electrons and, indirectly, on protons. As electrons are heated and expelled from the solid structure, protons feel the strong fields and are pulled out.

2.5.2 Radiation Pressure Acceleration

The Radiation Pressure Acceleration (RPA) mechanism was found and has been developed numerically by Esirkepov et al. [66, 67]. At intensities $I > 5 \times 10^{21}$ W/cm^2, this acceleration method that we are going to briefly analyze starts to dominate over TNSA.

The fundamental difference with the TNSA mechanism relies on the fact that the interaction between the laser and the plasma is not mediated by a thermal heating of the electrons. The ponderomotive force acts directly accelerating electrons (and also protons and ions) in this regime [68].

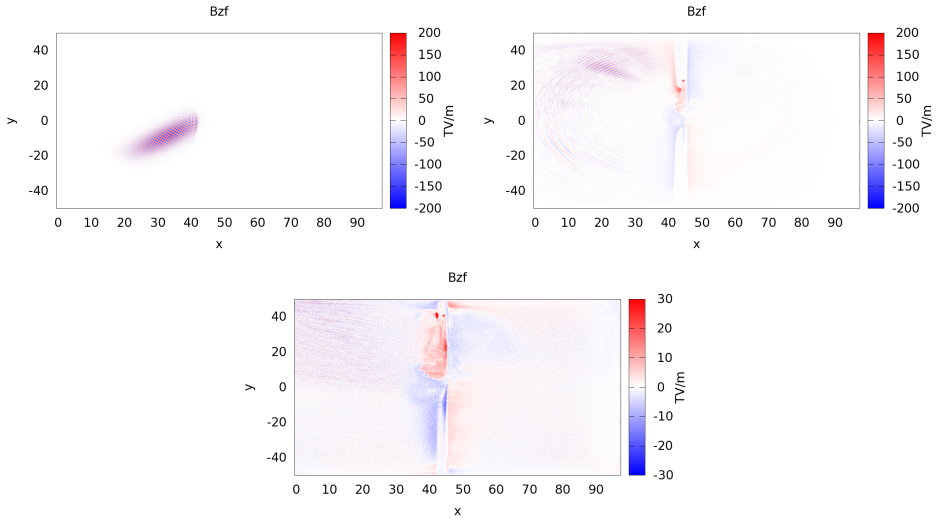

Figure 2.3: B fields for a TNSA simulation at t=33,166,333 fs. Target parameters: $\ell_{\text{preplasma}} = 2.8\mu$m, $n_{\text{preplasma}} = 3.0n_c$ with an exponential ramp to the target density that is $n_{\text{target}} = 100n_c$, $\ell_{\text{target}} = 0.5\mu$m, $\ell_{\text{contaminants}} = 80$ nm. Laser parameters: $\tau = 40$ fs, $a_0 = 23.5$, $\lambda = 0.8\mu$m, $w_0 = 3.25\mu$m

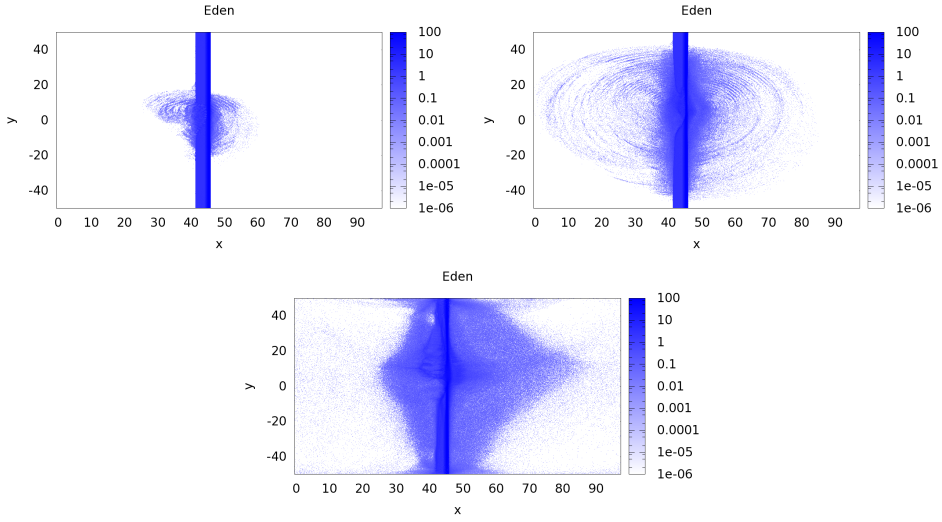

Figure 2.4: Electron density for the same 2D TNSA simulation at t=66,133,333 fs.

To see just a basic feature of this mechanism, let's see how an electromagnetic wave carries not only energy but also momentum. Let's consider a plain electromagnetic wave propagating in vacuum and a planar surface Σ perpendicular to the wave propagation direction x. This surface is made of electric charges (ionized atoms, so electrons+ions/protons), with a planar density σ. Lorentz force in this case is:

$$\mathbf{F}_\sigma = \sigma(\mathbf{E} + \mathbf{v}_\sigma \times \mathbf{B})$$

where $\mathbf{v}_\sigma$ is the speed transferred by the electric field to the electric charges. The total effect on the material surface is

$$\mathbf{F}_\sigma \cdot \mathbf{v}_\sigma = \sigma\mathbf{E} \cdot \mathbf{v}_\sigma + \sigma\mathbf{v}_\sigma \times \mathbf{B} \cdot \mathbf{v}_\sigma = \sigma v_\sigma E$$

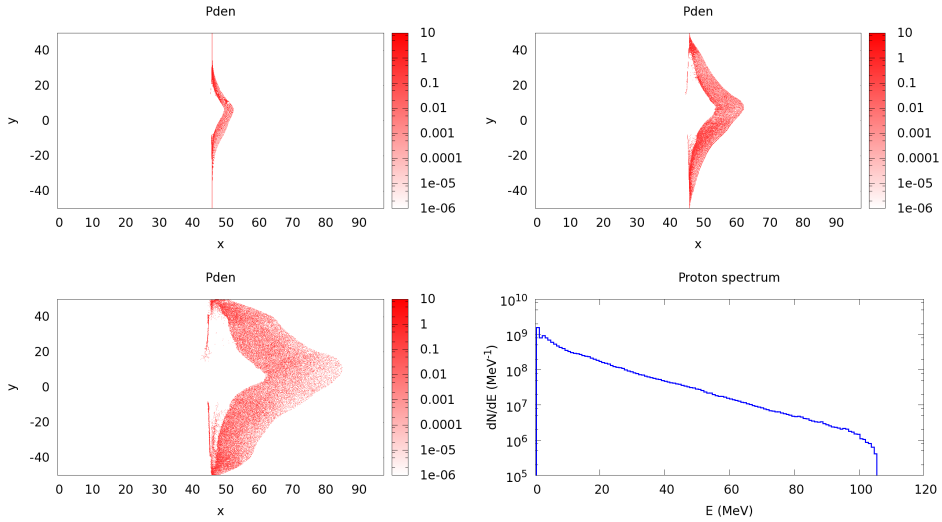

Figure 2.5: Proton density for the same 2D TNSA simulation at t=133,200,333 fs, and final proton spectrum.

The term with **B** is canceled and so it does not contribute to the absorbed power. Intensity given by the wave to the surface (energy per unit of time and surface) on average is

$$I = \sigma \langle v_\sigma E \rangle \tag{2.9}$$

This intensity does not produce a global mechanical effect on the surface, since **E** is parallel to it. The net effect is just a current. On the other hand, the magnetic force produces a mechanical effect without contributing to the absorbed power. In fact, on average we have

$$\langle \mathbf{F} \rangle = \sigma \langle \mathbf{v}_\sigma \times \mathbf{B} \rangle = \sigma \langle v_\sigma B \rangle \mathbf{u}_x \tag{2.10}$$

We can rewrite 2.10 as

$$\langle \mathbf{F} \rangle = \frac{\sigma}{c} \langle v_\sigma E \rangle \mathbf{u}_x = \frac{I}{c} \mathbf{u}_x,$$

where we have also used the 2.9 relationship.

This average force, calculated per unit of surface, corresponds to an average pressure, also knows as radiation pressure, exerted by the wave on the surface Σ.

On the other hand, if the wave gives the energy I to the surface Σ, it's not out of mind to think that it received also the pulse I/c. These results are valid for fully absorbing surfaces. The other, totally opposite case, is for surfaces completely reflective: in this situation, the wave after the reflection is propagating along $-\mathbf{u}_x$, so the momentum has flipped the direction and the pulse transmitted to Σ is double than before:

$$P_{\text{rad}} = \frac{2I}{c}$$

In general, a surface partly absorbs and partly reflects the electromagnetic incident energy. Denoting with R the reflection index, we can write:

$$P_{\text{rad}} = (1 + R)\frac{I}{c}$$

Finally, if the direction of propagation is not normal to Σ, just the normal component of the momentum participates to the interaction and so there's a $\cos\theta$ factor. Also, we

should consider that if the laser cross-section is the same, the spot size is increased and the pressure is reduced, again of a factor $\cos\theta$.

$$P_{\text{rad\_non\_norm}} = (1+R)\frac{I}{c}\cos^2\theta$$

This radiation pressure is at the basis of the RPA mechanism. From the local microscopic point of view, P_{rad} is given by the integral over the target volume of the temporal average of the $\mathbf{J}\times\mathbf{B}$ force over a period. As already said, and confirmed in [69], since the ponderomotive force scales with the inverse of the particle mass, its effect on ions is existent but negligible: the transfer of momentum is again mediated by electrons, which are not heated by the laser now but just pushed away in the forward direction. In general, both TNSA and RPA mechanisms give a contribution in every solid-target laser-plasma experiment. Usually TNSA dominates, but it is observed and there's an agreement in simulations that RPA will become progressively more important at very high intensities (still technically unfeasible), beyond 10^{23} W/cm^2. These considerations are valid only for linearly polarized pulses, since for circularly polarized ones electron heating is strongly suppressed and RPA should dominate even at much lower intensities.

Two different regimes of RPA can be distinguished by the value of the target thickness: the first, for thick targets, that is known as the "hole boring" (HB) regime [70], the second, for thin targets, known as "light sail" (LS) regime [71].

Let's try now to see some basic features in more detail.

When a laser pulse interacts with a particle the rapid oscillations of the field determine a rapid oscillatory transverse motion whereas the pulse envelope causes a longitudinal motion basically through the mechanism or radiation pressure. In order to examine its origin we average the Hamiltonian in order to drop out the effect of the rapid oscillations of the e.m.field. In the Lorentz gauge the Hamiltonian for a non relativistic particle reads

$$H = \frac{1}{2m}(\mathbf{P} - mc\mathbf{a})^2$$

The one period average on the field gives $\langle a\rangle = 0$ and consequently for the ordinary momentum $\mathbf{p} = \mathbf{P} - mc\mathbf{a}$ gives $\langle\mathbf{p}\rangle = \langle\mathbf{P}\rangle$. The averaged Hamiltonian becomes

$$\langle H\rangle = \frac{\langle\mathbf{P}\rangle}{2m} + \frac{mc^2}{2}\langle\mathbf{a}^2\rangle = \frac{\langle\mathbf{p}\rangle}{2m} + \frac{mc^2}{2}\langle\mathbf{a}^2\rangle$$

Choosing $\langle\mathbf{p}\rangle$ as new canonical variable the equations of motion reads

$$\frac{d\mathbf{x}}{dt} = \frac{\langle\mathbf{p}\rangle}{m} \qquad\qquad \frac{d}{dt}\langle\mathbf{p}\rangle = -mc^2\nabla\langle\mathbf{a}^2\rangle$$

In the 1D case given a pulse propagating along z with polarization along y and $a_y = a_0 f(z-ct)\cos(k_0(z-ct))$ accelerates a free particle initially at rest so that it moves with speed

$$\dot{z} = \frac{c}{2}a_0^2 f^2(z-ct)$$

As a consequence supposing $f(z)$ has a support in $[-w_z, 0]$, a particle initially at rest comes back to rest after the pulse has passed by. Within a a plasma the radiation pressure may accelerate particles in the longitudinal motion at a final speed when the pulse has passed by.

In the so called hole boring regime by equating the electrostatic and radiation pressure one estimates the energy gained by a proton according to

$$E_p(\mathrm{MeV}) = \frac{n_c}{n}\, a^2$$

At high values of a, the model of the relativistic is used. In this case a thin layer is considered which is rigidly accelerated by the laser pulse due to radiation pressure. Letting μ be the surface density the equation of motion reads

$$\mu c \frac{d}{dt} \frac{\beta}{\sqrt{1-\beta^2}} = \frac{2I'}{c} = \frac{2I}{c}\, \frac{1-\beta}{1+\beta}$$

where $beta = v/c$, I/c is the pressure in moving frame and I'/c the pressure in the laboratory frame. The pulse shape, whose time duration is τ, is specified by a function $f(u)$ which is positive in the interval $[-1, 1]$ and vanishes elsewhere

$$I = I_0 f\left(\frac{t - x/c}{\tau} - 1\right) \qquad\qquad \int_{-1}^{1} du\, f(u) = 1$$

By solving the equation one finds that a proton initially at rest gains an energy E_p according to

$$E_p = \frac{m_p c^2}{2}\, \frac{\alpha^2}{\alpha + 1}$$

The parameter α is defined by

$$\alpha = \frac{2 I_0\, \tau}{\mu c^2} = \frac{2 I_0\, S\, \tau}{N\, m_p\, c^2} = \frac{2 E_{\mathrm{las}}}{N\, m_p\, c^2}$$

where S is the foil surface assumed to be equal to laser focal spot and $N\, m_p\, c^2 = \mu S\, c^2 = n\, \ell\, S\, c^2$ is the rest energy of the foil. For simplicity we have considered a H foil, so that the proton and electron densities are equal and are both denoted with n. As a consequence the energy of the foil is

$$E_{\mathrm{foil}} = N\, E_p = \frac{N\, m_p c^2}{2} \alpha\, \frac{\alpha}{\alpha + 1} = E_{\mathrm{las}}\, \frac{\alpha}{1 + \alpha}$$

As a consequence the efficiency of the acceleration process

$$\eta = \frac{\alpha}{1 + \alpha}$$

tends to 1 for $\alpha \gg 1$.

We remark that α increases as in the inverse of the foil thickness ℓ since the surface density is $\mu = m_p\, n\, \ell$. However, a lower limit on ℓ is imposed by relativistic transparency for a given intensity, namely for a given value of a. Indeed the foil remain opaque as long as

$$\pi\sigma \geq a \qquad\qquad \sigma = \frac{n\, \ell}{n_{cr}\, \lambda}$$

For a given density and intensity the critical thickness is

$$\ell_{cr} = \lambda\, \frac{a\, n_c}{\pi\, n}$$

We can now express α in terms of σ recalling that the relation between the intensity and a is given by

$$\frac{I_0}{c} = m_e c^2\, n\, a^2$$

Replacing this expression in the definition of α we obtain

$$\alpha = \frac{2 I_0 \tau}{\mu c^2} = \frac{2\, m_e\, c^3\, n\, a^2 \tau}{m_p n\, \ell\, c^2} = 2\, \frac{m_e}{m_p}\, \frac{n_e}{n}\, a^2\, \frac{c\tau}{\ell}$$

Denoting with $\ell_{\rm las} = c\tau$ the laser pulse length we can express α in therms of the normalized density σ obtaining

$$\alpha = 2 \frac{m_e}{m_p}\, \frac{n_e}{n}\, \frac{\lambda}{\ell}\, a^2\, \frac{\ell_{\rm las}}{\lambda} = 2\pi\, \frac{m_e}{m_p}\, \frac{a}{\pi\sigma}\, a\, \frac{\ell_{\rm las}}{\lambda}$$

As a consequence to remain below the transparency limit we must have $\pi\sigma > a$ so that

$$\alpha \leq 2\pi\, \frac{m_e}{m_p}\, a\, \frac{\ell_{\rm las}}{\lambda}$$

Where the maximum value is obtained for $\ell = \ell_{cr}$. Choosing for instance $\ell_{las} = 10\lambda$ we would obtain $\alpha \leq a/31$. At the transparency limit for $a = 100$ we would have $\alpha \simeq 3$ and a proton energy of about 1 GeV. The critical thickness of a frozen H layer whose density is $5\,10^{22}$ cm^{-3} for a 1 μm wavelength would be $\ell_{cr} = 0.6$ μm.

The estimates of the simple one dimensional models have severe limitations since in 3D phenomena like Rayleigh Taylor instabilities can set in, severely limiting the efficiency of the methods and causing a loss of the mono-energetic nature of the beam.

This regime has been investigated, especially during this last year thanks to a PRACE project I was involved in.

Results are still unpublished but, as can be seen from figures 2.6 and 2.7, we can observe that, differently from TNSA, electrons and protons are moving almost together and the laser pulse is not reflected by the target. On the contrary, it destroys completely the foil that is pushed forward with it.

Since it is still not easily accessible experimentally, it was not considered for our simulations on laser-plasma acceleration and injection in a linac, even if for the future it is a very interesting and promising path.

2.5.3 The Magnetic Vortex Acceleration mechanism

Recently, attention has been paid to mechanisms allowing to produce high energy ions using a laser interaction with a near-critical $n_e \simeq n_c$ density plasmas (NCD) [72, 73, 74, 75, 76]. A low intensity laser pulse, impinging on the surface of overcritical $n_e > n_c$ plasma, can be transmitted and absorbed only over a short depth, the largest part of the pulse being reflected. At high intensity $a \gg 1$, relativistic transparency effects allow a laser transmission over a longer distance L_{NCD}, which can be estimated using the standard relation

$$\frac{n_e}{n_c}\, \frac{L_{NCD}}{\lambda_0} \simeq a,$$

where intensities corresponding to values $a = [20 \div 30]$ are considered.

As documented by numerical simulations, during the laser propagation, ponderomotive effects push electrons forward and a low density channel is formed behind the laser pulse, much alike the bubble regime in the under dense plasmas.

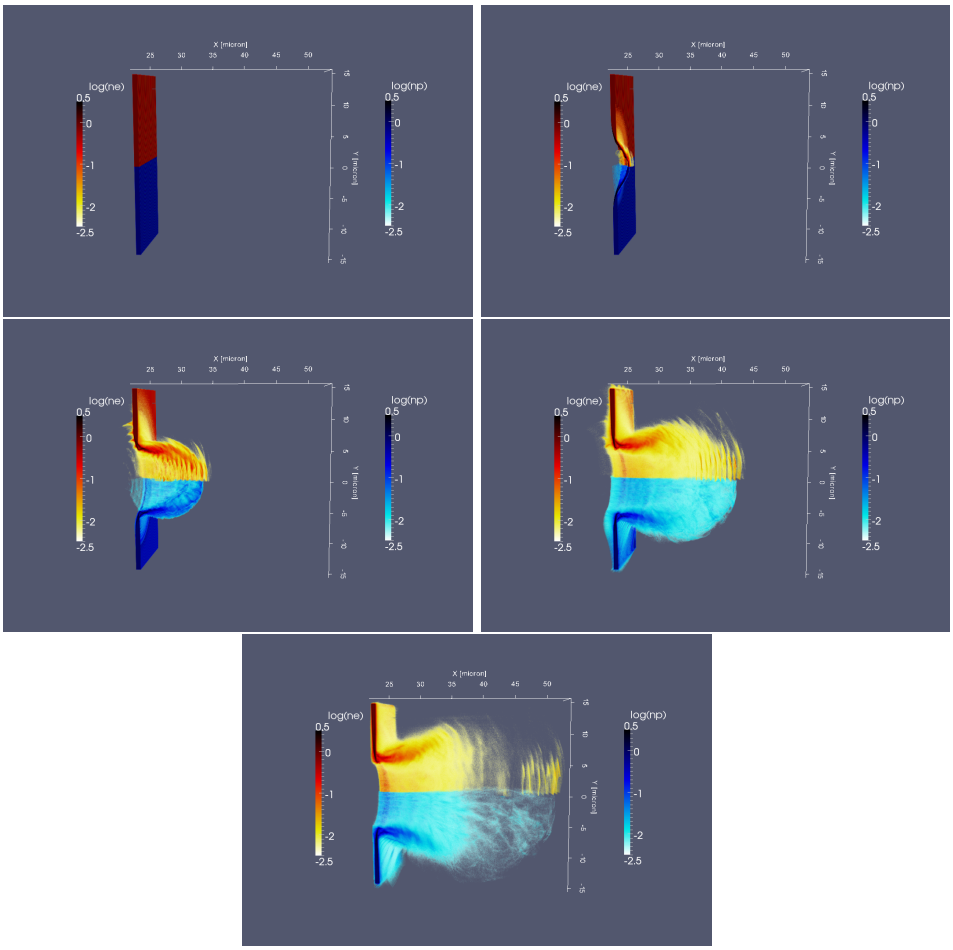

Figure 2.6: RPA acceleration mechanism sequence. In red scale, the electron density is reproduced; in blue scale, is showed the proton density. CP laser: $I_0 = 1.7 \cdot 10^{23}$ W/cm^2, $w_0 = 3.5\mu$m, $\tau = 24$ fs, $\lambda = 0.8\mu$m, plasma formed by electrons and protons, initial thickness $\ell = 0.8\mu$m and density $n_e = 64 n_c$.

The low density channel is characterized by a strong return electron current on the axis and by dense filaments of protons (or ions) on the axis and along the channel boundary. This complex phenomenology can be illustrated by figure 2.8, where a near-critical density laser-plasma configuration is considered, in a 2D simulation.

From these numerical studies, we can show that the energy of the propagating laser pulse is transformed, partly in relativistic particle kinetic energy and partly in the form of a slowly evolving transverse (azimuthal in cylindrical geometry) magnetic field.

The formation of these magnetic structures, for laser pulses propagating in NCD plasmas, has been intensively studied even experimentally, in a general perspective not necessary related to proton accelerations. In fact many studies are pursued to find other applications for these extremely strong magnetic fields that are generated.

Numerical simulations show that to achieve protons (ions) acceleration it is necessary to design a proper target configuration at the exit of the channel. If the NCD plasma experiences a fast transition to a low density material or to vacuum, the azimuthal magnetic field expands and a longitudinal electric fields is induced by the Faraday effect, which accelerates the protons of the end layer of the NCD channel.

For a smooth transition to a lower $(n_e < n_c)$ density plasmas, a model has been proposed, where the expanding magnetic field is transformed in a magnetic vortex around

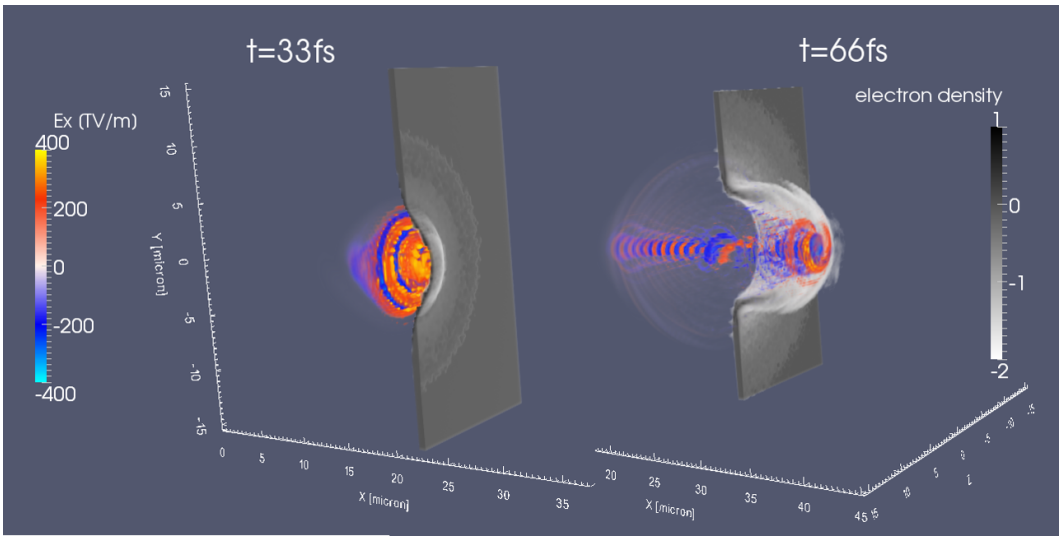

Figure 2.7: Laser pulse pushing target forward during RPA acceleration mechanism. CP laser: $I_0 = 1.7 \cdot 10^{23}$ W/cm^2, $w_0 = 3.5\mu$m, $\tau = 24$ fs, $\lambda = 0.8\mu$m, plasma formed by electrons and protons, initial thickness $\ell = 0.8\mu$m and density $n_e = 64 n_c$.

the channel exit side (Magnetic Vortex Acceleration, MVA) which then acts as a reservoir of relativistic electrons. The acceleration mechanism is then of TNSA type, driven by the electrostatic longitudinal field produced by the trapped electrons ([77]).

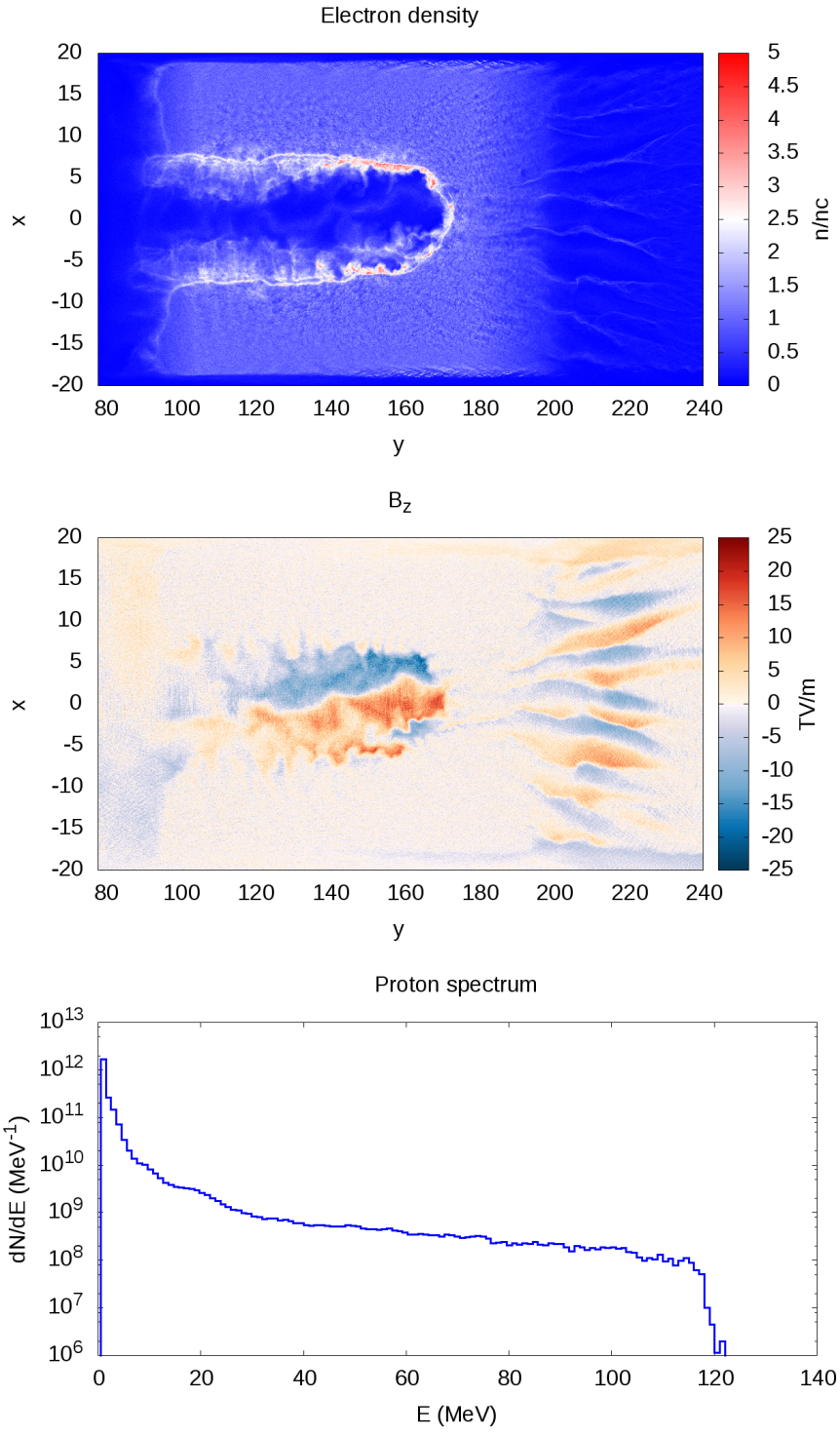

Figure 2.8: An example of Magnetic Vortex Acceleration. In the first frame we can see the electron density, in the second the B_z field and in the third the proton spectrum. $a_0 = 22$, laser power $P = 100$ TW. These shots are taken at $t \approx 250$ fs.

3 Beam shaping

The kind of proton bunches that are produced nowadays from TNSA is extremely poor from a traditional point of view and needs finding different applications and/or ways to improve energy spread and angular divergence.

Otherwise, the risk is just to have a device that produces a huge load of radiations, in form of electrons, X/γ rays, protons, ions, just to have to remove all of them, to keep a small slice of just one species.

Anyway, what we tried at first was just attempting to couple laser-driven proton bunches with conventional beamlines. It was a hard job from the beginning, but blending these two different worlds gave us invaluable knowledge and understanding of the problem.

We tried many different beamline configurations, in order to find which one was working the best for compactness, reliability, beam quality and feasibility.

Although space charge is neglected in our transport simulations (for now), our thoughts are that it acts like a defocusing lens. In an ideal beam with uniform charge density, the self-induced electric field, and hence this defocusing force, are proportional to the radius r and the net effect is an increasing in the focal length. In practice, the charge density is not uniform, and this non uniformity causes spherical aberrations.

3.1 Chicane

Mass spectrometers seem a very easy and reasonable solution to the problem of selecting an energy slice inside a laser-driven proton bunch. And in fact it was the first thing that we tried at the beginning of my PhD [78]. Unfortunately, results were extremely disappointing from many points of view and here it is why.

The biggest problem is the beam divergence. Let's analyze how it works through a study of the Thomson spectrometer.

Let's consider two fields, one magnetic and the other electric, uniform and parallel, inside the region $0 \leq z \leq \ell$.

$$\mathbf{E} = E\mathbf{e_y} \qquad\qquad \mathbf{B} = B\mathbf{e_y}$$

Let's consider first of all the effects of the magnetic field, evaluating how it deflects a particle (an ion) with a charge $q = Ze$ and mass $m = Am_p$, propagating with a speed $v = \beta c$ along z axis.

We can see a schematic drawing in figure 3.1. Since ions describe an arc of radius ρ in the region with the **B** field (let's consider it between $z = 0$ and $z = \ell$), with

$$\ell = \rho \sin\alpha$$

ρ can be obtained forcing an equality between the centripetal force and the Lorentz force.

$$\frac{1}{\rho} = \frac{ZeB}{Am_p vc} = \frac{Z}{A}\frac{\Omega_B}{\beta}$$

where we have defined

$$\Omega_B = \frac{eB}{m_p c^2}$$

Out of the **B** field of course the trajectory is again rectilinear, tangent to the arc that the particle was describing inside the magnetic field.

After the deviation, on the screen the particle position is after the two deflections QA and AB, where

$$QA = \rho(1-\cos\alpha) \qquad AB = d\tan\alpha$$

The total deviation is $x_s = QA + AB = \rho(1-\cos\alpha) + d\tan\alpha$. Let's consider the case in which $\alpha \ll 1$, keeping terms just up to the second order. In this case we can write $\tan\alpha \approx \alpha$, because $\alpha \approx \ell/\rho$, and $1-\cos\alpha \approx \alpha^2/2$.

$$x_s = \rho\frac{\alpha^2}{2} + \alpha d$$

Substituting the α value

$$x_s = \frac{\ell^2}{2\rho} + \frac{d\ell}{\rho} = \frac{\ell}{\rho}\left(d + \frac{\ell}{2}\right) = \frac{Z}{A}\frac{\Omega_B}{\beta}\ell\left(d+\frac{\ell}{2}\right)$$

If we consider now just the electric field, the motion equations for a particle of mass Am_p, charge Ze and initial speed along z equal to v are:

$$Am_p\ddot{y} = Ze\epsilon \qquad \ddot{z} = 0 \tag{3.1}$$

The schematic representation can be found in 3.2.

The solution is

$$y = \frac{1}{2}\frac{Ze\epsilon}{Am_p}t^2 \qquad z = vt \tag{3.2}$$

To determine $Q'A'$ we can say that, at time $t = t_* = \ell/v$,

$$Q'A' = y(t_*) = \frac{1}{2}\frac{Ze\epsilon}{Am_p}\frac{\ell^2}{\beta^2c^2}$$

α is determined by

$$\tan\alpha = \frac{v_y(t_*)}{v_z} = \frac{Ze\epsilon}{Am_p}\frac{\ell}{\beta^2c^2}$$

The deviation made by the electric field can be written as

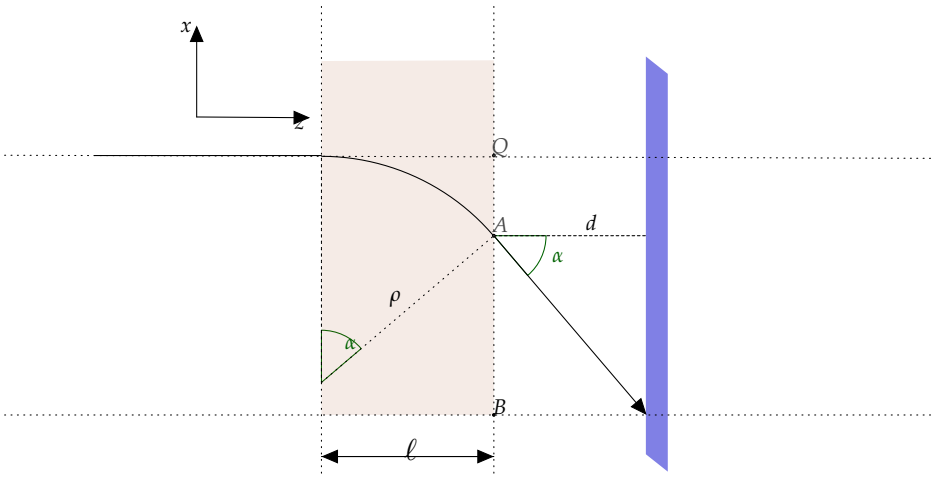

Figure 3.1: B field spectrometer

$$y_s = Q'A' + A'B' = Q'A' + d\tan\alpha = \tag{3.3}$$

$$= \frac{1}{2}\frac{Ze\epsilon}{Am_p}\frac{\ell^2}{\beta^2 c^2} + d\frac{Ze\epsilon}{Am_p}\frac{\ell}{\beta^2 c^2} = \frac{Z}{A}\frac{e\epsilon}{m_p c^2}\frac{\ell}{\beta^2}\left(d + \frac{\ell}{2}\right) = \tag{3.4}$$

$$= \frac{Z}{A}\frac{\Omega_E}{\beta^2}\ell\left(d + \frac{\ell}{2}\right) \tag{3.5}$$

where, similarly to the purely magnetic case, we have defined an Ω_E such that

$$\Omega_E = \frac{e\epsilon}{m_p c^2}$$

Combining both results, we have parabola arcs on the screen, described by

$$y_s = \frac{A}{Z}\frac{\Omega_E}{\Omega_B^2}\frac{x_s^2}{\ell\,(D + \ell/2)}$$

This tool can be used to diagnose the beam if we select a very small fraction of it in an extremely narrow angle. In fact we can use a slit instead of a screen and select an energy slice, as narrow as the aperture diameter. But in order to understand better how to select, let's firstly study a realistic case of a spectrometer to fully appreciate its strengths and weaknesses.

3.1.1 Numerical results for a realistic case

Let's consider a spectrometer with a magnetic field generated by a permanent magnet and two electrodes with a potential difference between them. Some realistic values can be

$$B = 1\ \text{T} \qquad E = 1\ \text{MV/m} \qquad V = 1\ \text{KV} \qquad \ell = 1\ \text{cm} \qquad D = 50\ \text{cm}$$

We can use the approximation

$$E = Am_p c^2\left[\left(1-\beta^2\right)^{-1/2} - 1\right] \simeq Am_p c^2\frac{\beta^2}{2}$$

Let's calculate now the deflection spectrum from the energy one. In order to simplify the calculations, let's go back to have just a magnetic field and a pure exponential energy spectrum for our ions.

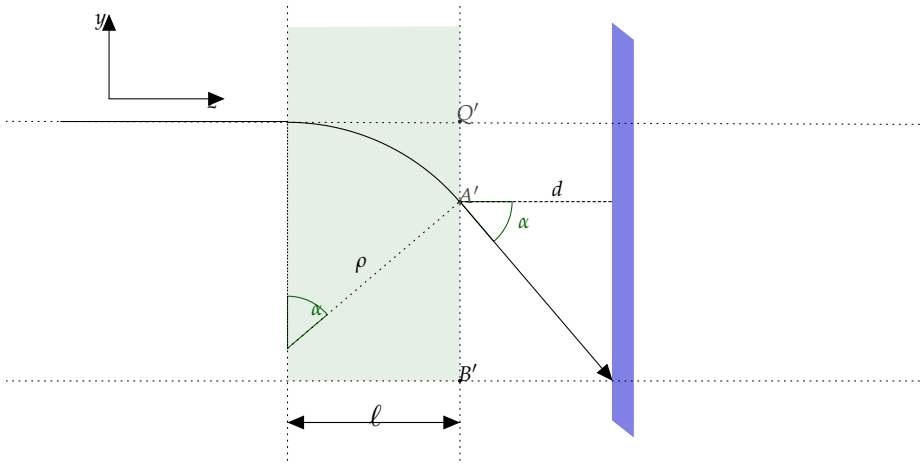

Figure 3.2: E field spectrometer

$$\frac{dN}{dE} = N_0 \rho(E) \qquad\qquad \rho(E) = \frac{1}{E_0} e^{-E/E_0}$$

where we have chosen for simplicity $\int_0^\infty \rho(E)dE = 1$ and where $\langle E \rangle = E_0$ is the average energy.

Let's calculate the x distribution, that is

$$\hat{\rho}(x)dx = \rho(E)dE$$

In order to do that, it's better to first define

$$k = \frac{Z}{A}\Omega_B \ell \left(D + \frac{\ell}{2}\right)$$

so that

$$x = \frac{k}{\beta} \tag{3.6}$$

Since

$$E = m_p c^2 \frac{\beta^2}{2} = \frac{E_{\text{ion}}}{A}$$

and

$$E_0 = m_p c^2 \frac{\beta^2}{2}$$

we can write

$$\hat{\rho}(x) = \rho(E) \tfrac{dE}{d\beta} / \left|\tfrac{dx}{d\beta}\right| = \rho(E) m_p c^2 \beta \frac{\beta^2}{k} = m_p c^2 \frac{\beta^3}{k} \rho(E)$$

and so the distribution of the deviations along x, that is $\rho(x)$, is described by

$$\hat{\rho}(x) = \frac{2\beta^2}{k\beta_0^2} e^{-\beta^2/\beta_0^2}$$

$$\hat{\rho}(x)dx = -e^{-\beta^2/\beta_0^2} \frac{2\beta d\beta}{\beta_0^2} = -e^{-\beta^2/\beta_0^2} \frac{d\beta^2}{\beta_0^2}$$

where the $-$ sign is explained by the fact that the β interval $[0, +\infty]$ is transformed into $[+\infty, 0]$. Substituting 3.6 we obtain

$$\hat{\rho}(x) = \frac{2x_0^2}{x^3} e^{-x_0^2/x^2}$$

where $x_0 = k/\beta_0$.

If we study the resulting distribution function, we can find that there's a maximum at $x = x_M$:

$$\frac{d\hat{\rho}}{dx} = \left(-6\frac{x_0^2}{x^4} + 4\frac{x_0^4}{x^6}\right) e^{-x_0^2/x^2} = 0 \qquad \longrightarrow \qquad x_M = \left(\frac{2}{3}\right)^{1/2} x_0$$

which correspond to a value of β_M of

$$\beta_M = \left(\frac{3}{2}\right)^{1/2} \beta_0 \qquad \longrightarrow \qquad E_M = m_p c^2 \frac{\beta_M^2}{2} = \frac{3}{2} m_p c^2 \frac{\beta_0^2}{2} = \frac{3}{2} E_0$$

Note that β_M is not the maximum of $\overline{\rho}(\beta)$, since $\hat{\rho}(x) = \overline{\rho}(\beta)|d\beta/dx| = \overline{\rho}(\beta)\beta^2/k$. In fact, the maximum of $\overline{\rho}(\beta)$ is $\beta_{\max} = \beta_0$.

A device using just magnetic fields and apertures, properly configured along the way, is one of the simplest tool to do some energy selections and diagnostics on a beam. In fact it was the first device I studied during the PhD to "clean" a laser-driven proton bunch [78] and it's used in many experiments to study the bunch properties. But until now, as we have seen, we have never discussed about transverse momenta. This is a serious issue for a Thomson spectrometer and in fact it's always used after two very narrow pinholes, in order to guarantee that the protons going inside have not any velocity on the plane perpendicular to the main direction of motion.

What happens if we try to include some transverse speed?

3.1.2 A more realistic case using complex distributions

From PIC simulations of laser-driven proton acceleration, the spectra are always exponential-like in energy, with an upper cutoff, and Mexican-hat style in angle θ, where

$$p_\perp = p_z \tan\theta \quad \text{and} \quad \mathbf{p} = \mathbf{p}_\perp + \mathbf{p_z}.$$

z is the reference direction for the proton bunch motion. Along the other angle ϕ, the one that describes a rotation around z, we can assume a uniform distribution since a cylindrical symmetry is perfectly justifiable.

In order to simplify our calculations a little, let's assume that we cut the θ distribution at a certain $\theta_{\max}$ thanks to a collimator and that the Mexican-hat distribution is instead uniform. Let's also consider just a deflection along x. A schematic draw can be found in fig. 3.3.

The position x_s of the particle on the screen is given by

$$-x_s = QA + AB = Q'A' + D\tan(\theta + \alpha) \tag{3.7}$$

Since $\Theta = A'\hat{O}Q'$ is

$$\Theta = 2\pi - \left(\pi - \theta + \frac{\pi}{2} + \frac{\pi - \alpha}{2}\right) = \theta + \frac{\alpha}{2}$$

we can write

$$Q'A' = OA' \sin\Theta = OA' \sin\left(\theta + \frac{\alpha}{2}\right)$$

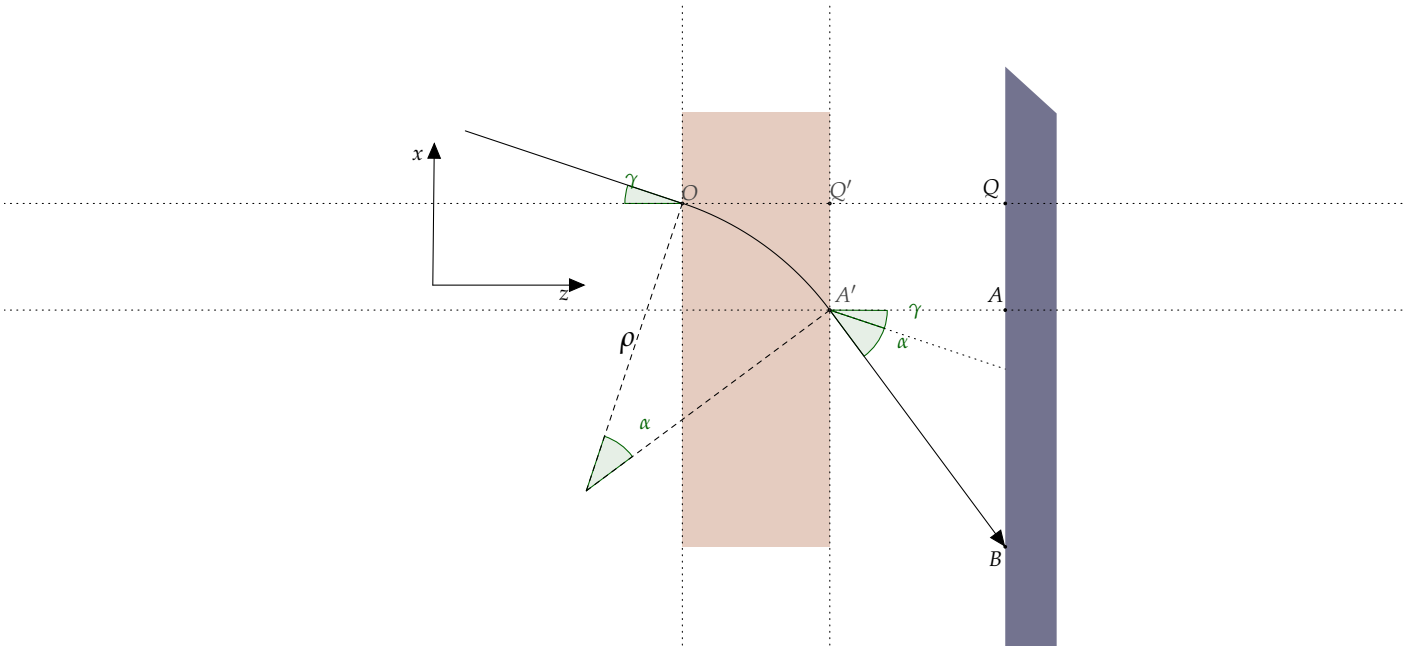

Figure 3.3: B field spectrometer with non-normal incidence

From the isosceles triangle COA' we have that

$$OA' = 2\rho \cos\left(\frac{\pi - \alpha}{2}\right) = 2\rho \sin\frac{\alpha}{2}$$

so that

$$Q'A' = 2\rho \sin\frac{\alpha}{2} \sin\left(\theta + \frac{\alpha}{2}\right) \tag{3.8}$$

With normal incidence, we find again

$$Q'A' = 2\rho \sin^2\frac{\alpha}{2} = \rho(1 - \cos\alpha)$$

being $\ell = \rho \sin\alpha$ we have

$$Q'A' = 2\ell\frac{\sin^2(\alpha/2)}{\sin\alpha} = \ell \tan\left(\frac{\alpha}{2}\right)$$

Back to the general case, inserting 3.8 into 3.7 we have

$$-x_s = 2\rho \sin\frac{\alpha}{2} \sin\left(\theta + \frac{\alpha}{2}\right) + D\tan(\theta + \alpha)$$

When $\theta \ll 1$ and $\alpha \ll 1$ we can write $\ell = \rho \sin\alpha \approx \rho\alpha$ so that

$$-x_s = \rho\alpha\left(\theta + \frac{\alpha}{2}\right) + D(\theta + \alpha) = \frac{\ell}{\rho}\left(D + \frac{\ell}{2}\right) + D(\theta + \ell)$$

Remembering that

$$\frac{1}{\rho} = \frac{Z}{A}\frac{\Omega_B}{\beta}$$

and defining k as

$$k = \frac{Z}{A}\Omega_B \ell \left(D + \frac{\ell}{2}\right)$$

we can rewrite the result as

$$-x_s = \frac{k}{\beta} + \theta(D + \ell)$$

This is a simple yet almost general case to describe how a chicane works, both from the energy selection point of view and the detector behavior.

During my PhD I was one of the tutor of S. Basile, that wrote his master thesis on this topic.

3.2 Quadrupole

In a behavior similar to light rays, also particle beams have a tendency to spread out thanks to an inherent beam divergence. This is true for conventional beams, mainly because of the self-interaction of particles with the same charge. It becomes extremely true for laser-driven bunches because the acceleration models themselves cause an initial strong divergence in the bunch.

To keep particle beam together and not having to select just those propagating along the axis as we were doing with the chicane, we can use focusing devices. As in optical lenses, the properties of these devices must be that the "particle rays" must be deflected by an angle proportional to the distance of the ray from the center of the "lens", in order for them to work.

Any magnetic field that deflects a particle by an angle proportional to its distance r from the axis of the focusing device will act in the same way as a glass lens does in the approximation of paraxial, geometric optics for visible light [79]. If f is the focal length, the deflection angle α is defined by

$$\alpha = -\frac{r}{f} \tag{3.9}$$

Charged particles passing through alternating field gradients receive a strong focusing effect and the net result is a beam convergence.

Strong focusing was first conceived by N. Christofilos in 1949 [80], but was almost unnoticed before it was independently developed by E. Courant, M. S. Livingston, H. Snyder [81] and J. Blewett [82] at Brookhaven National Laboratory. Afterward, they recognized the priority of Christofilos' idea but it was just after their work that the advantages of this technique were realized, and deployed in some particle accelerators.

Courant and Snyder found that the net effect of alternating the field gradient was that both the vertical and horizontal focusing of protons could be made strong at the same time, allowing tight control of proton paths in the machine. This increased beam intensity, while reducing the overall construction cost of a more powerful accelerator.

Quadrupole fields are a special case of cylindrical multipole fields, which satisfy the condition $\nabla \cdot \mathbf{E} = 0$ and $\nabla \times \mathbf{B} = 0$. The variation of the radial field component is proportional to $f(z)r^{n-1}\cos[2(n-1)\theta]$ [83].

A magnetic quadrupole field is described by

$$B_r = \frac{B_0 r}{a}\sin 2\theta \qquad\qquad B_\theta = \frac{B_0 r}{a}\cos 2\theta$$

or, in Cartesian coordinates,

$$B_y = B_0\frac{x}{a} \qquad\qquad B_x = B_0\frac{y}{a}$$

where a is the radius of the inner quadrupole bore.

The equations of motion are

$$\gamma m\ddot{x} = -qv_z B_y = -qv_z \frac{B_0}{a} x \qquad \gamma m\ddot{y} = -qv_z B_x = -qv_z \frac{B_0}{a} y$$

or

$$\ddot{x} + \frac{qv_z B_0}{\gamma m a} x = 0$$
$$\ddot{y} - \frac{qv_z B_0}{\gamma m a} y = 0$$

These equations are in the form $\ddot{\zeta} \pm \omega_0^2 \zeta = 0$, that have solutions $\zeta = A\cos\omega_0 t + B\sin\omega_0 t$ or $\zeta = A\cosh\omega_0 t + B\sinh\omega_0 t$ depending on the sign.

We can simplify the formalism of these equations eliminating the time t, rewriting the equations as trajectory equations.

Noting that $z = v_z t$, $v_z \approx v \approx$ const, $d^2/dt^2 = v^2\left(d^2/dz^2\right)$ we have

$$\begin{cases} x'' + kx &= 0 \\ y'' - ky &= 0 \end{cases} \tag{3.10}$$

where

$$k = \frac{qB_0}{\gamma m a v}$$

With initial conditions $x = x_0$, $x' = x'_0$, $y = y_0$, $y' = y'_0$ at $z = 0$, the solution is

$$x = x_0 \cos\sqrt{k}z + \frac{x'_0}{\sqrt{k}} \sin\sqrt{k}z$$
$$x' = -\sqrt{k}x_0 \sin\sqrt{k}z + x'_0 \cos\sqrt{k}z$$

that we can write in matrix form as

$$\begin{pmatrix} x \\ x' \end{pmatrix} = \begin{pmatrix} \cos\sqrt{k}z & \frac{1}{\sqrt{k}}\sin\sqrt{k}z \\ -\sqrt{k}\sin\sqrt{k}z & \cos\sqrt{k}z \end{pmatrix} \begin{pmatrix} x_0 \\ x'_0 \end{pmatrix}$$

and

$$\begin{pmatrix} y \\ y' \end{pmatrix} = \begin{pmatrix} \cosh\sqrt{k}z & \frac{1}{\sqrt{k}}\sinh\sqrt{k}z \\ \sqrt{k}\sinh\sqrt{k}z & \cosh\sqrt{k}z \end{pmatrix} \begin{pmatrix} y_0 \\ y'_0 \end{pmatrix}$$

As well described in [83], usually the lens approximation is valid if the quadrupole length $\Delta z = \ell$ is greater than the semi-aperture a, but less than $\sqrt{k}$.

In fact, there is a fringe field outside of the ideal quadrupole that forms a transition to the field-free region; however, if we fall under previous conditions, we can use an equivalent hard-edge approximation that is perfectly valid for the paraxial analysis.

Quadrupole lenses can have two different orientations: F quadrupoles are horizontally focusing but vertically defocusing and D quadrupoles are vertically focusing but horizontally defocusing.

A schematic representation of the magnetic field lines inside a quadrupole can be found in figure 3.4.

As can be seen from the picture of the field lines, it's impossible for a quadrupole to focus in both planes at the same time, but if two of them are placed in sequence, then the overall effect is what we were looking for. Of course, if we place an F and a D quadrupole

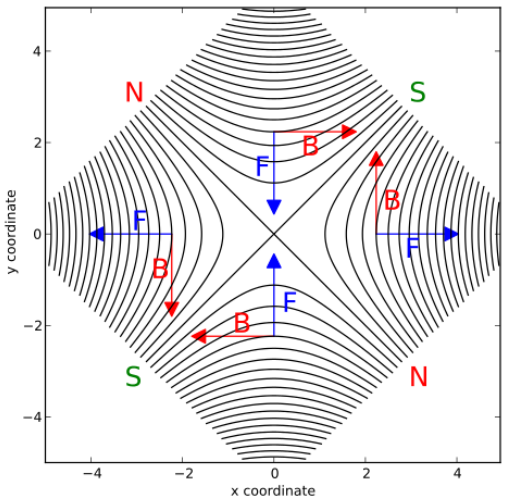

Figure 3.4: Magnetic field of an idealized quadrupole with forces.

immediately next to each other, the field lines change and they do not flow inside the same quadrupole, but they flow from one to the other, completely canceling out the field inside them.

This is the reason why, usually, lattices built from quadrupoles are called FODO: O stands for "nothing", it's just simple drift, between the quadrupoles.

The equations 3.10 cannot be solved in general since the k parameter is determined by the distribution itself, but integrating them over a short distance Δz we can calculate the deflection angle:

$$\alpha = y' - y'_0 = \int_{z_0}^{z_0+\Delta z} y'' dz$$

On the other hand, if the gradients are not "extreme", we can write

$$\int k y dz \approx k y \Delta z$$

and so, applying 3.9, we can write

$$\frac{1}{f_x} = +k\Delta z = +\frac{e}{cp}\frac{\partial B_y}{\partial x}\Delta z$$
$$\frac{1}{f_y} = -k\Delta z = -\frac{e}{cp}\frac{\partial B_x}{\partial y}\Delta z$$

In an attempt to solve the equations of motion 3.10, we have to note that the principal solutions of those differential equations are

$$\begin{cases} C(z) = \cos\left(\sqrt{k}z\right) \\ S(z) = \dfrac{1}{\sqrt{k}}\sin\left(\sqrt{k}z\right) \end{cases} \qquad \text{for } k > 0$$

$$\begin{cases} C(z) = \cosh\left(\sqrt{|k|}z\right) \\ S(z) = \dfrac{1}{\sqrt{|k|}}\sinh\left(\sqrt{|k|}z\right) \end{cases} \qquad \text{for } k < 0$$

Identifying with u both x or y, any arbitrary solution can be expressed as a linear combination of those two principal solutions:

$$u(z) = C(z)u_0 + S(z)u_0'$$
$$u'(z) = C'(z)u_0 + S'(z)u_0'$$

(derivatives are with respect to the independent variable z).

These solutions can be expressed in a matrix form:

$$\begin{pmatrix} u(z) \\ u'(z) \end{pmatrix} = \begin{pmatrix} C(z) & S(z) \\ C'(z) & S'(z) \end{pmatrix} \cdot \begin{pmatrix} u_0 \\ u_0' \end{pmatrix}$$

With this formulation, we are ready to follow a particle trajectory along a complicated beam line by repeating matrix multiplications from element to element.

3.2.1 A beamline with quadrupoles

Let's first recap the matrix form for each element of a FODO lattice. For a drift space, it's easy to see that

$$\begin{pmatrix} u(z) \\ u'(z) \end{pmatrix} = \begin{pmatrix} 1 & \ell \\ 0 & 1 \end{pmatrix} \cdot \begin{pmatrix} u_0 \\ u_0' \end{pmatrix}$$

As expected, the distance from the axis changes only if the trajectory has an initial non-vanishing slope $u_0' \neq 0$, while this transverse speed doesn't change at all.

For a quadrupole, the 'strength' k can be positive as well as negative, as we have seen, depending on if it's a focusing F or defocusing D quadrupole. For $k > 0$

$$\begin{pmatrix} u(z) \\ u'(z) \end{pmatrix} = \begin{pmatrix} \cos\psi & \frac{1}{\sqrt{k}}\sin\psi \\ -\sqrt{k}\sin\psi & \cos\psi \end{pmatrix} \cdot \begin{pmatrix} u(z_0) \\ u'(z_0) \end{pmatrix}$$

where $\psi = \sqrt{k}(z - z_0)$, for every z and z_0 that lies inside the same quadrupole.

For a full focusing quadrupole of length ℓ and strength k, we can set $\phi = \sqrt{k}\ell$ and the transformation matrix becomes

$$\begin{pmatrix} u_{\text{end}} \\ u'_{\text{end}} \end{pmatrix} = \begin{pmatrix} \cos\psi & \frac{1}{\sqrt{k}}\sin\psi \\ -\sqrt{k}\sin\psi & \cos\psi \end{pmatrix} \cdot \begin{pmatrix} u_{\text{beginning}} \\ u'_{\text{beginning}} \end{pmatrix}$$

The transformation matrix for a defocusing quadrupole of length ℓ and $\phi = \sqrt{k}\ell$ is therefore:

$$\begin{pmatrix} u_{\text{end}} \\ u'_{\text{end}} \end{pmatrix} = \begin{pmatrix} \cosh\psi & \frac{1}{\sqrt{|k|}}\sinh\psi \\ \sqrt{|k|}\sinh\psi & \cosh\psi \end{pmatrix} \cdot \begin{pmatrix} u_{\text{beginning}} \\ u'_{\text{beginning}} \end{pmatrix}$$

Now that we have the ingredients, the transformation matrix for an arbitrary sequence of drift spaces and quadrupoles can be easily obtained from the product of the individual matrices; for example, for a lattice composed of 10 elements, the total transformation would be:

$$\mathcal{M} = \mathcal{M}_{10} \ldots \mathcal{M}_5 \mathcal{M}_4 \mathcal{M}_3 \mathcal{M}_2 \mathcal{M}_1$$

and the particle trajectory would be summed up by

$$\begin{pmatrix} u(z) \\ u'(z) \end{pmatrix} = \mathcal{M}(z|z_0) \begin{pmatrix} u(z_0) \\ u'(z_0) \end{pmatrix}$$

This is an extremely useful formalism to describe and calculate trajectories for a single particle or even for a virtual particle representing the central path of a whole beam. This multiplication is easily performed on a computer.

Sometimes, it's useful to calculate analytically the approximate properties of a small set of elements; in these cases, we can use what is called the thin lens approximation. In this approximation, it's assumed that the length of the quadrupole is small with respect to the focal length, so that we can assume $\ell \to 0$ keeping the focal strength constant.

In this approximation, we can simplify $\sin\psi \to \psi$, $\sinh\psi \to \psi$, $\cos\psi \to 1$ and $\cosh\psi \to 1$ so that

$$\mathcal{M}_F = \begin{pmatrix} 1 & \frac{1}{\sqrt{k}}\psi \\ -\sqrt{k}\psi & 1 \end{pmatrix} = \begin{pmatrix} 1 & 0 \\ -k\ell & 1 \end{pmatrix}$$

$$\mathcal{M}_D = \begin{pmatrix} 1 & \frac{1}{\sqrt{|k|}}\psi \\ \sqrt{|k|}\psi & 1 \end{pmatrix} = \begin{pmatrix} 1 & 0 \\ k\ell & 1 \end{pmatrix}$$

Let's consider a line composed of $\to \mathsf{O}_1 \to \mathsf{D} \to \mathsf{O}_2 \to \mathsf{F} \to$, where the arrows define the beam direction. F and D quadrupoles have the same strength and so the same focal length f, while the two drifts have lengths of L_1 and L_2. In the $\mathbb{R}^2_x$ plane, with $\mathbf{x} = (x, x')$ and $x' = dx/ds$ (s is the curvilinear path) the single transport matrices are the following:

$$\mathsf{F} = \begin{pmatrix} 1 & 0 \\ -\frac{1}{f} & 1 \end{pmatrix} \qquad \mathsf{D} = \begin{pmatrix} 1 & 0 \\ \frac{1}{f} & 1 \end{pmatrix} \qquad \mathsf{O} = \begin{pmatrix} 1 & L \\ 0 & 1 \end{pmatrix}$$

The total transfer matrix is:

$$\mathsf{M}_x = \mathsf{FO_2DO_1} = \begin{pmatrix} 1 + \frac{L_2}{f} & L_1 + L_2 + \frac{L_1 L_2}{f} \\ -\frac{L_2}{f^2} & 1 - \frac{L_2}{f} - \frac{L_1 L_2}{f^2} \end{pmatrix}$$

Since the two quadrupoles are identical except for a 90° rotation, we can say that the full transfer matrix in the $\mathbb{R}^2_y$ plane, with $\mathbf{y} = (y, y')$ and $y' = dy/ds$, can be expressed using the matrices for the $\mathbb{R}^2_x$ plane just exchanging the F and D terms:

$$\mathsf{M}_y = \mathsf{DO_2FO_1} = \begin{pmatrix} 1 - \frac{L_2}{f} & L_1 + L_2 - \frac{L_1 L_2}{f} \\ -\frac{L_2}{f^2} & 1 + \frac{L_2}{f} - \frac{L_1 L_2}{f^2} \end{pmatrix}$$

This is quite a common result in beam transport literature, since a FODO line is the most common one.

Let's add another drift O_3 of length L_3 after the final F. This is because at the end of this other drift we want another focus. We found that it was possible to do beam shaping and energy selection using just quadrupoles [84]. Starting from a laser-driven proton source in $\mathbf{x} = (0, x'_0)$ and $\mathbf{y} = (0, y'_0)$, we want to have another focus for both planes at a certain $\mathbf{z}_f$ position.

The full transfer matrices are

$$\begin{aligned} \overline{\mathsf{M}}_x &= \mathsf{O_3 M}_x = \mathsf{O_3 FO_2 DO_1} = \\ &= \begin{pmatrix} 1 + \frac{L_2}{f} - \frac{L_2 L_3}{f^2} & L_1 + L_2 + \frac{L_1 L_2}{f} + L_3\left(1 - \frac{L_2}{f} - \frac{L_1 L_2}{f^2}\right) \\ -\frac{L_2}{f^2} & 1 - \frac{L_2}{f} - \frac{L_1 L_2}{f^2} \end{pmatrix} \end{aligned}$$

and

$$\overline{\mathsf{M}}_y = \mathsf{O}_3\mathsf{M}_y = \mathsf{O}_3\mathsf{D}\mathsf{O}_2\mathsf{F}\mathsf{O}_1 = \\ = \begin{pmatrix} 1 - \frac{L_2}{f} - \frac{L_2 L_3}{f^2} & L_1 + L_2 - \frac{L_1 L_2}{f} + L_3\left(1 + \frac{L_2}{f} - \frac{L_1 L_2}{f^2}\right) \\ -\frac{L_2}{f^2} & 1 + \frac{L_2}{f} - \frac{L_1 L_2}{f^2} \end{pmatrix}$$

Imposing in $\mathbf{z}_f$ that $\mathbf{x}_f = (0, x'_{0f})$ and $\mathbf{y}_f = (0, x'_{0f})$:

$$\begin{pmatrix} x_f \\ x'_f \end{pmatrix} = \overline{\mathsf{M}}_x \begin{pmatrix} 0 \\ x'_0 \end{pmatrix} \qquad \begin{pmatrix} y_f \\ y'_f \end{pmatrix} = \overline{\mathsf{M}}_y \begin{pmatrix} 0 \\ y'_0 \end{pmatrix}$$

we obtain a condition on L_3^x and L_3^y that is

$$L_3^x = -\frac{L_1 + L_2 + \frac{L_1 L_2}{f}}{1 - \frac{L_2}{f} - \frac{L_1 L_2}{f^2}} \qquad L_3^y = L_3^x = -\frac{L_1 + L_2 - \frac{L_1 L_2}{f}}{1 + \frac{L_2}{f} - \frac{L_1 L_2}{f^2}} \tag{3.11}$$

Since we need that the foci are overlapped at the same z, so that they are the same on both planes, we must match the two results

$$L_3^x = L_3^y \quad \longrightarrow \quad \frac{L_1^2 L_2}{f^2} = 2L_1 + L_2$$

Fixing L_1 and L_2 we can obtain f:

$$f = \left(\frac{L_1^2 L_2}{2L_1 + L_2}\right)^{1/2}$$

If we substitute this f in 3.11 we obtain that $L_3^x = L_3^y = L_1$. We have found a very precise value for a point in which our beam gets refocused, almost replicating the initial conditions at the source (the initial point): this happens at a distance $d = L_1 + L_2 + L_1 = 2L_1 + L_2$.

This map can also be iterated as many times as we want, since it's easy to find that at each $z = n(2L_1 + L_2)$ the beam is refocused. Unfortunately, on the other hand, the transverse speeds increase and so the beam divergence. This can lead to losses inside the lattice and so a plain repetition of the structure should be avoided as much as possible. In fact, if we now consider a lattice as follows:

$$\to \mathsf{O}_1 \to \mathsf{D} \to \mathsf{O}_2 \to \mathsf{F} \to \mathsf{O}_1 \to \mathsf{O}_1 \to \mathsf{O}_1 \to \mathsf{F} \to \mathsf{O}_2 \to \mathsf{D} \to \mathsf{O}_1 \to$$

because of its symmetry, we can say that at the $z = 2(2L_1 + L_2)$ we have a focal point again, with the peculiar condition that $x'_f = x'_{0f}$ and equally $y'_f = y'_{0f}$. Unfortunately, if the initial point has not $x_0 = 0$, but for example $x_0 > 0$, we find that x'_f grows. Iterating n times we find that

$$x_n = x_0 \qquad \text{but also} \qquad x'_n = x'_0 + n\lambda x_0$$

3.2.2 Thick lenses

In case of a thick lens, the **B** field can be expressed as

$$\mathbf{B} = B'y\mathbf{e}_x + B'x\mathbf{e}_y$$

If the speed is $\mathbf{v} = \dot{x}\mathbf{e}_x + \dot{y} + \mathbf{e}_y + v_0\mathbf{e}_z$ and $|\dot{x}|, |\dot{y}| \ll v_0$, Lorentz force is given by

$$\mathbf{F} = \frac{ev_0 B'}{c}(-x\mathbf{e}_x + y\mathbf{e}_y)$$

Motion equations are given by

$$m\ddot{x} = -\frac{ev_0B'}{c}x \qquad m\ddot{y} = \frac{ev_0B'}{c}y$$

where m and e are mass and charge of the proton. If we use $s = v_0t$ as the longitudinal variable

$$m\frac{d^2x}{ds^2} = -\frac{eB'}{mv_0c}x \qquad m\frac{d^2y}{ds^2} = \frac{eB'}{mv_0c}y$$

In a quadrupole typically the maximum field B_0 is at the edge and d is the separation between the edges. In this case we can assume $B' = B_0/d$

It's useful to define

$$k = \frac{eB'}{mv_0c}\frac{1}{\beta} = \frac{eB_0}{mc^2}\frac{1}{\beta d}$$

Using this definition, the matrices in $\mathbb{R}^2_x$ are given by the evolutions described by

$$\frac{d^2x}{ds^2} + kx = 0 \qquad \frac{d^2y}{ds^2} - ky = 0$$

If L_Q is the quadrupole length and $\alpha = \sqrt{k}L_Q$, we can write

$$\mathsf{F} = \begin{pmatrix} \cos\alpha & k^{-1/2}\sin\alpha \\ -k^{1/2}\sin\alpha & \cos\alpha \end{pmatrix} \qquad \mathsf{D} = \begin{pmatrix} \cosh\alpha & k^{-1/2}\sinh\alpha \\ k^{1/2}\sinh\alpha & \cosh\alpha \end{pmatrix}$$

$$\mathsf{O} = \begin{pmatrix} 1 & L \\ 0 & 1 \end{pmatrix}$$

If we consider now a line

$$\rightarrow \mathsf{O}_1 \rightarrow \mathsf{D} \rightarrow \mathsf{O}_2 \rightarrow \mathsf{F} \rightarrow$$

the full transfer matrix in $\mathbb{R}^2_x$ is

$$\mathsf{M}^x = \mathsf{F}\mathsf{O}_2\mathsf{D}\mathsf{O}_1 = \begin{pmatrix} \mathsf{M}^x_{11} & \mathsf{M}^x_{12} \\ \mathsf{M}^x_{21} & \mathsf{M}^x_{22} \end{pmatrix}$$

where

$$\begin{aligned}
\mathsf{M}^x_{11} &= \cos\alpha\cosh\alpha + L_2\sqrt{k}\cos\alpha\sinh\alpha + \sin\alpha\sinh\alpha \\
\mathsf{M}^x_{12} &= L_1\cos\alpha\cosh\alpha + k^{-1/2}\cos\alpha\sinh\alpha + L_2\cos\alpha\cosh\alpha + \\
&\quad + L_1L_2\sqrt{k}\cos\alpha\sinh\alpha + k^{-1/2}\sin\alpha\cosh\alpha + L_1\sin\alpha\sinh\alpha \\
\mathsf{M}^x_{21} &= -\sqrt{k}\sin\alpha\cosh\alpha + \sqrt{k}\cos\alpha\sinh\alpha - L_2k\sin\alpha\sinh\alpha \\
\mathsf{M}^x_{22} &= -L_1\sqrt{k}\sin\alpha\cosh\alpha - \sin\alpha\sinh\alpha + \cos\alpha\cosh\alpha + \\
&\quad + L_1\sqrt{k}\cos\alpha\sinh\alpha - L_2\sqrt{k}\sin\alpha\cosh\alpha - L_1L_2k\sin\alpha\sinh\alpha
\end{aligned}$$

Let's symmetrize the previous line:

$$\rightarrow \mathsf{O}_1 \rightarrow \mathsf{D} \rightarrow \mathsf{O}_2 \rightarrow \mathsf{F} \rightarrow \mathsf{O}_1 \rightarrow$$

Its transfer matrix is

$$\begin{aligned}
\overline{\mathsf{M}}^x &= \mathsf{O}_1\mathsf{F}\mathsf{O}_2\mathsf{D}\mathsf{O}_1 = \mathsf{O}_1\mathsf{M}^x = \begin{pmatrix} 1 & L_1 \\ 0 & 1 \end{pmatrix}\begin{pmatrix} \mathsf{M}^x_{11} & \mathsf{M}^x_{12} \\ \mathsf{M}^x_{21} & \mathsf{M}^x_{22} \end{pmatrix} = \\
&= \begin{pmatrix} \mathsf{M}^x_{11} + L_1\mathsf{M}^x_{21} & \mathsf{M}^x_{12} + L_1\mathsf{M}^x_{22} \\ \mathsf{M}^x_{21} & \mathsf{M}^x_{22} \end{pmatrix}
\end{aligned}$$

In order that we have another focus at $z = L_1 + L_Q + L_2 + L_Q + L_1 = 2L_1 + L_2 + 2L_Q$ we must have

$$\overline{\mathsf{M}}^x \begin{pmatrix} 0 \\ x'_0 \end{pmatrix} = x'_0 \begin{pmatrix} \mathsf{M}^x_{12} + L_1 \mathsf{M}^x_{22} \\ \mathsf{M}^x_{22} \end{pmatrix} = \begin{pmatrix} 0 \\ x' \end{pmatrix}$$

This means that $\mathsf{M}^x_{12} + L_1 \mathsf{M}^x_{22}$ must be zero. This is not trivial, since the full expression is extremely complicated:

$$\begin{aligned} \mathsf{M}^x_{12} + L_1 \mathsf{M}^x_{22} = {} & (2L_1 + L_2)\cos\alpha\cosh\alpha + L_1^2 L_2 \sqrt{k}\cos\alpha\sinh\alpha + \\ & - L_1^2 L_2 \sqrt{k}\sin\alpha\cosh\alpha + k^{-1/2}\sin\alpha\cosh\alpha(1 - L_1^2 k) \\ & + k^{-1/2}\cos\alpha\sinh\alpha(1 + L_1^2 k) - L_1^2 L_2 k \sin\alpha\sinh\alpha = 0 \end{aligned}$$

We can just give an analytical result in the case $L_1 = L_2 = 0$, which simplifies to

$$\cos\alpha\sinh\alpha + \cosh\alpha\sin\alpha = 0$$

Unfortunately the results are not realistic, since

$$\alpha = 2.365,\ 5.5,\ 8.64,\ \ldots$$

If we choose $\sqrt{k} \sim 0.1$, an ordinary value for a quadrupole, we would have that the shortest quadrupole would have a length $L_Q = \alpha/\sqrt{k} \approx 22$ cm, exaggeratedly long. Also, this analytic case is absurd since we cannot put two quadrupoles close, side by side: the magnetic field lines, as already said, would collapse between the two, removing any field from the bore.

So, in order to build a line that works with quadrupoles for proton transport and energy selection, we proceeded fixing some parameters and doing some numerical simulations, in order to obtain realistic parameters.

Some results with beamlines based on a multiplet of quadrupoles are presented in chapter 4.2.2.

During my PhD I was the tutor of J. S. Pelli Cresi that wrote his bachelor thesis on this topic.

3.3 Solenoid

The solenoid has been found as the most effective device to do beam shaping and energy selection for laser-driven proton acceleration [85].

Let's consider a solenoid of length L, with a uniform $\mathbf{B} = B_0\mathbf{e}_z$ field inside it (z is the solenoid axis). The field on the border (entrance and exit) is extremely important, as we will find out, since it determines the focusing properties of the device itself: if missing, we would only have a rotation in the phase space of the particles. To describe the fringe fields, the best way is just to impose $\operatorname{div}\mathbf{B} = 0$ and exploiting cylindrical symmetry around z axis.

$$\mathbf{B} = B_r(r,z)\mathbf{e}_r + B_z(z)\mathbf{e}_z$$

If we impose a null divergence, we have

$$\operatorname{div}\mathbf{B} = \frac{1}{r}\frac{\partial}{\partial r}(rB_r) + \frac{1}{r}\frac{\partial B_\phi}{\partial\phi} + \frac{\partial B_z}{\partial z} = 0$$

Since B_r is limited, rB_r goes to zero for $r = 0$ and so we have

$$rB_r = -\int_0 rr' B_z(z)dr' \qquad\qquad B_r = -\frac{r}{2}B'_z(z)$$

The vector potential is given by

$$\mathbf{A} = \frac{r}{2} B_z \mathbf{e}_\phi$$

since, calculating its rotor, we have back the previous results:

$$\operatorname{rot} \mathbf{A} = \frac{1}{r} \begin{pmatrix} \mathbf{e}_r & r\mathbf{e}_\phi & \mathbf{e}_z \\ \partial_r & \partial_\phi & \partial z \\ 0 & rA_\phi & 0 \end{pmatrix} = -\frac{r}{2} B_z' \mathbf{e}_r + B_z \mathbf{e}_z = B_r \mathbf{e}_r + B_z \mathbf{e}_z$$

Calculating the Lorentz force we have

$$\begin{aligned} \mathbf{F} &= \frac{e}{c} \left(\dot{r}\mathbf{e}_r + r\dot{\phi}\mathbf{e}_\phi + \dot{z}\mathbf{e}_z \right) \times \left(B_r \mathbf{e}_r + B_z \mathbf{e}_z \right) = \\ &= \frac{e}{c} \left[r\dot{\phi} B_z \mathbf{e}_r + \left(\dot{z} B_r - \dot{r} B_z \right) \mathbf{e}_\phi - r\dot{\phi} B_r \mathbf{e}_z \right] \end{aligned}$$

The equation of motion then are:

$$\begin{cases} m\left(\ddot{r} - r\dot{\phi}^2 \right) = \dfrac{e}{c} r\dot{\phi} B_z \\ \dfrac{m}{r} \dfrac{d}{dt} \left(r^2 \dot{\phi} \right) = \left(\dot{z} B_r - \dot{r} B_z \right) \dfrac{e}{c} \\ m\ddot{z} = -r\dot{\phi} B_r \dfrac{e}{c} \end{cases}$$

If we transform these equations in Cartesian coordinates we have:

$$\begin{aligned} \mathbf{B} &= \mathbf{e}_r B_r + \mathbf{e}_z B_z = -\left(\frac{x}{r} \mathbf{e}_x + \frac{y}{r} \mathbf{e}_y \right) \frac{r}{2} B_z' + \mathbf{e}_z B_z = \\ &= -\frac{x}{2} B_z' \mathbf{e}_x - \frac{y}{2} B_z' \mathbf{e}_y + \mathbf{e}_z B_z \end{aligned}$$

and the Lorentz force in matrix form:

$$\mathbf{F} = \frac{e}{c} \begin{pmatrix} \mathbf{e}_x & \mathbf{e}_y & \mathbf{e}_z \\ \dot{x} & \dot{y} & \dot{z} \\ -xB_z'/2 & -yB_z'/2 & B_z \end{pmatrix} = \begin{cases} F_x = \dfrac{e}{c} \dot{y} B_z + \dfrac{e}{2c} y\dot{z} B_z' \\ F_y = -\dfrac{e}{c} \dot{x} B_z - \dfrac{e}{2c} x\dot{z} B_z' \\ F_z = \dfrac{e}{2c} B_z' \left(x\dot{y} - y\dot{x} \right) \end{cases}$$

To proceed further, it's useful to describe B_z as $B_z = B_0 f(z)$, where

$$f(z) = H(z) - H(z - L) \tag{3.12}$$

where, as previously defined, L is the solenoid length. With this definition, and defining ω_L as the Larmor frequency

$$\omega_L = \frac{eB_0}{2mc}$$

we have

$$\begin{cases} F_x = \omega_L 2m\dot{y} f(z) + \omega_L m y\dot{z} f'(z) \\ F_y = -\omega_L 2m\dot{x} f(z) - \omega_L m x\dot{z} f'(z) \\ F_z = \omega_L m x\dot{y} f_z' - \omega_L m y\dot{x} f'(z) \end{cases} \Longrightarrow \begin{cases} \ddot{x} = \omega_L \left(2\dot{y} f(z) + y\dot{z} f'(z) \right) \\ \ddot{y} = -\omega_L \left(2\dot{x} f(z) + x\dot{z} f'(z) \right) \\ \ddot{z} = \omega_L f'(z) \left(x\dot{y} - y\dot{x} \right) \end{cases} \tag{3.13}$$

A proper choice for $H(z)$ is

$$H(z) = \frac{1 + \tanh\left(\frac{x}{2\lambda}\right)}{2} = \frac{1}{1 + e^{-x/\lambda}} \tag{3.14}$$

so that the derivative is

$$H'(z) = \frac{1}{4\lambda} \frac{1}{\cosh^2\left(\frac{x}{2\lambda}\right)} = \frac{1}{\lambda} \frac{e^{-x/\lambda}}{\left(1 + e^{-x/\lambda}\right)^2} \tag{3.15}$$

If we restrict ourselves to the paraxial approximation, we can assume

$$\dot{z} \approx v_0 \tag{3.16}$$

The speed along z is constant and so $\ddot{z} = 0$.
We can also use the variable s to describe the longitudinal position:

$$s = \int_0^t v dt \approx v_0 t = z$$

so that

$$x' = \frac{dx}{ds} \approx \frac{dx}{d(v_0 t)} = \frac{dx}{dz} = \frac{dx}{v_0 dt} = \frac{\dot{x}}{v_0} = \frac{1}{\beta_0} \frac{\dot{x}}{c}$$

and the Larmor frequency

$$\Omega_L = \frac{eB_z}{2mc^2} \qquad \Omega_L' = \frac{d\Omega_L}{dz} = \frac{eB_z'}{2mc^2}$$

We should note that $B_z' = dB_z/ds \approx dB_z/dz$.
Under this paraxial approximation, we can rewrite 3.13 as

$$\begin{cases} x'' = 2\dfrac{\omega_L}{\beta_0} y' + \dfrac{\Omega_L'}{\beta_0} y \\ y'' = -2\dfrac{\omega_L}{\beta_0} x' - \dfrac{\Omega_L'}{\beta_0} x \end{cases} \tag{3.17}$$

where we have discarded z'' since it is now an extremely small correction thanks to 3.16.
We can also rewrite these equation in a complex form using $w = x - iy$:

$$w'' = 2\frac{\omega_L}{\beta_0} i w' + i\frac{\Omega_L'}{\beta_0} w \tag{3.18}$$

If we introduce the rotating reference system defined by

$$w = w_L e^{i\Phi} \tag{3.19}$$

where

$$\Phi(z) = \int_0^z \frac{\Omega_L(z')}{\beta_0} dz'$$

the first derivative is

$$w' = w_L' e^{i\Phi} + i\frac{\Omega_L}{\beta_0} w_L e^{i\Phi} \tag{3.20}$$

and the second one is

$$w'' = w_L'' e^{i\Phi} + 2i\frac{\Omega_L}{\beta_0} w_L' e^{i\Phi} + i\frac{\Omega_L'}{\beta_0} w_L e^{i\Phi} - \frac{\Omega_L^2}{\beta_0^2} w_L e^{i\Phi} \tag{3.21}$$

Inserting 3.19, 3.20 and 3.21 into 3.18 and dividing by $e^{i\Phi}$ the motion equation reads

$$w_L'' + 2i\frac{\Omega_L}{\beta_0}w_L' + i\frac{\Omega_L'}{\beta_0}w_L - \frac{\Omega_L^2}{\beta_0^2}w_L = 2i\frac{\Omega_L}{\beta_0}w_L' - 2\frac{\Omega_L^2}{\beta_0^2}w_L + i\frac{\Omega_L'}{\beta_0}w_L$$

simplified:

$$w_L'' + \frac{\Omega_L^2}{\beta_0^2}w_L = 0 \tag{3.22}$$

3.3.1 Maps in the thin lens approximation

We can consider the solenoid in the limit for $\lambda \to 0$, when the 3.15 goes to a $\delta(z)$. In this case, the focusing effect does not disappear, it becomes a kick.

Inside the solenoid we can write the map using the previously obtained motion equation:

$$w(s) = e^{i\Phi(s)}w_L(s) \tag{3.23}$$

where $w_L(s)$ satisfy the 3.22. In order to streamline the notation, we can define

$$k = \left(\frac{\Omega_L}{\beta_0}\right)^2 = \left(\frac{eB_0}{2mcv_0}\right)^2 \qquad \alpha \equiv \Phi(s) = \frac{\Omega_L}{\beta_0}s = \sqrt{k}s$$

The solution of 3.23 for $0 < s < L$ is

$$\begin{pmatrix} w_L(s) \\ w_L'(s) \end{pmatrix} = \mathsf{S}\begin{pmatrix} w_L(0) \\ w_L'(0) \end{pmatrix}$$

where

$$\mathsf{S} = \begin{pmatrix} \cos\alpha & k^{-1/2}\sin\alpha \\ -k^{1/2}\sin\alpha & \cos\alpha \end{pmatrix}$$

Going back from w to the real x, y coordinates we have

$$\begin{pmatrix} x_L(s) \\ x_L'(s) \\ y_L(s) \\ y_L'(s) \end{pmatrix} = \begin{pmatrix} \mathsf{S} & 0 \\ 0 & \mathsf{S} \end{pmatrix} = \begin{pmatrix} x_L(0) \\ x_L'(0) \\ y_L(0) \\ y_L'(0) \end{pmatrix}$$

It would be interesting also to go from the rotating system to the fixed one, using the 3.19. Noting that

$$w(s) = w_L(s)e^{i\alpha} \qquad w'(s) = w_L'(s)e^{i\Phi} + i\sqrt{k}w_L(s)e^{i\Phi}$$

and using the rotation matrix

$$\mathsf{R} = \begin{pmatrix} \cos\Phi(s) & \sin\Phi(s) \\ -\sin\Phi(s) & \cos\Phi(s) \end{pmatrix}$$

we can write

$$\begin{pmatrix} x(s) \\ y(s) \end{pmatrix} = \mathsf{R}\begin{pmatrix} x_L(s) \\ y_L(s) \end{pmatrix}$$
$$\begin{pmatrix} x'(s) \\ y'(s) \end{pmatrix} = \mathsf{R}\begin{pmatrix} x_L'(s) \\ y_L'(s) \end{pmatrix} + k^{1/2}\mathsf{R}\begin{pmatrix} y_L(s) \\ -x_L(s) \end{pmatrix}$$

We should notice that, for the first time, we are mixing x and y original components. Defining $Q = \cos\Phi(s)$ and $Z = \sin\Phi(s)$, the final form of the map can be written as

$$\begin{pmatrix} x(s) \\ x'(s) \\ y(s) \\ y'(s) \end{pmatrix} = \mathsf{R}_f \begin{pmatrix} x_L(s) \\ x'_L(s) \\ y_L(s) \\ y'_L(s) \end{pmatrix} = \mathsf{R}_f \cdot \mathsf{S}_f \begin{pmatrix} x(0) \\ x'(0) \\ y(0) \\ y'(0) \end{pmatrix}$$

with

$$\mathsf{R}_f = \begin{pmatrix} Q & 0 & Z & 0 \\ -k^{1/2}Z & Q & k^{1/2}Q & Z \\ -Z & 0 & Q & 0 \\ -k^{1/2}Q & -Z & -k^{1/2}Z & Q \end{pmatrix}$$

and

$$\mathsf{S}_f = \begin{pmatrix} Q & k^{1/2}Z & 0 & 0 \\ -k^{1/2}Z & Q & 0 & Z \\ 0 & 0 & Q & k^{-1/2}Z \\ 0 & 0 & -k^{1/2}Z & Q \end{pmatrix}$$

As we will see later from simulations, the solenoid is an exceptional tool to do energy selection, through focusing them at a certain position, where we can place an aperture to absorb all the non-focused protons. Unfortunately, beyond the desired energy, also particles with much lower energy are focused at the same point.

In the sharp edge approximation we can justify the presence of several peaks in the spectrum. For a given energy $E_* = 30$ MeV we consider the focus of the solenoid which is located at $z_{\text{foc}} = D + L + D_1$ where D_1 is such that, from equation 4.3, we obtain $A(E_*) = 0$:

$$z_{\text{foc}} = D + L + \frac{D\cos\alpha + k^{-1/2}\sin\alpha}{Dk^{1/2}\sin\alpha - \cos\alpha}$$

At $z = z_{\text{foc}}$ we place a collimator of radius r. A particle with energy $E \neq E_*$ and a given value of $\theta_0 = \left(x_0'^2 + x_0'^2\right)^{1/2}$ reaches the focal plane at a distance d from the z axis, where

$$d = \left(x^2(z_{\text{foc}}) + y^2(z_{\text{foc}})\right)^{1/2} = \theta_0 |A(E)|$$

and will go through the collimator only if $d < r$. As a consequence the condition that the particle passes through the collimator is $d < r$.

We first consider the position of the focus $z_{\text{foc}} = D + L + D_1$ as a function of E and look for values of E such that $z_{\text{foc}}(E) = z_{\text{foc}}(E_*)$. Indeed there are multiple values of the energy for which the same focus occurs. Choosing $D = 2$ cm, $B_0 = 10$ Tesla and $L = 27$ cm we find that at $E = 30$ MeV with $x'_0 = y'_0 = 0.05$, which corresponds to $p_z = 0.2523$, we have $D_1 = 58.2$ cm so that $z_{\text{foc}} = 87.2$ cm. These values are somewhat different from the case with a smooth fringe field. Changing x'_0, y'_0 we change p_z and the focus slightly changes. For instance with $x'_0 = y'_0 = 0.01$ we have $p_z = 0.2528$ and $z_{\text{foc}} = 88.4$ cm. In figure 3.5 we show the position of the focus as a function of energy E by keeping $x'_0 = y'_0 = 0.01$. The same focus $z = 88.4$ cm occurring for $E = 30$ MeV is also obtained for $E = 4.3$ MeV and $E = 1.6$ MeV. The same figure shows the distance d from the z axis at $z = 88.4$ cm when the energy is varied and compares it with the collimator radius $r = 0.5$ mm.

We consider now a beam having an exponential spectrum and a uniform angle distribution within a given range.

$$\frac{dN}{dEd\theta_0} = N_0\rho(E, \theta_0)$$

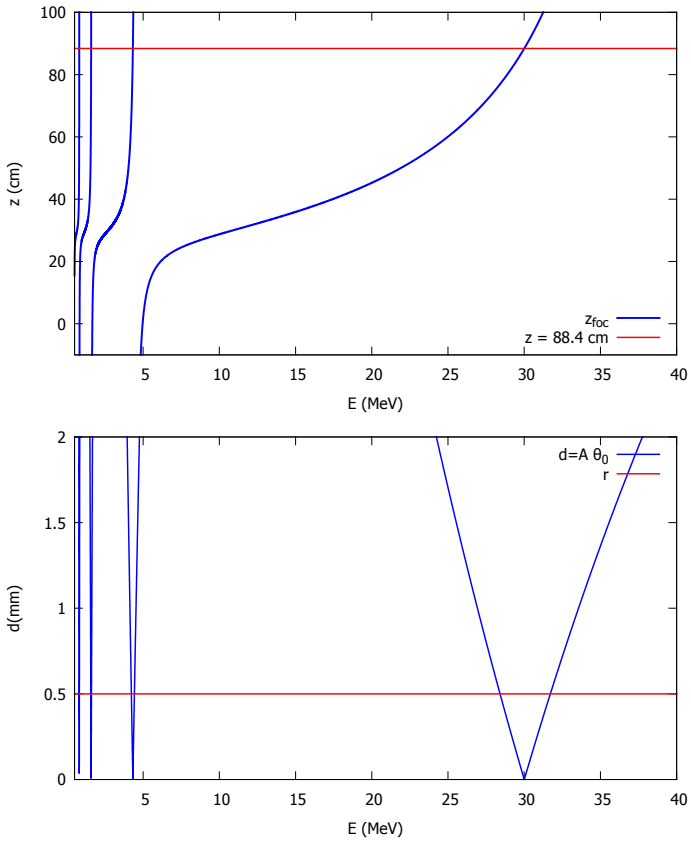

Figure 3.5: Upper frame: plot of the focus as a function of the energy compared with the focus for $E = 30$ MeV. Lower frame: comparison of the distance $d = A\theta_0$ from the z axis at the point $z = 88.4$ with the collimator radius $r = 0.5$ mm when the energy varies and $x'_0 = y'_0 = 0.01$

$$\int_{E_{\min}}^{E_{\max}} dE \int_{\theta_{\min}}^{\theta_{\max}} d\theta_0 \; \rho(E, \theta_0) = 1$$

where N_0 is the total number of particles having crossed the first collimator. We assume for simplicity a factorization of the distribution according to $\rho(E, \theta_0) = \rho_E(E)\, \rho_\theta(\theta_0)$ where

$$\rho_E(E) = \frac{1}{E_0} \frac{\exp\left(-E/E_0\right)}{e^{-E_{\min}/E_0} - e^{-E_{\max}/E_0}} \chi_{[E_{\min}, E_{\max}]}(E)$$

and

$$\rho_\theta(\theta_0) = \frac{1}{\theta_{\max} - \theta_{\min}} \chi_{[\theta_{\min}, \theta_{\max}]}(\theta_0)$$

having defined $\chi_{[a,b]}(x)$ the characteristic function of the interval $[a, b]$. If $E_{\min} \ll E_0$ and $E_{\max} \gg E_0$ then $e^{-E_{\min}/E_0} - e^{-E_{\max}/E_0} \simeq 1$. The spectrum at the exit of the second collimator at $z_{\text{foc}} = L + D + D_1$ is given by

$$\rho_1(E) = \int_{\theta_{\min}}^{\theta_{\max}} d\theta_0 \, \vartheta(r - A\theta_0) \rho_E(E) = \; g(E) \rho_E(E)$$

The function $g(E)$ gives the fraction of particles transmitted at a given energy through the collimator. We recall that A depends weakly on θ_0 because $p_z = p_0(1 + \theta_0^2)^{-1/2}$ and for non relativistic particles $\beta_z \simeq p_z$ we have $k^{1/2} = \Omega_L/\beta_z \simeq \left(1 + \theta_0^2\right)^{1/2} \Omega_L/p_0$ and $\theta_0 \ll 1$. When r decreases, the width of the peaks decreases too and a spectrum of lines is approached. When the value of $\theta_{\min}$ decreases the peaks become larger and a background is

progressively created because the particles almost parallel to the z axis cross the collimators whatever is their energy. In figure 3.6 we show the function $g(E)$ for two different values of $\theta_{\min}$ equal to 0.001 and 0.005 respectively

During my PhD I was the tutor of S. Fazzini that wrote his bachelor thesis on this topic.

3.4 Other devices

3.4.1 RF cavity

For the purpose of improving the characteristics of laser-produced protons that have thermal characteristics and a Maxwellian distribution, rotation of the particles in the longitudinal phase-space ("phase rotation") has been proposed [86, 87, 88, 89].

The principle of its design is almost easy: if we let the laser-driven bunch propagate for some centimeters, the length of it will become longer than the wavelength of the RF cavity. It's then possible to inject the bunch and, thanks to a good calibration of the device and the different phases of the RF electric field the protons will experience, the relatively higher energy ions will be decelerated and lower energy ones will be accelerated, collecting at the end just a well-defined energy region.

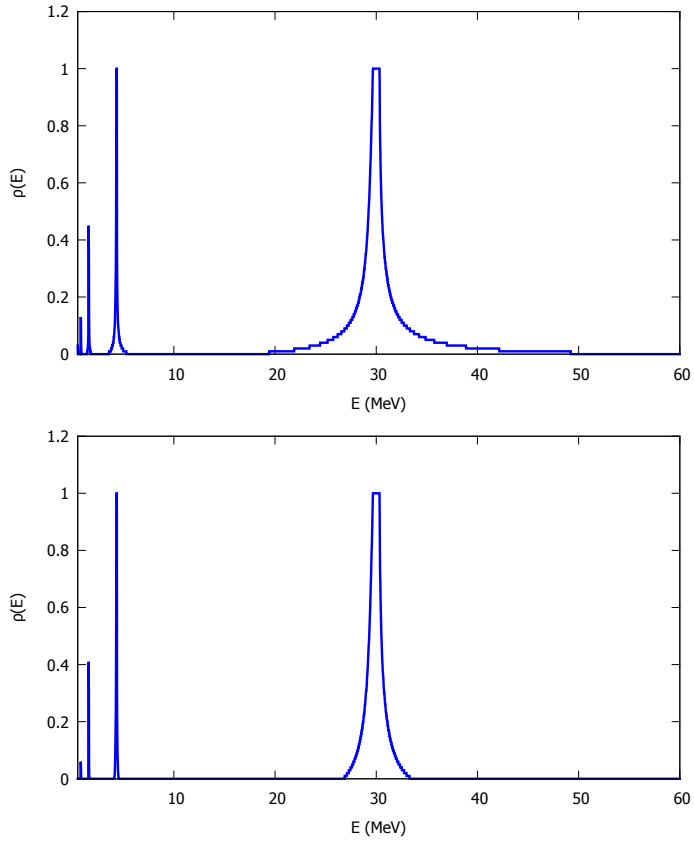

Figure 3.6: Upper frame: Plot of the function $g(E) = \rho_1(E)/\rho_E(E)$ which gives the fraction of particles having overcome the second collimator, at a given energy, whatever is their initial value of angular deviation θ_0. The spectrum is obtained for an angular distribution whose lower bound is $\theta_{\min} = 0.001$. Lower frame: the same as the upper frame with a larger value of the angular spectrum lower bound $\theta_{\min} = 0.005$. In this case the spectrum is narrower.

This idea was also used in our works and combined with a post acceleration stage: the RF cavity was acting as a "perfect" filter and also as a device that raised the energy, in our cases from $\sim$ 30 to $\sim$ 60 MeV [85].

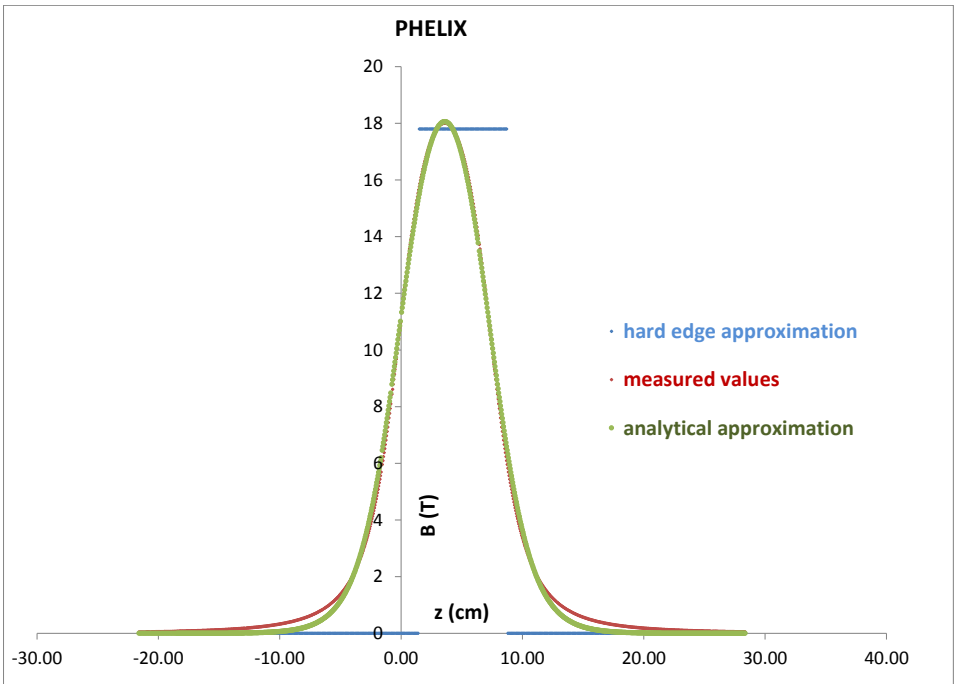

Figure 3.7: On-axis field for PHELIX Solenoid (GSI-Darmstadt), measured and both in the hard-edge approximation and in the analytical fringe-field representation.

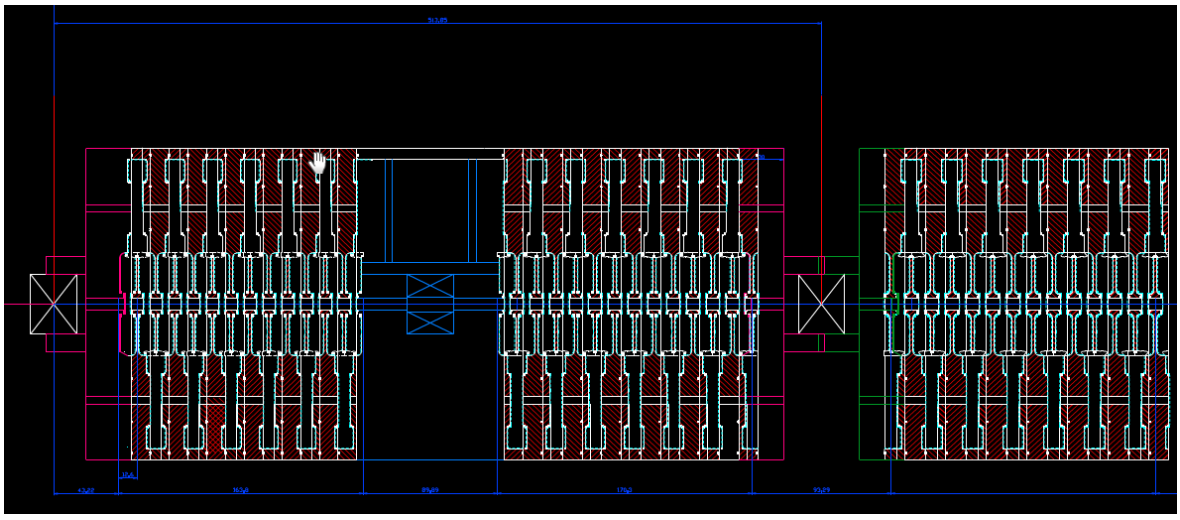

Figure 3.8: CAD drawing of ACLIP, an RF cavity designed by INFN and used for our studies in paper [85].

3.4.2 Plasma lens

It has been proposed [90] to use lasers also to create their own devices for beam focusing and energy selection. The advantages would be connected to their ability to withstand large ion beam currents, the fact that they can be switched over picosecond time scales and their property to support large deflecting fields on microscales. As described by the authors, the proposed method uses a compact laser-driven micro-lens arrangement. The process begins with relativistic electrons injected through the cylinder's wall, produced by the laser, which spread evenly inside and initiate the hot-plasma expansion. The transient electric fields associated with the expansion are used in a radial geometry to focus protons obtained by the main laser pulse impact on the thin planar foil.

This method is extremely interesting but was not considered by us, at least in these initial stages, because we were looking for a design that was able to sustain a high-frequency operation mode.

3.5 Propaga

At the beginning of my PhD I continued the development of a particle tracking code that I started to write during my Master Thesis.

The main goal of this software is to be able to transport all the particles that come out from our particle-in-cell code and any other code, through extremely flexible interfaces, inside elements of a conventional beamline. The code is available under request on GitHub[1].

Algorithms

A conventional transport code is not "enough" for laser-plasma driven transport simulations, since almost all of traditional codes have important drawbacks that make it difficult to use them with laser-driven bunches. The main trouble is the exponential spectrum of the particles, an assumption valid for all the species. This peculiarity renders unusable all the tools that use an optical formalism to do the transport, like PARMILA [91] or TRANSPORT [92], since their fundamental requirement is a strictly monochromatic beam, and also many other tools that relies on the integration of the motion equation that simplify the tracking using just a single virtual particle located at the center of the bunch. Since the bunch becomes very long just after few centimeters, and because particles with different energies have different behaviors, using these tools can be very troublesome: our solution, when we had to handle this problem, was to split the full bunch in thousands of "almost monochromatic" sub-components and so the full simulation was split inside thousands of sub-simulations.

The code is fully parallelized with MPI and OpenMP, in order to be able to scale as much as possible. It includes all the basic elements of a conventional beamline with the algorithms for a time integration of the particle tracks. At each time step, for each particle it overlaps the contribution at its position of every field in the structure, so that even very long fringe fields can be considered in case of complex overlapping. Then it applies the geometry, and flags the particle if it doesn't fit inside the constraints.

The code contains a proper description of quadrupoles, solenoids, chicanes, RF cavities, drift tubes and apertures. It has been thoughtfully checked with other codes, such as ASTRA from Desy [93, 94]. All of the tests were done in the proper approximations valid for those other codes and the results are perfectly matched.

[1] https://github.com/cenit/Propaga.git

There's also an experimental routine to calculate the space-charge effect as an electrostatic one. We don't use it in our daily simulations, since in laser-plasma literature the space-charge effect is almost always considered as negligible, at least after a couple of centimeters from the source, since the charge is diluted enough. Also, the routine does the calculations as an N-body algorithm and so it's extremely hard to make it scale to many particle system as the ones we are dealing with. This is a loss only for a special kind of problems that we are still not dealing with and that is not very well treated also in literature, that is the interaction of the protons with the comoving electrons. Fast electrons produced during the laser-plasma interaction, in fact, go away pretty soon, and so they can be removed with a chicane. But what happens with electrons contained inside the proton/ion bunch is much more difficult to understand, since the self-interaction can be very strong and so it could be very troublesome to separate them.

In Appendix B I will discuss a way to do bunch de-neutralization as studied at GSI (Darmstadt), using a foil, that can be made of copper or carbon, to absorb electrons and reduce as much as possible the number of secondary emitted ones.

Visualization

Plotting of bunch parameters and statistical values along the lattice is done through a `gnuplot` interface. Most important plots that we have for a simulation are the emittances and the bunch envelope along the beamline, and the spectra at different positions (integrated in time) or time steps (integrated along the whole line). The code is extremely modular, so it is possible to do many other evaluations easily if requested by the user. Data converters and post-processing tools are available on other GitHub repositories[2,3,4].

[2] `https://github.com/cenit/dataproc.git`

[3] `https://github.com/cenit/converter.git`

[4] `https://github.com/cenit/ALaDyn_Fluka_Astra_tools.git`

4 Increasing the proton bunch quality

Since laser-plasma acceleration of protons has been demonstrated as a proof-of-concept technology that works, many laboratories now are trying to improve the quality of the proton bunch obtained.

This is an extremely important work, since almost all of the applications, like fast ignition, laboratory astrophysics, material studies, biological irradiation, cancer therapy, require a stable and reproducible beam, with well-defined properties.

In this chapter, I will analyze the work that we have done in order to improve the quality of laser-driven protons. Starting from the foundation of beam shaping discussed in chapter 3 and describing some new ideas, I will present the most up-to-date results that we had from simulations and that we presented in our papers.

Improving the beam quality can be seen as a broad topic. In fact it could mean improving the maximum energy, the average energy, the charge of the bunch, its divergence and size, the emittance in general, reducing the broadness of the energy spectrum to increase monochromaticity, ... First of all I will describe few ways to increase the cut-off energy and then I will present some beamline designs that perform energy selection and bunch size confinement.

4.1 Target optimization and development

In these years of laser-plasma ion acceleration research, most of the focus has been devoted to improve the quality of the lasers. Enhancing the pulse energy, improving the contrast, reaching new level of intensity on the focal spot, a great work has been pursued on delivering more energy in a shorter pulse on the target. This was important in order to be able to shoot on very thin target and transfer as much energy as possible to ions, without "burning" energy ablating a thick target.

On the other hand, not so much work has been done to this very important ingredient of the experiment. In a typical configuration, the target is a simple metallic foil, without much characterization. Few alternative target designs exist, like plastic foils, micro-grooved targets, double layer (foam-coated), ultrathin, mass-limited, conical-shaped, but the impression that we have is that this is an area that can benefit a lot from future work.

An alternative to solid target could be shooting on clustered gas jets [95], but the results were not extremely enthusiastic and so this path looks like difficult to pursue; fortunately, an effort is going on also in other labs like LOA.

4.1.1 Foam

An interesting role in enhancing laser pulse conversion into fast electrons, and so faster ions, was found with the foam-coating of metallic targets [96]. In fact, since the plasma obtained from a bare metal foil is highly overcritical ($n_e > 100 n_c$), for a laser with optical/near-infrared wavelength, the penetration depth is just a "skin" layer, of thickness $\sim c/\omega_p = (\lambda/2\pi)\sqrt{n_c/n_e}$. This means that the interaction of the laser with the target is a surface one, rather than a volume one. Most of the laser is usually reflected, even if a good part of it can be absorbed via different mechanisms [97].

In order to enhance the laser absorption, a low-density coat on the upstream (illuminated) side of the target was deeply studied in our group [63]. The presence of this near-critical-density layer allows the laser to penetrate inside the target, enhancing energy conversion into fast electrons through an higher absorption.

This technology is extremely promising, even if it adds some complications to the design of an experiment. In fact it may be extremely difficult to deposit such a layer on a very thin target, in an accurate and non-destructive way.

In our simulations, we considered many different electron densities n_f and thicknesses ℓ_f for the foam: $1 \leq n_f \leq 4n_c$ and $1 \leq \ell_f \leq 8\mu$m. Behind the target, on the downstream side, there's a contaminants layer, whose characteristics are not very important for the results of the simulations. Usually it is kept to a very low thickness ($\ell_c \leq 10$ nm) and densities at about ten times the critical density.

In figure 4.1 we can see the drastic improvement that a foam coating can bring to the energy spectra, without having to modify anything on the laser side.

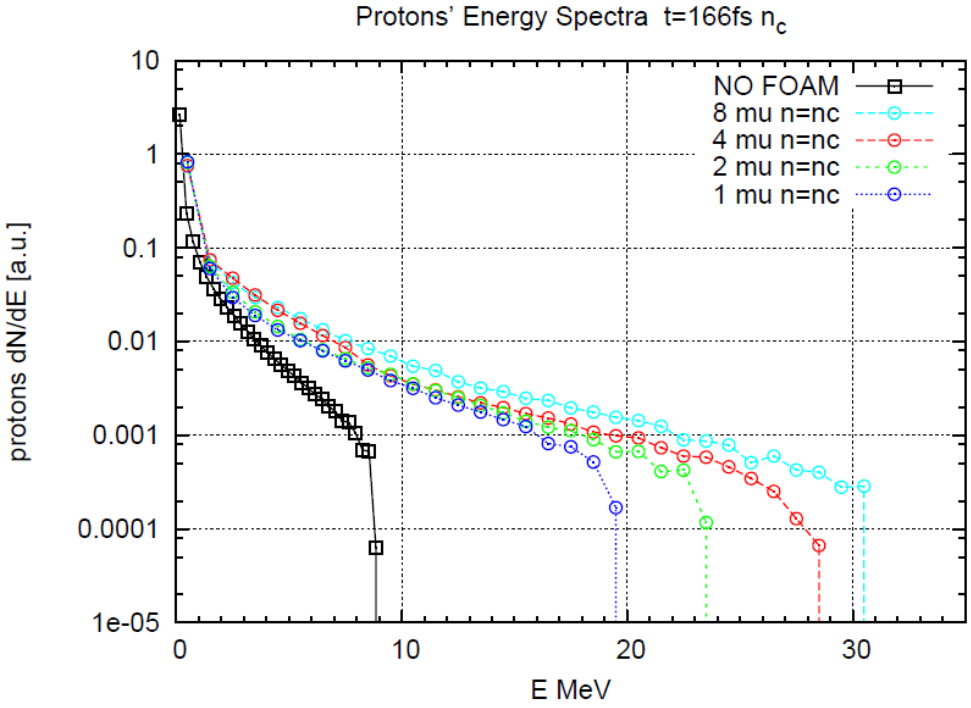

Figure 4.1: From [63], a comparison of the energy spectra obtained with the same target and the same laser, just coating with different foam thicknesses.

4.1.2 Prepulse shaping and preplasma

Pre-heating the target with a second pulse or exploiting the prepulse is an extremely interesting and difficult topic. The major constituent of the prepulse is the nanosecond-scale amplified spontaneous emission (ASE). This energy, delivered on target with low intensity (with respect to the main pulse, not really on an absolute point of view) and long time scales (nanoseconds instead of femtoseconds) heats, melts, evaporates, ionize and ablate a portion of the initially solid "conventional" bare target. This ablated material creates a preplasma that can be studied, and, contrary to an intuitive expectation, that such preplasma hinders the ion acceleration due to the main pulse depletion, what can be found is that, under certain optimal conditions, the acceleration can be substantially enhanced as compared to the (purely numerical, still not feasible) clean laser-pulse case. This may be due to the relativistic self-focusing of the main pulse, or also to the enhanced laser conversion in the low-density region into fast electrons.

Citing the conclusions found in [98], having a petawatt class laser with a clean pulse is of course extremely beneficial even with those results, since in this case a second lower intensity laser pulse can be used to create the optimum preplasma, instead of having to rely on an unstable (shot by shot) phenomenon.

Anyway, we can say that the plasma slab formed by the pre-pulse plays an important role, but understanding this mechanism is not so straightforward. In [98] and [99], to describe the melting, evaporation and ablation they use a hydrodynamic code. Both article, especially the second, describe in good detail the governing equations implemented in the code and the algorithms used in the simulations. The output of this hydrodynamic code is then used as an input for the PIC code to describe the interaction of the main pulse with the "residual" target. All their work has been done in 2D and it is one of my personal goal for the next future to do some 3D simulations on this topic.

Since I don't have any hydrodynamical code, to tackle this problem I started using bops[1] [100, 101]. This is an extremely nice PIC code, 1D-3V (1 spatial, 3 velocity coordinates), originally created by Paul Gibbon. Of course the oversimplifications of a 1D code are big, but what I was looking for were just some density profile along the laser propagation direction for the targets hit by the ASE prepulse (modeled as a continuous sinusoidal wave with low intensity). Unfortunately the code is not parallelized and this made the task unfeasible. Anyway, what we learnt from this experience was invaluable and we are planning for 2D simulations of these extremely long interactions using our `ALaDyn` code in 2D mode. We didn't use it from the beginning since it is still not working in 1D.

In order to have density profile for the targets as an input for `ALaDyn` 2D/3D, reading from literature [102] I got some realistic models obtained with other hydrodynamic codes like MULTI [103]. The typical given description of a target after the prepulse is essentially a thinner target, whose ablated material created a low density cloud in front of it, that is describable with an exponential ramp and a long, uniform, low density layer at the beginning.

Examples of average energy evolutions in time for different preplasma are shown in figure 4.2.

[1] `https://github.com/cenit/bops.git`

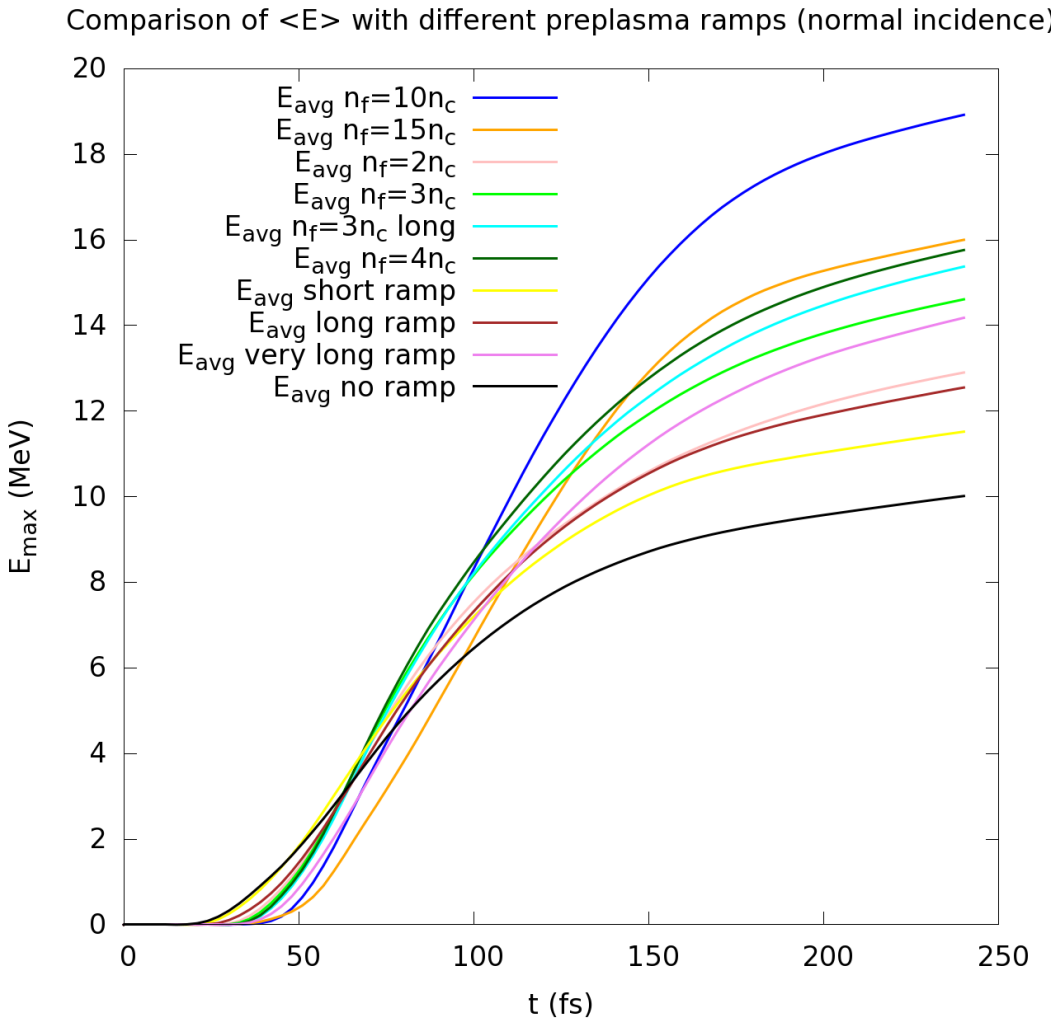

Figure 4.2: Comparison of average energies obtained from different target preplasmas. All the shots were done using the same laser pulse. We can notice that the case without preplasma is the one reaching the lowest average energy at the end (all the preplasma configurations considered were enhancing ones). Also to note that the one without preplasma is the one starting first, since the laser does not have to penetrate any layer at the beginning.

4.2 Beamline development

4.2.1 Beamline with solenoid and LINAC

Using the solenoid as a bunch compressor and an energy selection device, we studied many simulations in order to obtain few realistic configurations.

In every condition, we had to choose the best energy slice, that was the highest energy with at least 10^8 protons. Following there is an example.

During my PhD I was the tutor of C. Benassi that wrote his bachelor thesis on this topic.

This work was very instructive for the paper [85], where we analyzed conventional post-acceleration of laser-driven proton bunches.

In that work, trying to have a configuration as close as possible to the experimental condition of LILIA Phase II, we chose as a target a composite model given by a thin foil

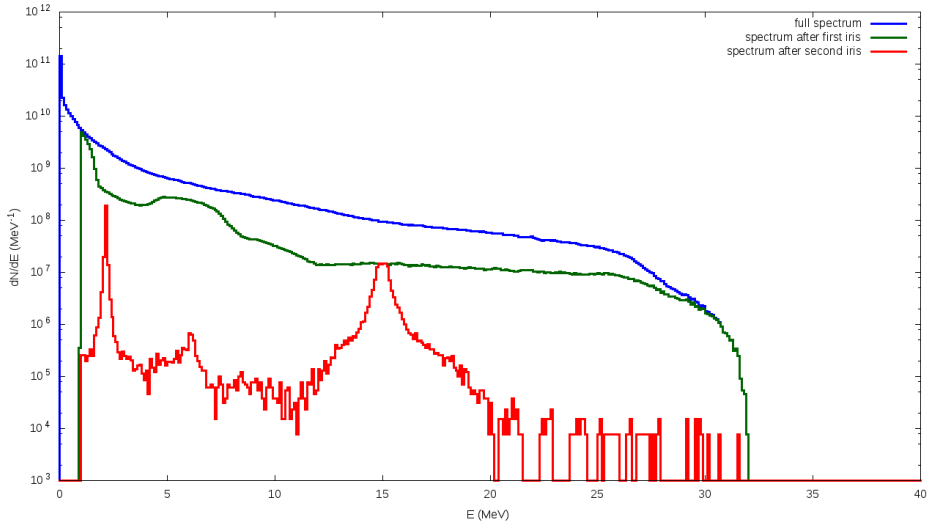

Figure 4.3: PIC Simulation: $a_0 = 20$, $n/n_c = 40$, $\ell = 0.2$ μm, $\ell_c = 0.05$ μm, $\ell_f = 0.0$ μm. Transport Simulation: first collimator at $z = 1$ cm, cutting at 50 mrad, solenoid from $z = 2$ cm to $z = 32$ cm with a field of 7 T and a fringe field λ factor of 2 and the energy selector (second collimator) at $z = 86$ cm.

with a layer of foam for the TNSA mechanism and a target with critical density for the MVA regime.

The injection into a linac for post-acceleration could be done directly without any beamline at the beginning, but this strategy has at least a couple of drawbacks:

- we are not compressing beam divergence and so only the protons coming out from the target with very low angles are accepted inside the cavity;
- since we are giving the task to do energy selection fully to the RF cavity, we are loosing a lot of particles inside the first module. This may not be a problem at the beginning, but with the strategy in mind to design a high-repetition device, this would compromise the functionality and the maintenance of it, since we would have the activation of the material. Clearing the bunch, as much as possible, before the entrance is extremely useful.

So, since at INFN there's ACLIP (ACceleratore LIneare compatto per Prototerapia) [104, 105] ready, which has an injection energy of 30 MeV, we chose target designs in order to end up with a maximum proton energy of at least 60 MeV using a laser configuration similar to FLAME for LILIA Phase II.

It was important to have a good number of protons at 30 MeV and the transport line is designed in order to reduce as much as possible the losses for that slice.

Similar experiments and simulations, done independently but at the same time, have been done at GSI and are reported in few papers [106, 107].

The first transport line that we considered for these studies was based on a solenoid, because it appeared to be more efficient than a multiplet of quadrupoles. To reduce the angular spread of the initial beam to 50 mrad we start with a collimator, which does not cause a relevant reduction of the intensity. To select the energy we place a second collimator after the solenoid, precisely on the focus of the protons having the energy 30 MeV of the selected slice. We observe that the same focus occurs for lower energy protons, but the

energy separation is so large that the low energy peaks can be easily removed. Again, the use of a collimator to perform energy selection has been independently proposed in [108].

After the transport and energy selection the beam has a small size and transverse emittance so that it is possible to inject it into the RF cavity. But let's see the configuration in more detail: we analyzed the behaviors of two different bunches inside the same beamline, one obtained on a solid target, the other on a quasi critical density target.

For the TNSA regime we consider a linearly polarized laser pulse of duration $\tau = 25$ fs FWHM (Full Width Half Maximum), wavelength $\lambda = 0.8\,\mu$m and power $P = 270$ TW. With a waist $w = 3\,\mu$m the intensity is $I = 2\,10^{21}$ W/cm^2 which corresponds to $a = 30$.

The target we consider is a composite one: on the illuminated side is deposited a layer of foam having quasi critical density and thickness of 2 μm, while on the rear of the Al foil (electron density $n_e = 40 n_c$ and thickness $\ell = 0.5\mu$m) we put a layer of contaminants (hydrogen) of thickness 0.05 μm and density $n_e = 9\,n_c$.

The ionization state of the Al foil is limited to the ninth electron. A non-full ionization state of the foil is justified since the absorption of laser energy occurs mainly in the foam layer. The foam layer is H fully ionized.

In the upper frame of figure 4.4 we show the protons energy spectrum for the composite target, where the maximum energy is 60 MeV and the average energy is 7.2 MeV; we also compare the full spectrum with the energy spectrum obtained with a cutoff in the angle θ at 50 mrad. In the lower frame we show the energy-angle distribution $dN/(dEd\theta)$ where $\theta = \arctan(p_\perp/p_z)$ having denoted by $p_\perp = (p_x^2 + p_y^2)^{1/2}$ the transverse component and by p_z the longitudinal component of the momentum of each proton.

The longitudinal resolution for overcritical targets has been chosen in order to resolve the skin depth in the foil, which in our case is $\ell_{\rm skin} = \lambda/(2\pi(n_e/n_c - 1)^{1/2}) \simeq 20$ nm. The computational box is $L_z = 22\,\mu$m, and $L_x = L_y = 32\,\mu$m transversally. The grid size is $\Delta z = 10$ nm, $\Delta x = \Delta y = 30$ nm so that the number of cells is $2.5\,10^9$ whereas the total number of macroparticles describing the electrons is $2\,10^9$ and the number of ions is correspondingly chosen on the base of the ionization state. Transversally the laser pulse and electron density variations are milder so that we can allow a space resolution larger than the skin depth.

For the quasi-critical targets, where the MVA regime dominates, the key laser parameter is power rather than intensity [77]. We have considered a circularly polarized laser pulse with $P = 155$ TW of duration 25 fs FWHM. The waist is 2.5 μm so that the intensity is $I = 1.58\,10^{21}$ W/cm^2 which corresponds to $a = 19$. The target thickness is 40 μm and its electron density is $n = n_c$. In this case PIC simulations provide a maximum energy $E_{\rm max} \sim 100$ MeV.

The full energy spectrum and the spectrum with a cutoff in the angle at 50 mrad are shown in the upper frame of figure 4.5. The distribution in the energy-angle plane is presented in the lower frame of the same figure: it shows that the angular spread is higher than in the overcritical case. For this configuration the computational box is $L_z = 40\,\mu$m and $L_x = L_y = 20\,\mu$m with a grid size $\Delta_z = 25$ nm and $\Delta_x = \Delta_y = 50$ nm. The total number of cells is $2.5\,10^8$ and the average number of macroparticles per cell is 8 so that the total number is $2\,10^9$ (the initial distribution is uniform).

Let's analyze now the bunch propagation along the beamline. First of all, let's say that when dealing with a laser-driven bunch the description itself can be cumbersome since all the conventional statistical parameters are always known for monochromatic bunches.

When the full beam is considered, a given point z is reached at different times by particles having different energies. In our case, we adopt a strategy based on the computation of the RMS invariants in order to characterize its properties. At any time we

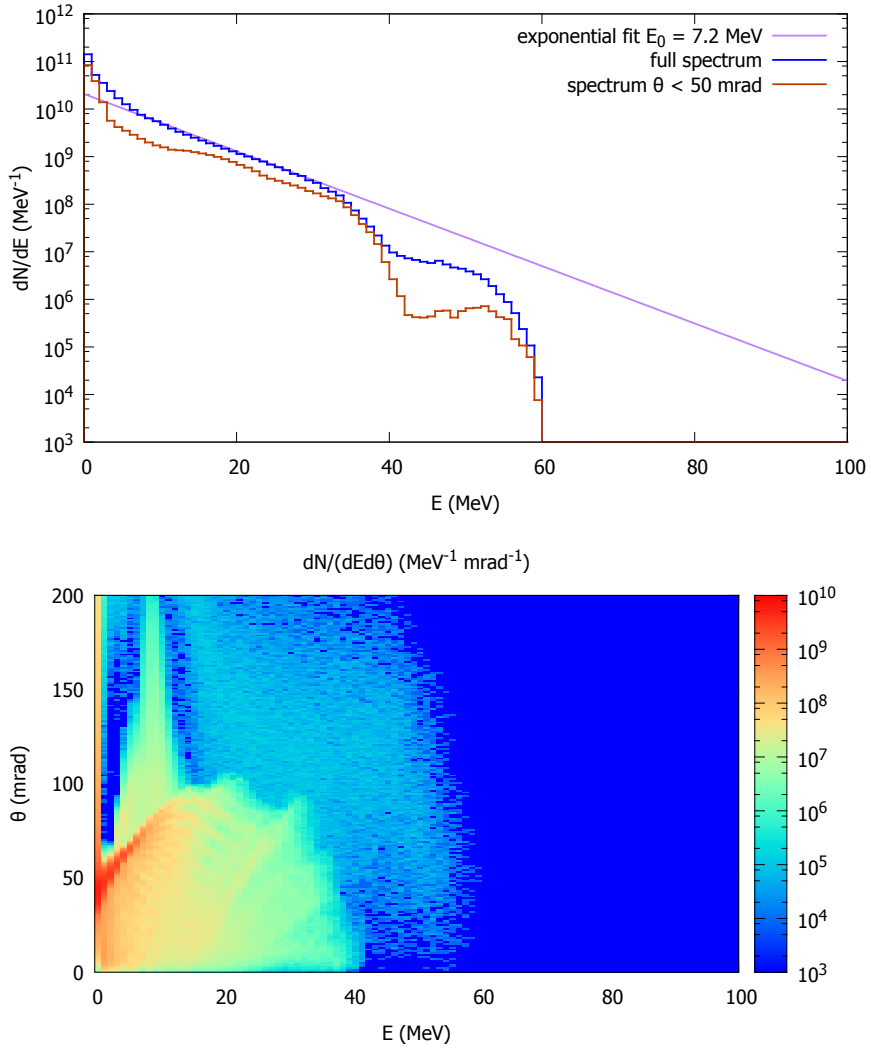

Figure 4.4: Upper frame: plot in a logarithmic scale of the proton initial energy spectrum (blue line) and after an angular selection $\theta < 50$ mrad (light brown line) for the composite foam+foil target (TNSA) with $a = 30$. Lower frame: initial energy-angle distribution of the bunch in a logarithmic color scale.

compute the averages $\langle x_i \rangle$, variances σ_i^2 of the space variables and the emittances ϵ_i. Letting $x_1 = x,\ x_2 = y,\ x_3 = z$ they are defined by

$$\sigma_i^2 = \langle (x_i - \langle x_i \rangle)^2 \rangle \tag{4.1}$$

$$\epsilon_i^2 = \langle (x_i - \langle x_i \rangle)^2 \rangle \langle (x_i' - \langle x_i' \rangle)^2 \rangle + - \left(\langle (x_i - \langle x_i \rangle)(x_i' - \langle x_i' \rangle) \rangle \right)^2 \tag{4.2}$$

These averages are computed at each time step but to display them we use $\langle z \rangle$ rather than t itself. Indeed the longitudinal position of the center of mass of the beam $\langle z \rangle$ provides a more intuitive picture of the propagation of the beam. When its longitudinal size, measured by σ_z, becomes large the interpretation of the dependence of the position variances and emittances on $\langle z \rangle$ is no longer intuitive as for a short bunch.

The spectrum may be filtered to reduce its support to a smaller interval, by using a suitable focusing and collimation system. Supposing that $\langle z \rangle$ is 1 m and that $\delta_1 = 10\%$

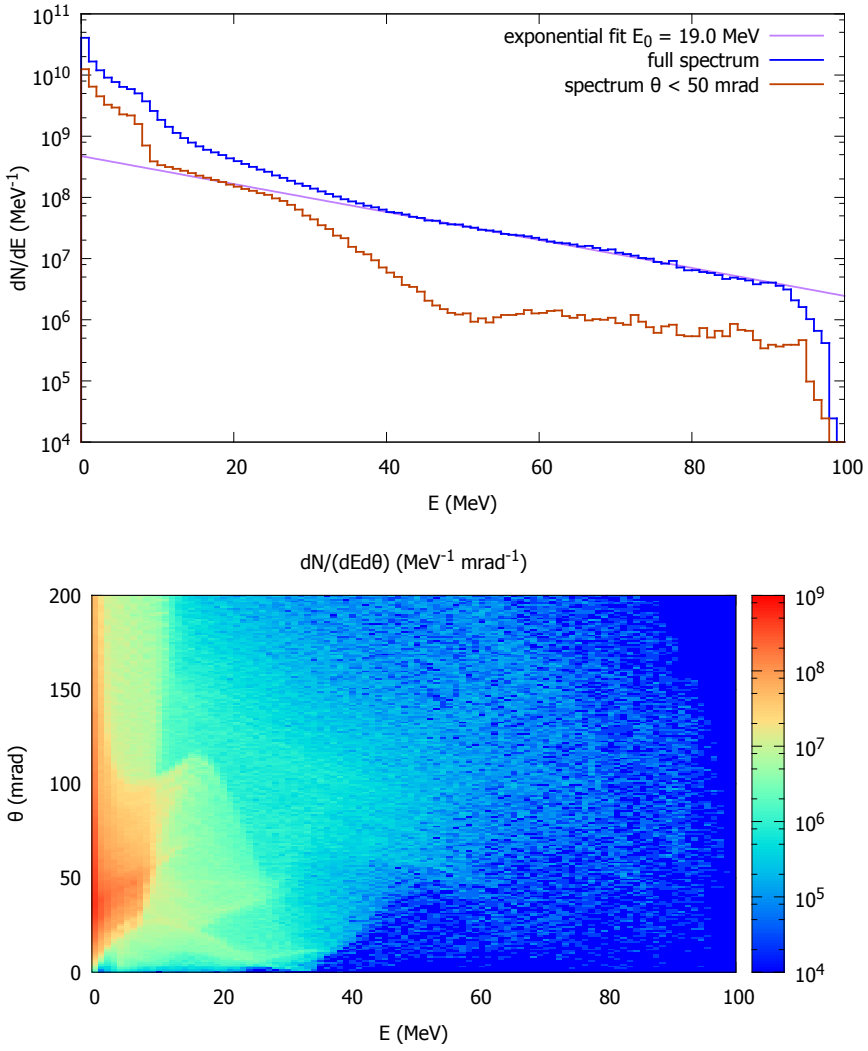

Figure 4.5: Upper frame: plot in a logarithmic scale of the proton initial energy spectrum (blue line) and after an angular selection $\theta < 50$ mrad (light brown line) for the target with critical density (MVA) with $P = 155$ TW and $a = 19$. Lower frame: initial energy-angle distribution of the bunch in a logarithmic color scale.

then σ_z is close to 3 cm. If $\delta_1 = 1\%$ then $\sigma_z = 3$ mm and the whole bunch is suitable for injection into a high frequency RF cavity. In such cases the use of $\langle z \rangle$ as independent variable is very appropriate.

The early propagation of the beam, from $t = 0$ up to $t \sim 0.15$ ps, where the acceleration process terminates, is described by the PIC simulation. The subsequent propagation up to a few ps is mainly ballistic, but the interaction of electrons and protons still plays a role at least for charge neutralization. The propagation of the beam is treated by neglecting the electrons, part of which is still comoving with the protons. The separation of protons becomes large due to free motion and the dilution of the proton bunch allows, at first approximation, to neglect space charge effects. It would be desirable to model these effects but the available simulation schemes are still inadequate to fully address this issue.

In appendix B I will show some strategies to remove the comoving electrons and ease this constraint.

The transport line we considered is made of a drift of length D and a circular collimator of radius r, followed by a solenoid of length L.

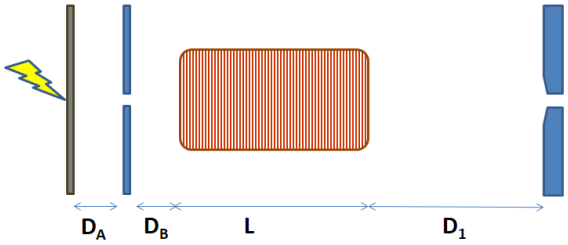

Figure 4.6: Schematic drawing of the transport line. D_A = D_B = 10 mm, D_1 = 510 mm, L = 300 mm, first iris radius = 0.5 mm, second iris radius = 0.5 mm, second iris minimum thickness = 5 mm.

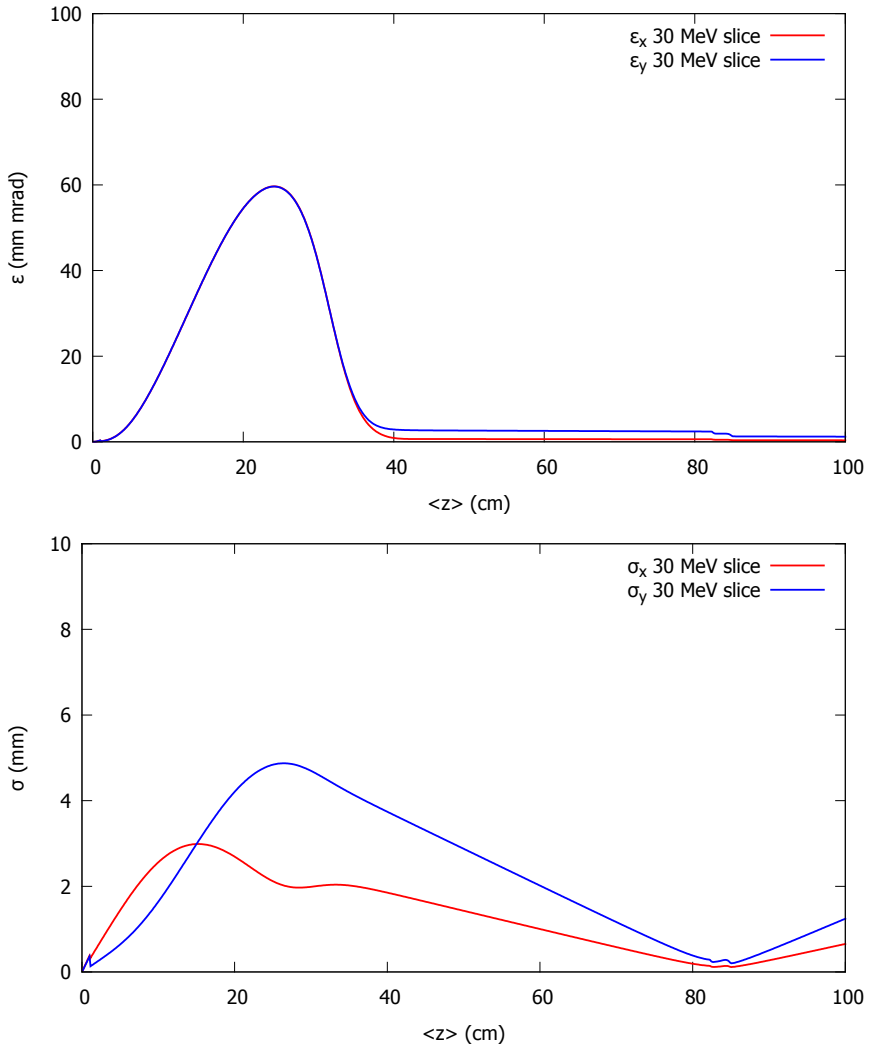

Figure 4.7: Upper frame: plot of the transverse emittances ϵ_x, ϵ_y in mm-mrad as a function of $\langle z \rangle$ in cm for an energy selection of the beam $29 < E < 31$ MeV. Lower frame: plot of the RMS beam sizes σ_x, σ_y in mm for the same energy selection. The focus of the solenoid for this quasi mono-energetic beam is at $z = 83$ cm

As described in chapter 3, the analytic treatment of the solenoid is elementary only in the sharp edge limit. In this case, we have a focusing in both phase planes (x, x') and (y, y') followed by a rotation in the (x, y) and (x', y') planes. Letting $\beta_z = v_z/c \simeq p_z/mc$

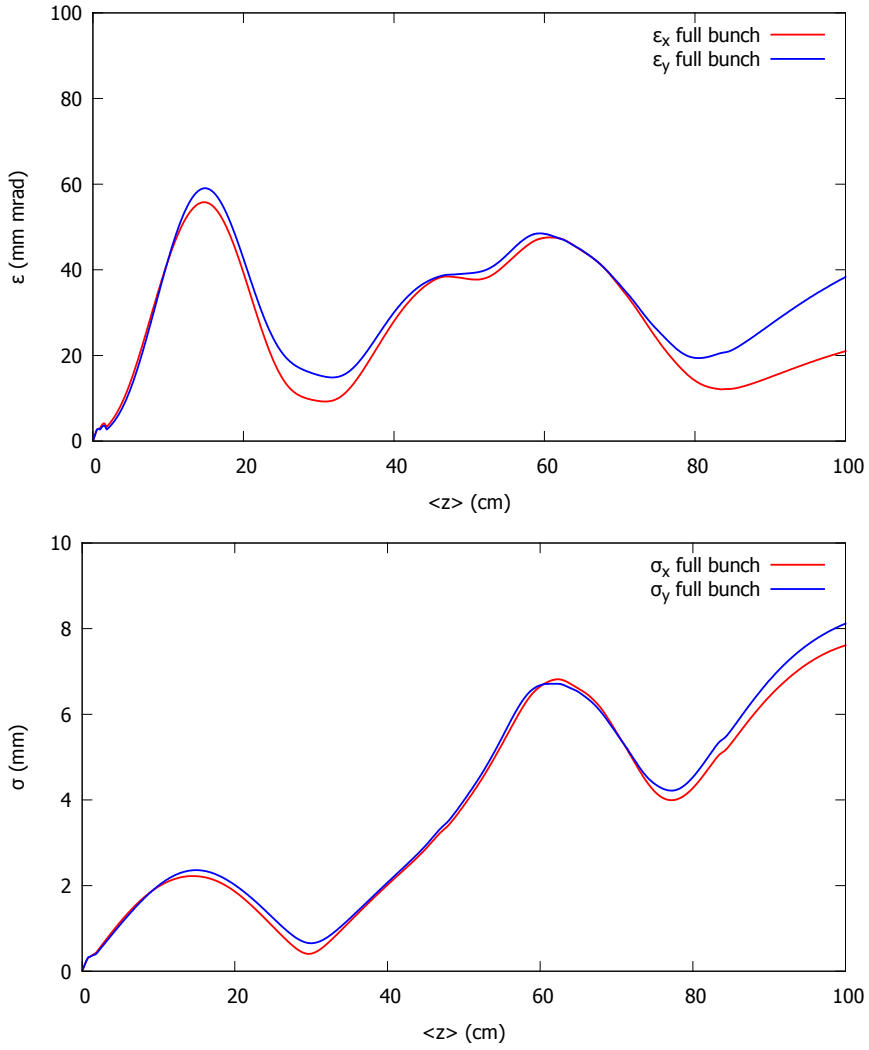

Figure 4.8: Upper frame: plot of the transverse emittances ϵ_x, ϵ_y in mm-mrad as a function of $\langle z \rangle$ in cm for an energy selection of the beam $3 < E < 60$ MeV. Lower frame: plot of the RMS beam sizes σ_x, σ_y in mm for the same energy selection.

we define

$$\sqrt{k} = \frac{\Omega_L}{\beta_z} = \frac{eB_0}{2mc^2\beta_z} \qquad \alpha = \sqrt{k}L$$

The particles trajectories at the exit of the solenoid are parallel to the z axis if $k^{1/2} \tan\alpha = 1$. At a distance D_1 from the end of the solenoid the particle crosses the transverse plane at (x_1, y_1) such that

$$x_1^2 + y_1^2 = A^2(E)\left(x_0'^2 + y_0'^2\right)$$

where

$$A = D\cos\alpha + k^{-1/2}\sin\alpha - DD_1\,k^{1/2}\sin\alpha + D_1\cos\alpha \tag{4.3}$$

As a consequence, the focus for particles of a given energy occurs at a distance D_1 such that $A = 0$. If we put a collimator of radius r at $z = D + L + D_1$, only the particles having $A(x_0'^2 + y_0'^2)^{1/2} < r$ will get through and energy selection is achieved, even if secondary peaks exist as described in section 3.3. The presence of a low energy component is not desirable for the injection into a RF but it does not affect significantly the acceleration

process as we will show later. The elimination of this component can be achieved with a weak chicane or a thin foil. The absorption of these components in the linac would not be a problem due to their low intensity.

The particles with energy $E = 30$ MeV are focused at $z = 83$ cm namely after a drift of $D_1 = 51$ cm from the end of the solenoid, and there the second collimator is located, see figure 4.6.

The second collimator is chosen as a Al slab 1 cm thick, such that all protons up to 60 MeV are stopped. The hole is a cone with an aperture of 1 mm radius, small basis of 0.5 mm radius and height of 5 mm, followed by a cylinder of 0.5 mm radius and 5 mm height. The thickness of 5 mm is sufficient to stop protons up to 35 MeV.

We first perform a numerical selection of the spectrum at $E = 30 \pm 1$ MeV and follow the bunch along this transport line.

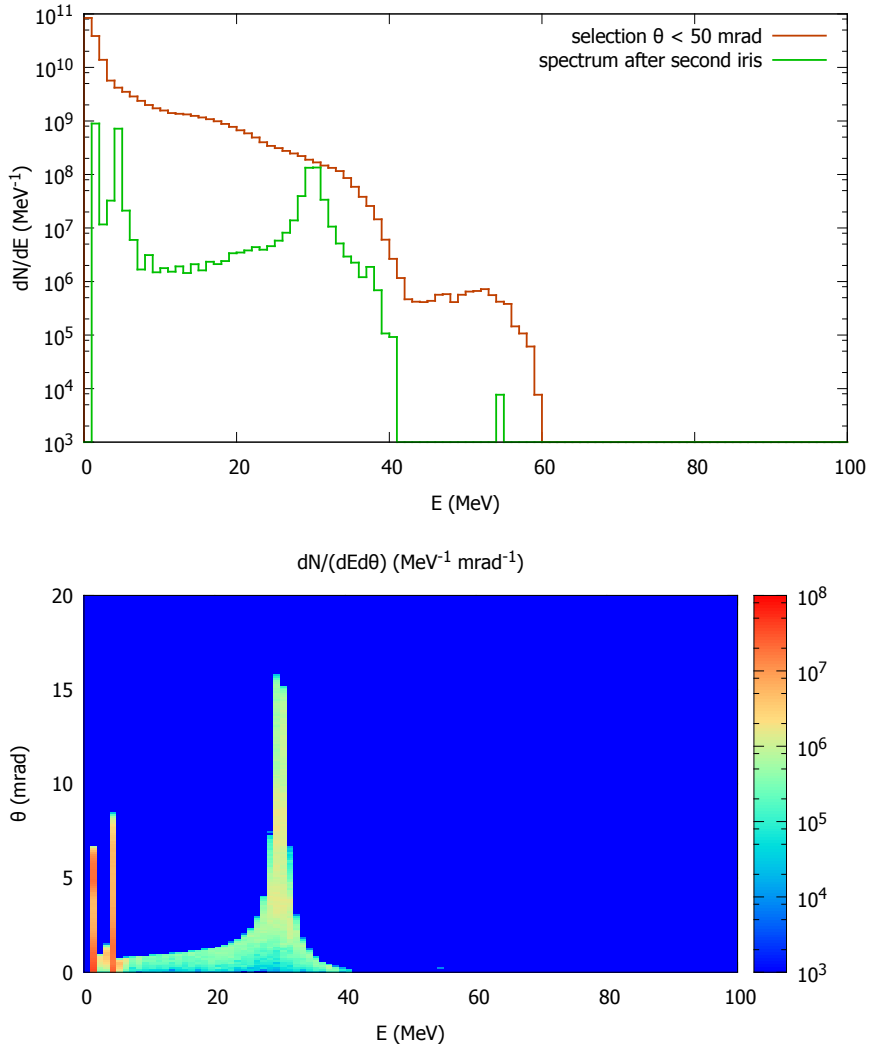

Figure 4.9: Upper frame: plot in a logarithmic scale of the proton energy spectrum after the second collimator (dark green curve) for the composite target foam+foil (TNSA) compared with the spectrum after the first collimator which selects the angle to $\theta < 50$ mrad (light brown curve). Lower frame: plot of the energy-angle distribution of the bunch after the second collimator in a logarithmic color scale

The corresponding transverse emittances and transverse size RMS values are shown in figure 4.7 where we choose $\langle z \rangle$ as independent variable. Along the same transport line,

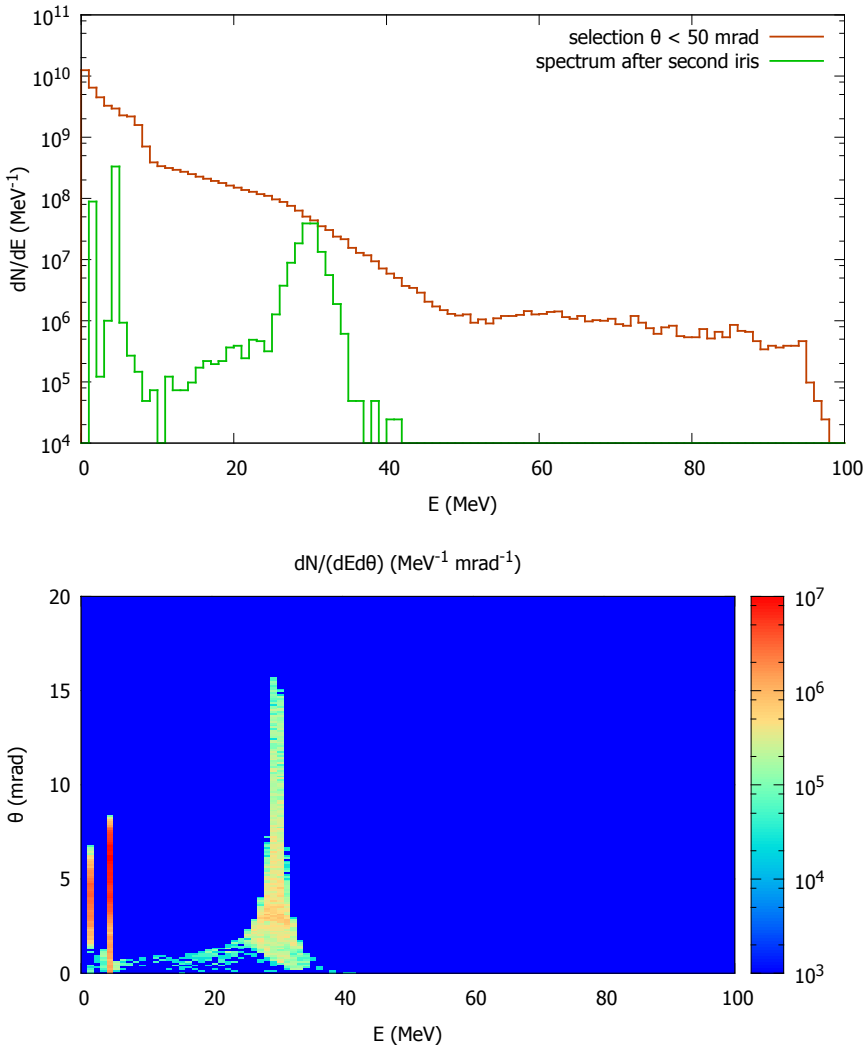

Figure 4.10: Upper frame: plot in a logarithmic scale of the proton energy spectrum after the second collimator (dark green curve) for the target with critical density (MVA) compared with the spectrum after the first collimator which selects the angle to $\theta < 50$ mrad (light brown curve). Lower frame: plot of the energy-angle distribution of the bunch after the second collimator in a logarithmic color scale

we have propagated all the protons in the energy interval $[3, 60]$ MeV. The transverse emittances and transverse RMS size values are reported in figure 4.8. We observe oscillations in the transverse RMS sizes and emittances because the slow protons are still in the solenoid long after the center of mass of the bunch has overcome it. As a consequence the interpretation of these plots is not intuitive. An exhaustive information can only be obtained from analyzing a full sequence of monochromatic energy slices.

The second collimator performs an energy selection as can be seen in figure 4.9 where we plot the energy distribution and the energy-angle distribution for the composite target (TNSA). In figure 4.10 the same distributions are shown for the target with critical density (MVA).

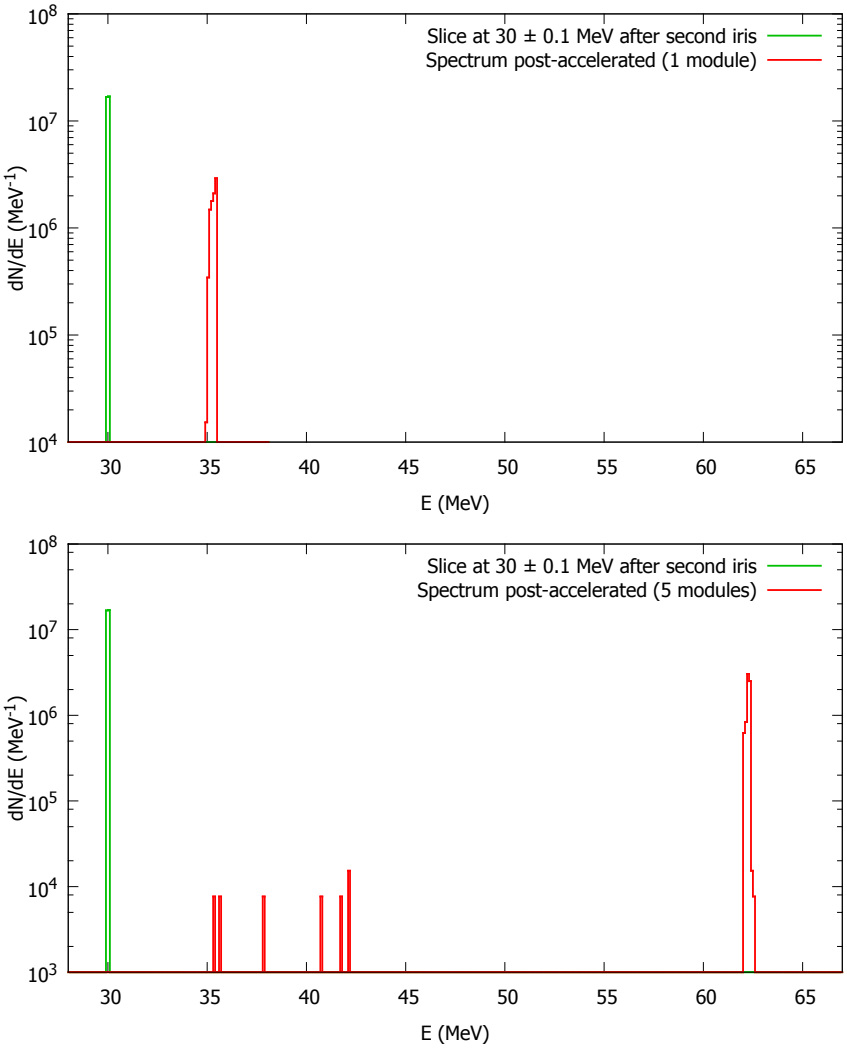

Figure 4.11: Upper frame: Energy spectra for a bunch with initial energy of 30 MeV $\pm$ 0.1 MeV (blue line) post-accelerated in 1 module of ACLIP (red line). Lower frame: post-acceleration in 5 modules. The values refer to the actual number of particles for each bin and each bin has a width of $\Delta E = 0.1$ MeV.

Post-acceleration

Starting from the bunch selected in energy by the previously described transport line, we have simulated the post-acceleration in the linac ACLIP. This was conceived as a Side Coupled Linac (SCL) designed as a booster for a 30 MeV proton injector working at 3 GHz. This high frequency implies a linac more compact and shorter than the standard lower-frequency proton linacs, used as injector of most synchrotrons, since the permissible accelerating field is roughly proportional to $f^{1/2}$ (f is the RF frequency) [109]. The final energy is 62 MeV.

The linac consists of 5 different modules, each with a maximum of 30 accelerating cells arranged in 2 tanks, powered by a single RF feed. Beam focusing is obtained through the use of permanent magnetic quadrupoles (PMQs). The total length of the five modules is 3.1 m. Eleven PMQs (gradient of 190 T/m) are positioned between the adjacent tanks and at the beginning and the exit of ACLIP. All the modules are essentially identical, except for their progressive increase in length, due both to the increasing velocity of the protons and

to the different numbers of accelerating cells. The RF design is based on the same mean accelerating field on axis in all the 10 tanks. The design foresees a mean axial field value of $E = 20$ MV/m.

The synchronization process between the laser pulse and the RF power amplifier can be a major issue. The phase acceptance window of the linac is of the order of 30 ps and it turns out that the synchronization among laser pulses and RF fields has to be in the ps scale. Nevertheless the SPARC Lab (Sorgente Pulsata Auto-amplificata di Radiazione Coerente) layout in Frascati already foresees devoted electronic and optical equipment to provide timing and synchronization in the femtosecond scale between 3 GHz accelerating structures of the electron linac SPARC and the laser pulses. The fast timing structure has been developed to allow Thompson emission and plasma acceleration experiments, and it is supposed here that the same infrastructure, with minor changes, can be used for these tests [110].

One of the critical issues of the hybrid acceleration scheme is compactness. The principal laser components can be located in a 20 m^2 room. The interaction chamber, the transport line and the linac (3.2 m long and less than 1 m wide) can be located in a radiation shielded room of a similar size.

The simulations of the post-acceleration stages have been carried out using ASTRA [94]. In figure 4.11 (upper frame) we can see that if we inject a monochromatic bunch at $E = 30$ MeV with a spread $\Delta E = 0.1$ MeV into the first module of ACLIP, in phase with the field in the cavity, a good portion of it is accelerated up to 35 MeV. After five modules the bunch is accelerated up to 62 MeV without additional losses, see lower frame of figure 4.11.

The monochromatic bunch is just a slice of the whole bunch that propagates along our beam-line. We have injected the whole bunch, obtained from the laser interaction with a composite foam+foil target (TNSA), coming out from the second collimator, and we found that a similar energy gain can be obtained. The final spectrum after five modules has a divergence less that 10 mrad, see figure 4.12 (lower frame). The energy distribution is peaked at 62 MeV with a spread less than 1 MeV and has a low background, see figure 4.12 (upper frame). The number of protons in the peak is $\sim 10^7$. The main bunch parameters, including efficiency and energy spread, for the composite target (TNSA) at various stages (initial, after first collimator, second collimator and at the end of the linac) are shown in table 4.1.

In figure 4.13 we consider the angle and energy distribution of the bunch obtained from the laser interaction with a target having critical density (MVA) post-accelerated after selection by the second collimator. We still observe the angle cutoff at 10 mrad, the energy peak at 62 MeV and a negligible background. The total number of protons is comparable.

$\langle z \rangle$ (cm)	$N_{p_{\mathrm{tot}}}$	$E_{p_{\mathrm{tot}}}$ (mJ)	ϵ_x (mm mrad)	ϵ_y (mm mrad)	$\Delta E/E$	$N_{p_{\mathrm{slice}}}$
0	$3.5\ 10^{11}$	195	0.021	0.023		$5.98\ 10^{8}$
1.5	$8.7\ 10^{10}$	79	0.24	0.21		$3.58\ 10^{8}$
84	$2.1\ 10^{9}$	2.8	0.48	1.91	3%	$2.69\ 10^{8}$
400	$8.4\ 10^{6}$	0.08	0.71	0.39	0.2%	$7.53\ 10^{6}$

Table 4.1: Bunch parameters for the composite target (TNSA) at different stages. The values quoted in the columns for $N_{p_{\mathrm{tot}}}$ and $E_{p_{\mathrm{tot}}}$ refer to the whole proton bunch, with $E > 1$ MeV for $z > 0$. The values quoted in the columns ϵ_x, ϵ_y, $\Delta E/E$, $N_{p_{\mathrm{slice}}}$ refer to the energy slice defined in the last column. The laser energy is 6.75 J. The energy spread ΔE for a distribution peaked at E is defined by $dN/dE(E \pm \Delta E) = e^{-1} dN/dE(E)$. The last column is referred to protons belonging to the slice 30 ± 1 MeV

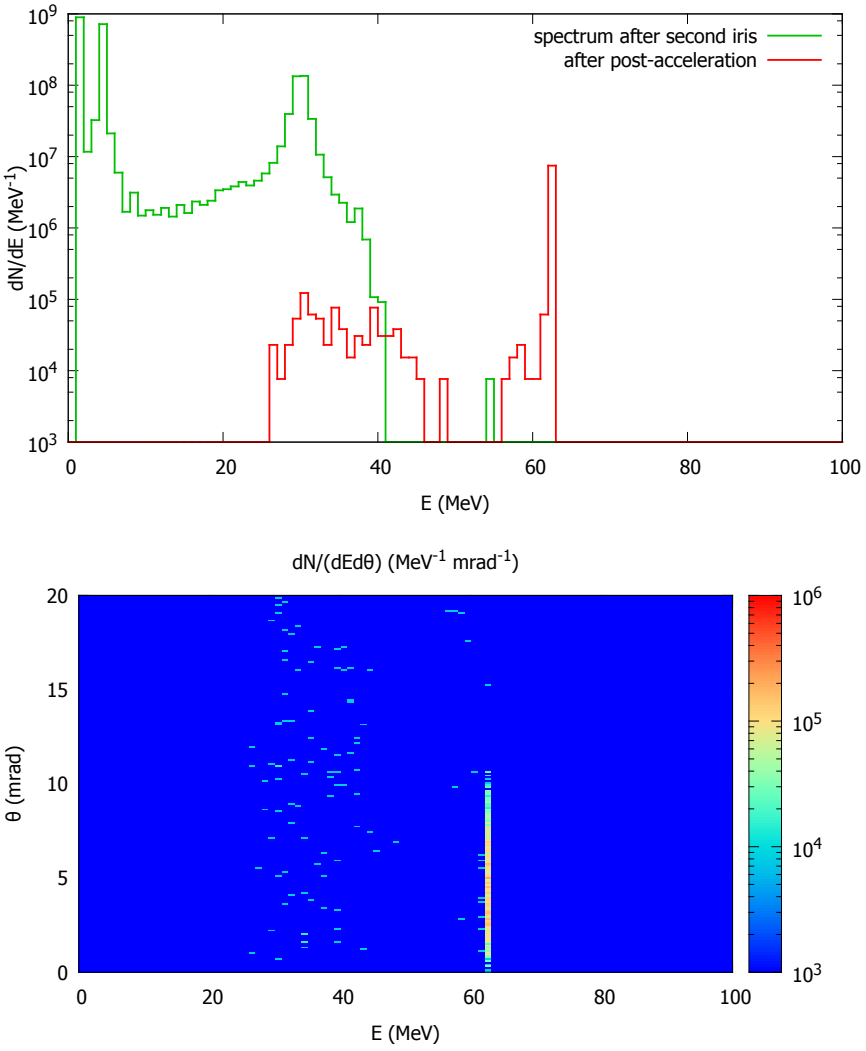

Figure 4.12: Upper frame: plot in a logarithmic scale of the proton energy spectrum after post-acceleration by five modules of ACLIP (red curve) for the composite target foam+foil (TNSA) compared with the spectrum after the second collimator which selects the angle to $\theta < 50$ mrad (dark green curve). Lower frame: plot of the energy-angle distribution after post-acceleration in a logarithmic color scale.

Considerations about this beamline

The beam has been injected into the linac and accelerated up to 35 MeV, with a single module, and up to 62 MeV, with 5 modules, without additional significant losses.

The conclusion is that one can post accelerate $\sim 10^7$ protons up to 62 MeV with a small spread $\Delta E/E < 1\%$ after an energy selection based on a solenoidal lens.

Acceleration to higher energies is possible using another stage such as the linac LIBO (LInac BOoster) [111, 112, 113].

Supposing that these results can be confirmed in a single shot experiment, important technological developments are necessary to reach the 10 Hz maximum laser repetition rate in a stable and reliable way.

The start-to-end simulation was carried out in order to avoid initial guesses on the laser accelerated proton beam and to follow consistently the evolution along the transport line and the accelerating modules. The neglected space charge effects are not expected to be

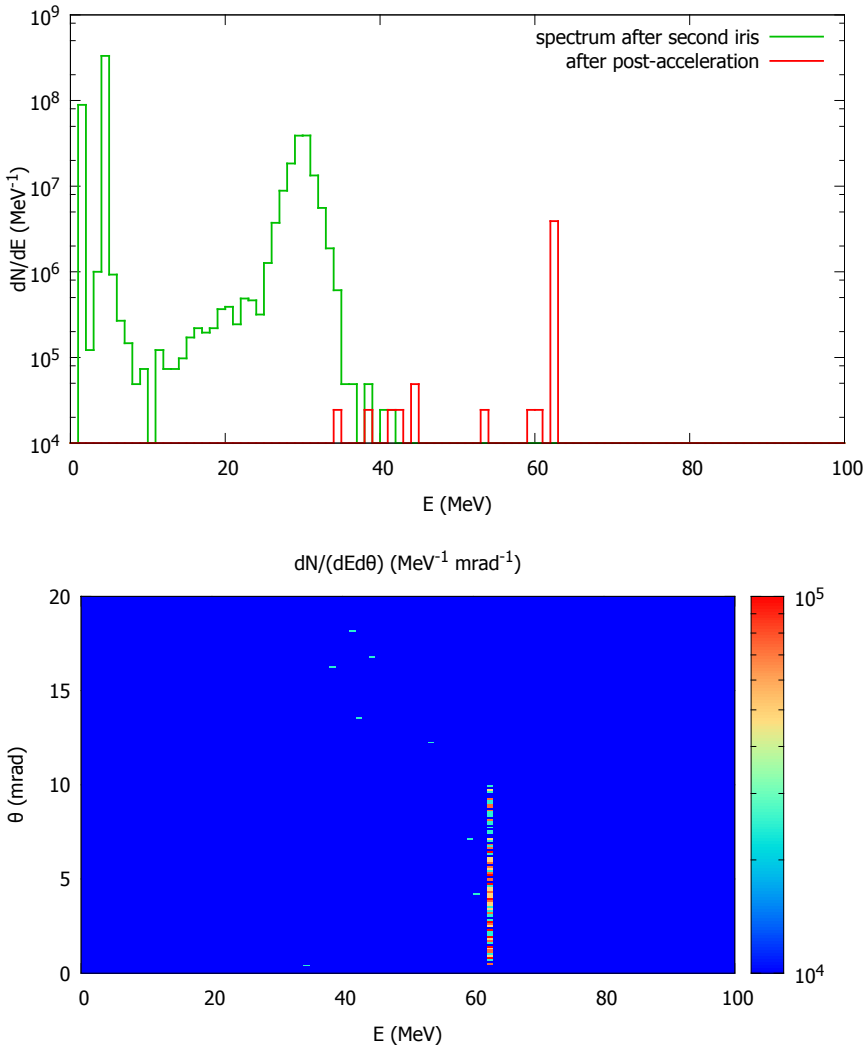

Figure 4.13: Upper frame: plot in a logarithmic scale of the proton energy spectrum after post-acceleration by five modules of ACLIP (red curve) for the target with quasi critical density (MVA) compared with the spectrum after the second collimator which selects the angle to $\theta < 50$ mrad (dark green curve). Lower frame: plot of the energy-angle distribution after post-acceleration in a logarithmic color scale.

relevant. What might be more relevant is the structure of the targets we used. Such foam-coated or quasi-critical density targets are not presently available. Taking into account also recent experimental results [114], one may estimate that using presently available targets the number of protons after energy selection would be $\sim 10^7$ and decrease to 10^6 or below after post-acceleration. The composite targets we have considered are much less sensitive to the thickness and electron density of the foil. As a consequence the results that we have obtained should be close to reality provided that a homogeneous foam layer can be prepared. The near critical targets, that are expected to be available soon from upgraded gas jets, have been modeled in a realistic way and might be the best candidates to provide a post-accelerated beam with 10^7 protons at a high repetition rate.

4.2.2 Beamline with quadrupoles or chicanes

Previously we have shown that a transport line based on two collimators and a high field solenoid is adequate to perform the energy and angular selection required for the injection into a compact linac.

Another work [84] was done using different lattice beamlines for the transport phase.

Beam focusing and energy selection are achieved also with multiplets of PMQ and, similarly to the solenoid case, selection is provided by a collimator located in the focal plane of protons of the chosen energy. Similar configurations have been already reported in literature [115, 116].

The laser beam we consider is very similar to the previous TNSA case: linearly polarized, has a duration of 40 fs FWHM and a peak intensity $I = 2\,10^{21}$ W/cm^2. Also the target is the same, in order to give comparable results: it is an Al foil of 0.8μm with a layer of foam 2 μm thick on the upstream side. With these parameters, we obtained in the simulation a maximum energy of $E_{\max} = 56$ MeV, with an average energy of $E_0 = 10$ MeV. It's different from before since the density of the target and the laser focal spot size are minimally different.

Let's say from the beginning that for PMQ transport line the number of energy selected protons is one order of magnitude lower than that for the solenoid.

We have also considered a chicane as a possible transport alternative for energy selection. Because this device is efficient for a parallel beam, the divergence of the beam in our case causes a decrease of the proton number by an additional order of magnitude after energy selection.

The quadrupole parameters are chosen in such a way that the focus in both xz and yz planes is the same, having denoted with z the beam propagation axis which is normal to the target. Since the beam size at the beginning is only a few μm, it can be considered point-like. The momenta of each macroparticle produced by the 3D PIC simulation are denoted by p_x, p_y, p_z and the angle with the z axis is $\theta = \arctan(p_\perp / p_z)$ where $p_\perp = (p_x^2 + p_y^2)^{1/2}$. The trajectory of each macroparticle is the same as a proton with the same initial conditions since the mass to charge ratio is the same. The angular deviations in the xz and yz planes are defined by $x' = p_x/p_z$, $y' = p_y/p_z$ and if we replace p_z by the momentum modulus p there is no significant difference as long as $p_\perp^2/p_z^2 \ll 1$.

The condition for the focus to be same in the xz and yz planes can be easily worked out in the thin lens approximation, using the equations described in section 3.2

A realistic and conservative solution is given in table 4.2.

Ξ	O	D	O	F	O	F	O	D	O
ℓ	2	6	4	6	4	6	4	6	45
ϱ		80		80		95		115	

Table 4.2: Ξ denotes the elements: O for a drift, F for a focusing quadrupole and D for a defocusing quadrupole; ℓ is the length, expressed in cm; ϱ is B_0/d, expressed in T/m

For protons with $E = 30$ MeV, the focus in x and y occurs for the same value $z_f = 83$ cm.

The full aperture of the quadrupoles is assumed to be 2 cm (1 cm radius); to avoid big losses inside the line, the first collimator selects protons with $|\theta| \leq 20$ mrad.

The energy and energy-angle spectra are shown in figure 4.14.

The number of selected protons is lower by almost one order of magnitude but, in

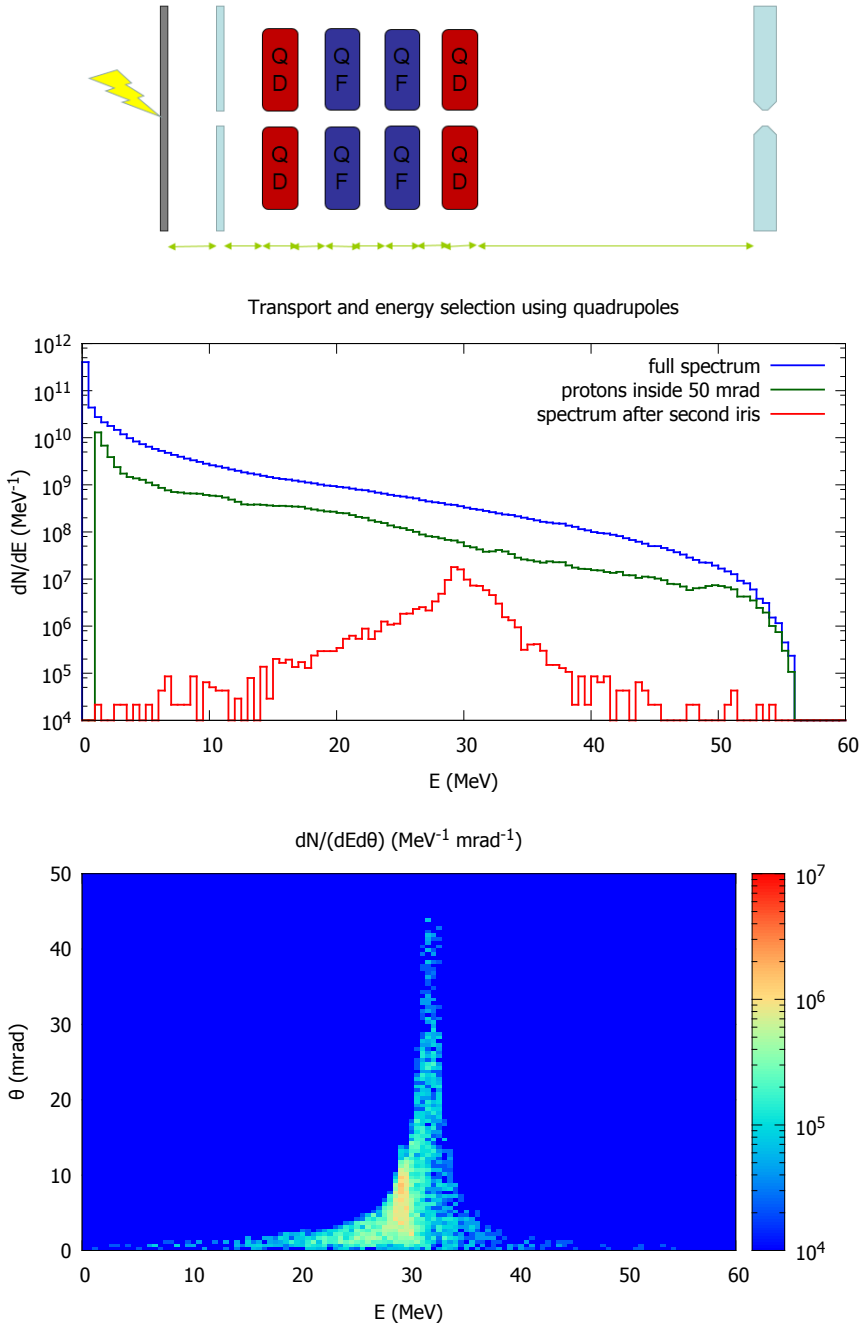

Figure 4.14: Upper frame: sketch of the transport line using a PMQ quadruplet. Middle frame: proton energy spectra for the the triple layer target. (cyan initial spectrum, green after selection at $|\theta| < 20$ mrad imposed by the first collimator, red after energy selection operated by the second collimator after the PMQ quadruplet). Lower frame: color plot for energy angle spectrum after energy selection by the PMQ quadruplet.

contrast to the solenoid case, no low energy peaks are present.

We have considered also the possibility of performing the energy selection with two magnetic dipoles (chicane), whose arrangement has been calculated following equations described in 3.1.

The chicane we have considered consists of two dipoles with $B_0 = 1$ T of extension $\ell = 10$ cm placed at a distance of 10 cm. No fringe fields have been considered. The spectrum after the selection by a slit with $\Delta x = 0.1$ cm, placed at a distance $D = 29$ cm

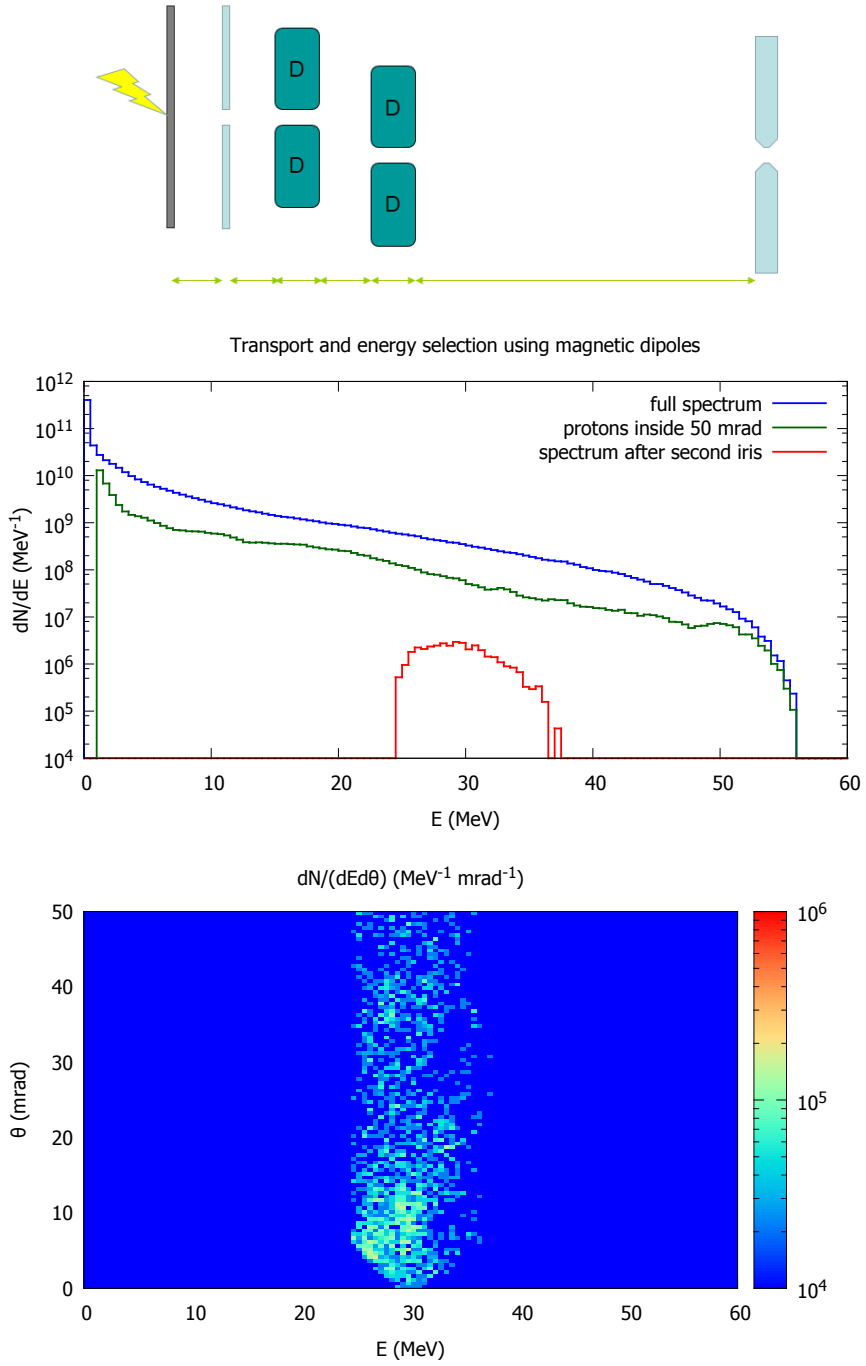

Figure 4.15: Upper frame: sketch of the transport line using magnetic dipoles. Middle frame: proton energy spectra for the triple layer target. (cyan initial spectrum, green after selection at $|\theta| < 10$ mrad imposed by the first collimator, red after energy selection operated by the second collimator after the chicane). Lower frame: color plot for energy angle spectrum after energy selection by the chicane.

from the second dipole, is shown in the upper frame of fig. 4.15. The initial angle selection has been restricted to $|\alpha| \leq 10$ mrad in order to have a good selection efficiency. The final number of selected protons is one order of magnitude lower than the system based on quadrupole transport.

We have also considered the same PMQ transport system with an aperture of 4 cm, rather than 2 cm, and an initial angular selection at 50 mrad, as for the solenoid. Even

though the initially collected number of protons is higher, the peak of the energy spectrum after the second collimator at the end of the line is not significantly enhanced, at the expense of the quality of the beam, so that the final number of protons suitable for post-acceleration is comparable with the previous case.

For the chicane, if we perform an initial selection at 50 mrad, the losses during the transport are much higher, so that the spectrum after the second collimator is about the same as for the initial selection at 10 mrad. A reduction in ΔE in the spectrum of the energy after the second collimator is possible reducing the size of the pinhole, but it causes even more losses for protons at 30 MeV. Considering the fact that the total number of injected protons is not very high, for now we consider that the losses inside the RF cavity are not a problem and reducing the size of the pinhole or moving it further are not worth enough.

Considerations about these beamline

We have considered different transport lines, based on a multiplet of PMQ and two magnetic dipoles to focus and achieve energy selection of a laser accelerated proton beam, in order to inject it into the first module of a linac.

Because of PMQ lower effectiveness with respect to the solenoid, in comparison with previous results, after the energy selection at 30 MeV the number of protons is lower by one order of magnitude; this is then reflected on the final beam intensity at the exit of the linac.

A selection system based on two magnetic dipoles appears to be effective only if the beam divergence is very low.

So, considering that only the very low initial divergent protons are going to survive this transport line, the final number of selected protons before injection and after post-acceleration is two orders of magnitude smaller than that of the solenoid based transport line.

Anyway, what we learned with these simulation was invaluable to learn the best methods to guide future post-acceleration experiments and the general development of hybrid integrated laser-driven ion accelerator systems (HILDIAS) [117].

4.3 Collaborating with KPSI

The conditions required for the injection into a compact linac like ACLIP could be achieved at the laser FLAME facility in Italy [118]. But it is also possible to obtain them in other facilities, like the Kansai Photon Science Institute (KPSI) in Japan.

In fact, as described in [114], recently they obtained protons with energy up to 40 MeV.

During the third year of my PhD I spent some months at the KPSI Institute. This was a great opportunity to have many fruitful discussions with some of the best talented people in this field, establish many connections that triggered interesting exchanges of ideas with people from there or just visiting the lab like me, and also because it offered me the opportunity to start working on a 3D PIC simulation that, for the first time, is trying to reproduce an experiment, understand the actual results and suggest future possible development paths.

The work is still completely in progress, but we hope to have publishable results as soon as possible. A brief description of the experiment conducted at the end of 2011 and later published in [114] follows.

4.3.1 Description of the recent results obtained at KPSI

At KPSI the laser available, J-KAREN, is a Ti:Sa hybrid laser system ($\lambda = 0.8\mu$m), with a nominal power of 200 TW and an optical parametric chirped-pulse amplification technology. They focused the linearly polarized laser pulse to intensity of up to 10^{21} W/cm^2 at the incidence angle of 45°. The pulse has an energy of 7.5 J and a length FWHM of 40 fs. The temporal contrast is 10^{10} : 1, obtained without plasma mirror but using a saturable absorber inserted between the high-energy CPA oscillator and the stretcher.

The laser pulses are focused in a spot that is 3 μm long (FWHM) along the laser polarization axis and 2 μm in the perpendicular plane. 23% of the full laser energy was contained in this spot.

It was measured, at 50 TW operation mode, that the temporal contrast of 3×10^{10} : 1 was maintained down to about 20 ps before the main pulse, with an estimation that this value lowered to 1×10^{10} : 1 in 200 TW mode. This means that a good portion of energy reached the target before the main pulse and so a proper description of the prepulse effect is extremely important to simulate this experiment.

Energy-resolved spatial distributions of proton fluence along the target normal were determined using nuclear track detector with CR-39 films, described in appendix A. This technology gives the ion energy and angular distribution, since the ion energy determines the penetration range, calibrated with SRIM [47, 48, 49].

Another point in favor of an important preplasma is the nearly absent specular reflection of the laser pulse. This indicates a substantial absorption of the main pulse at the target surface.

The proton energy spectrum is exemplified in figure 4.16, obtained counting the total number of protons at each CR-39 plate. This counts gave also an estimation of single shot conversion efficiency of the laser pulse energy into proton kinetic energy. For energies above 15 MeV, it is estimated around 0.1%, corresponding to a proton bunch energy of 7.5 mJ.

Since the CR-39 plates were all illuminated, up to the end, they were not able to measure the cut-off energy. From estimations using the hot electron temperature, they predicted a maximum proton energy of 54 MeV, values extremely interesting for our HILDIAS proposed structures.

A proper simulation work is still in progress. In the meantime, I was able to reproduce the spectrum using a different laser-target configuration. Results are presented in figures 4.16 and 4.17.

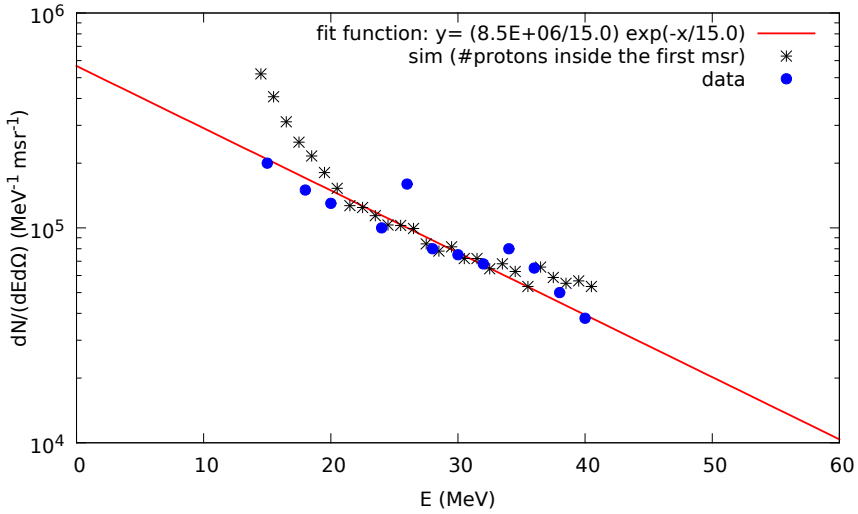

Figure 4.16: Proton spectrum obtained during the 2011 proton acceleration experiment at KPSI [114] and comparison with a preliminary PIC simulation.

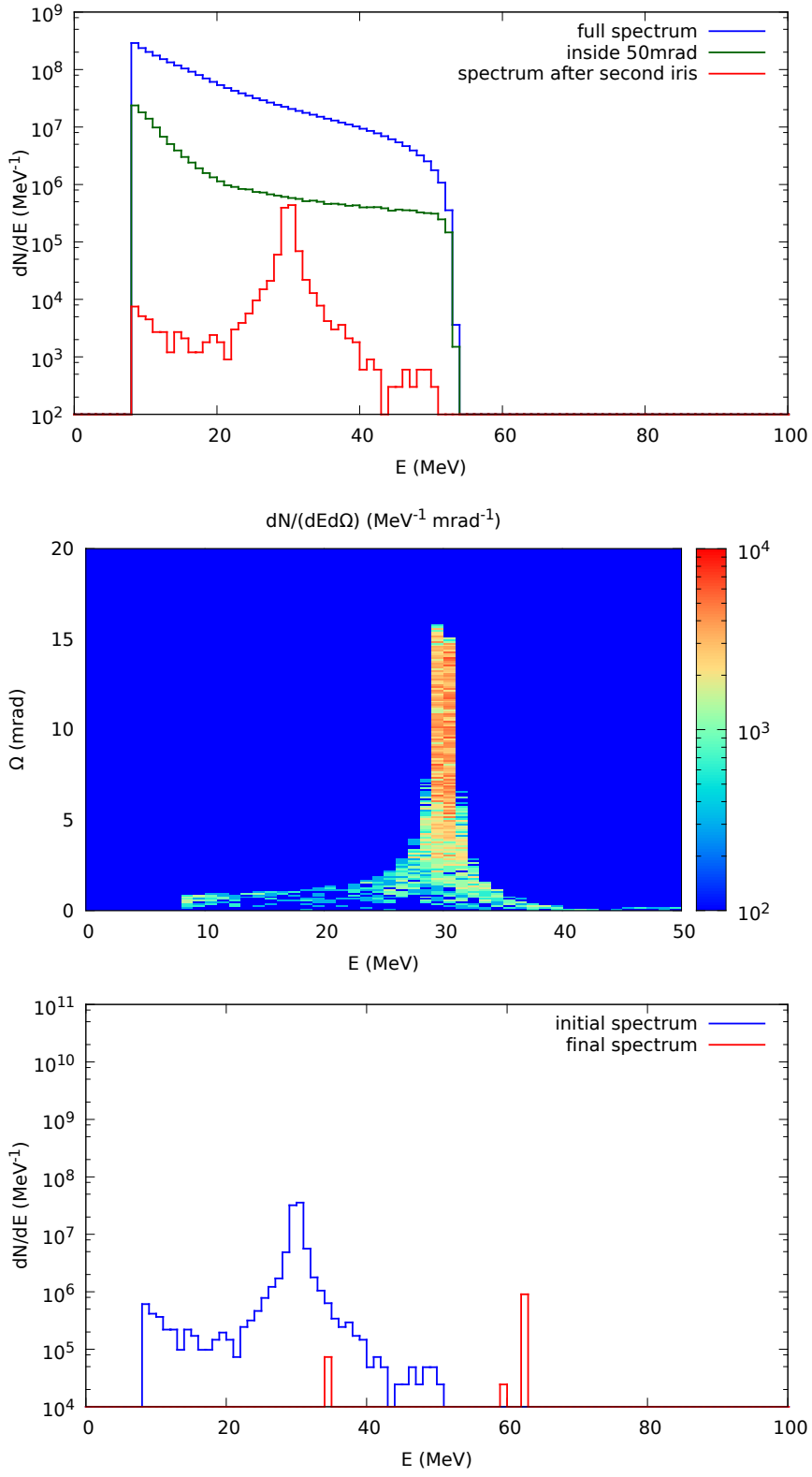

Figure 4.17: Test for a HILDIAS device for the proton bunch produced during the 2011 experiment at KPSI: in the first two frames there are the energy spectra and the energy-angle plot before and after the transport line based on a solenoid (30 cm, 10 T); in the third frame there's the energy spectra before and after the injection into the ACLIP RF cavity. Simulations will be optimized after a proper PIC simulation of the laser-plasma experiment will be done.

Conclusions

Laser driven particle acceleration is experiencing a thriving momentum since the recent developments in laser technologies. New experiments demonstrate the possibility to obtain proton beams with very high maximum energy from compact systems, while theoretical work is fervent in order to propose new schemes that can guarantee even higher quality bunches, associated with energies greater and greater.

An important part of this process is done by numerical simulations and in this thesis a technique widely used in this field, that is exploiting Particle In Cell algorithms, is described, analyzed and used, to study some interesting cases, using our code `ALaDyn` . It has been developed in the previous years and my work in this context was related to enhance its scaling on massively parallel architectures, while introducing at the same time new routines to deal with new target descriptions. This work was the basis for the subsequent process of beam analysis and shaping.

In fact, as extensively described throughout the thesis, laser driven proton energy spectra are exponential in nature. The main aim of this work was to study and design a beamline that control the emittance, reduce the size of the bunch and perform an energy selection on it, in order to obtain parameters that are comparable with the one from conventional accelerators, that were unmatched for quality.

From the simple chicane, built around a collection of magnetic dipoles, to quadrupoles, solenoids, RF cavities, many strategies have been analyzed throughout numerical simulations and analytical calculations and their results are reported. This work was driven with the purpose of designing a line already technically feasible, so that it would be possible to build it now and do some experiments with it.

The best beamline structure is obtained with a high field pulsed solenoid, coupled with a RF conventional linear accelerator, that doubles the final energy and performs a strict cleaning of the bunch.

Thanks to some good collaborations we have with other groups around the world, in this thesis there's described some work I did with GSI (Darmstadt-DE) on bunch deneutralization: removing electrons comoving with the protons, since they are unwanted, is a task of great interest and few ideas to do it are analyzed and simulated.

Another preliminary work presented here is done thanks to a collaboration with KPSI (Kyoto-JP) to reproduce with 3D numerical simulations an experiment they completed in 2011 and presented in 2012, when they obtained proton record energies of $\sim$ 40 MeV using the J-KAREN laser. This experiment is very well suited for our transport and post-acceleration studies and, on the grounds of a recent memorandum of understanding signed

by KPSI and INFN, it is possible that some of the results presented in this work will be tested in a real experiment in the next few years.

Bibliography

[1] Robert J. Van De Graaf. Electrostatic generator, feb 1935. US Patent 1,991,236.

[2] J. D. Cockcroft and E. T. S. Walton. Artificial production of fast protons. *Nature*, 129:242, 1932.

[3] Rolf Widerøe. Über ein neues prinzip zur herstellung hoher spannungen. *Archiv für Elektrotechnik*, 21(4):387–406, 1928.

[4] Ernest O. Lawrence. Method and apparatus for the acceleration of ions, feb 1934. US Patent 1,948,384.

[5] E.J.N. Wilson. Fifty years of synchrotrons. *Conf.Proc.*, C960610:135–139, 1996.

[6] T. Tajima and J. M. Dawson. Laser electron accelerator. *Phys. Rev. Lett.*, 43:267–270, Jul 1979.

[7] S. P. D. Mangles, C. D. Murphy, Z. Najmudin, A. G. R. Thomas, J. L. Collier, A. E. Dangor, E. J. Divall, P. S. Foster, J. G. Gallacher, C. J. Hooker, D. A. Jaroszynski, A. J. Langley, W. B. Mori, P. A. Norreys, F. S. Tsung, R. Viskup, B. R. Walton, and K. Krushelnick. Monoenergetic beams of relativistic electrons from intense laser-plasma interactions. *Nature*, 431(7008):535–538, September 2004.

[8] C. G. R. Geddes, C. Toth, J. van Tilborg, E. Esarey, C. B. Schroeder, D. Bruhwiler, C. Nieter, J. Cary, and W. P. Leemans. High-quality electron beams from a laser wakefield accelerator using plasma-channel guiding. *Nature*, (7008):538–541, 2004.

[9] J. Faure, Y. Glinec, A. Pukhov, S. Kiselev, S. Gordienko, E. Lefebvre, J.-P Rousseau, F. Burgy, and V. Malka. A laser-plasma accelerator producing monoenergetic electron beams. *Nature*, 431(7008):541–544, September 2004.

[10] W. P. Leemans, B. Nagler, A. J. Gonsalves, C. Tóth, K. Nakamura, C. G. R. Geddes, E. Esarey, C. B. Schroeder, and S. M. Hooker. GeV electron beams from a centimetre-scale accelerator. *Nature Physics*, 2:696–699, October 2006.

[11] Xiaoming Wang, Rafal Zgadzaj, Neil Fazel, Zhengyan Li, SA Yi, Xi Zhang, Watson Henderson, Y-Y Chang, R Korzekwa, H-E Tsai, et al. Quasi-monoenergetic laser-plasma acceleration of electrons to 2 gev. *Nature communications*, 4, 2013.

[12] R. A. Snavely, M. H. Key, S. P. Hatchett, T. E. Cowan, M. Roth, T. W. Phillips, M. A. Stoyer, E. A. Henry, T. C. Sangster, M. S. Singh, S. C. Wilks, A. MacKinnon, A. Offenberger, D. M. Pennington, K. Yasuike, A. B. Langdon, B. F. Lasinski, J. Johnson, M. D. Perry, and E. M. Campbell. Intense high-energy proton beams from petawatt-laser irradiation of solids. *Phys. Rev. Lett.*, 85:2945–2948, Oct 2000.

[13] Hiroyuki Daido, Mamiko Nishiuchi, and Alexander S Pirozhkov. Review of laser-driven ion sources and their applications. *Reports on Progress in Physics*, 75(5):056401, 2012.

[14] A. Einstein. Zur Quantentheorie der Strahlung. *Physikalische Zeitschrift*, 18:121–128, 1917.

[15] Arthur L. Schawlow and Charles H. Townes. Masers and maser communications system, mar 1960. US Patent 2,929,922.

[16] A. L. Schawlow and C. H. Townes. Infrared and optical masers. *Phys. Rev.*, 112:1940–1949, Dec 1958.

[17] D. Strickland and G. Mourou. Compression of amplified chirped optical pulses. *Optics Communications*, 55:447–449, October 1985.

[18] S. Fritzler, V. Malka, G. Grillon, J. P. Rousseau, F. Burgy, E. Lefebvre, E. d'Humiéres, P. McKenna, and K. W. D. Ledingham. Proton beams generated with high-intensity lasers: Applications to medical isotope production. *Applied Physics Letters*, 83(15):3039–3041, 2003.

[19] Takashi Fujii, Yuji Oishi, Takuya Nayuki, Yasushi Takizawa, Koshichi Nemoto, Tsutomu Kayoiji, Kazuhiko Horioka, Yasuaki Okano, Yoichiro Hironaka, Kazutaka G. Nakamura, and Ken-ichi Kondo. MeV-order proton and carbon ion acceleration by irradiation of 60 fs TW laser pulses on thin copper tape. *Applied Physics Letters*, 83(8):1524–1526, 2003.

[20] Y. Oishi, T. Nayuki, T. Fujii, Y. Takizawa, X. Wang, T. Yamazaki, K. Nemoto, T. Kayoiji, T. Sekiya, K. Horioka, Y. Okano, Y. Hironaka, K. G. Nakamura, K. Kondo, and A. A. Andreev. Dependence on laser intensity and pulse duration in proton acceleration by irradiation of ultrashort laser pulses on a Cu foil target. *Physics of Plasmas (1994-present)*, 12(7), 2005.

[21] I. Spencer, K. W. D. Ledingham, P. McKenna, T. McCanny, R. P. Singhal, P. S. Foster, D. Neely, A. J. Langley, E. J. Divall, C. J. Hooker, R. J. Clarke, P. A. Norreys, E. L. Clark, K. Krushelnick, and J. R. Davies. Experimental study of proton emission from 60 fs, 200 mJ high-repetition-rate tabletop-laser pulses interacting with solid targets. *Phys. Rev. E*, 67:046402, Apr 2003.

[22] A. J. Mackinnon, Y. Sentoku, P. K. Patel, D. W. Price, S. Hatchett, M. H. Key, C. Andersen, R. Snavely, and R. R. Freeman. Enhancement of proton acceleration by hot-electron recirculation in thin foils irradiated by ultraintense laser pulses. *Phys. Rev. Lett.*, 88:215006, May 2002.

[23] M. Kaluza, J. Schreiber, M. I. K. Santala, G. D. Tsakiris, K. Eidmann, J. Meyer-ter Vehn, and K. J. Witte. Influence of the laser prepulse on proton acceleration in thin-foil experiments. *Phys. Rev. Lett.*, 93:045003, Jul 2004.

[24] M. Roth, A. Blazevic, M. Geissel, T. Schlegel, T. E. Cowan, M. Allen, J.-C. Gauthier, P. Audebert, J. Fuchs, J. Meyer-ter Vehn, M. Hegelich, S. Karsch, and A. Pukhov. Energetic ions generated by laser pulses: A detailed study on target properties. *Phys. Rev. ST Accel. Beams*, 5:061301, Jun 2002.

[25] M. Allen, Y. Sentoku, P. Audebert, A. Blazevic, T. Cowan, J. Fuchs, J. C. Gauthier, M. Geissel, M. Hegelich, S. Karsch, E. Morse, P. K. Patel, and M. Roth. Proton spectra from ultraintense laser–plasma interaction with thin foils: Experiments, theory, and simulation. *Physics of Plasmas (1994-present)*, 10(8):3283–3289, 2003.

[26] A. Maksimchuk, K. Flippo, H. Krause, G. Mourou, K. Nemoto, D. Shultz, D. Umstadter, R. Vane, V.Yu. Bychenkov, G.I. Dudnikova, V.F. Kovalev, K. Mima, V.N. Novikov, Y. Sentoku, and S.V. Tolokonnikov. High-energy ion generation by short laser pulses. *Plasma Physics Reports*, 30(6):473–495, 2004.

[27] K. Krushelnick, E. L. Clark, M. Zepf, J. R. Davies, F. N. Beg, A. Machacek, M. I. K. Santala, M. Tatarakis, I. Watts, P. A. Norreys, and A. E. Dangor. Energetic proton production from relativistic laser interaction with high density plasmas. *Physics of Plasmas (1994-present)*, 7(5):2055–2061, 2000.

[28] P. McKenna, K. W. D. Ledingham, J. M. Yang, L. Robson, T. McCanny, S. Shimizu, R. J. Clarke, D. Neely, K. Spohr, R. Chapman, R. P. Singhal, K. Krushelnick, M. S. Wei, and P. A. Norreys. Characterization of proton and heavier ion acceleration in ultrahigh-intensity laser interactions with heated target foils. *Phys. Rev. E*, 70:036405, Sep 2004.

[29] P. McKenna, K. W. D. Ledingham, S. Shimizu, J. M. Yang, L. Robson, T. McCanny, J. Galy, J. Magill, R. J. Clarke, D. Neely, P. A. Norreys, R. P. Singhal, K. Krushelnick, and M. S. Wei. Broad energy spectrum of laser-accelerated protons for spallation-related physics. *Phys. Rev. Lett.*, 94:084801, Mar 2005.

[30] M. Zepf, E. L. Clark, K. Krushelnick, F. N. Beg, C. Escoda, A. E. Dangor, M. I. K. Santala, M. Tatarakis, I. F. Watts, P. A. Norreys, R. J. Clarke, J. R. Davies, M. A. Sinclair, R. D. Edwards, T. J. Goldsack, I. Spencer, and K. W. D. Ledingham. Fast particle generation and energy transport in laser-solid interactions. *Physics of Plasmas (1994-present)*, 8(5):2323–2330, 2001.

[31] M. Borghesi, J. Fuchs, S. V. Bulanov, A. J. Mackinnon, P. K. Patel, and M. Roth. Fast ion generation by high-intensity laser irradiation of solid targets and applications. *Fusion Science and Technology*, 49(3):412–439, 2006.

[32] P. J. Morrison. Hamiltonian and action principle formulations of plasma physicsa). *Physics of Plasmas (1994-present)*, 12(5), 2005.

[33] Alain J. Brizard. A new lagrangian formulation for laser-plasma interactions. *Physics of Plasmas (1994-present)*, 5(4):1110–1117, 1998.

[34] C.K. Birdsall and A.B. Langdon. *Plasma Physics via Computer Simulation*. Series in Plasma Physics. Taylor & Francis, 2004.

[35] E.G. Evstatiev and B.A. Shadwick. Variational formulation of particle algorithms for kinetic plasma simulations. *Journal of Computational Physics*, 245:376 – 398, 2013.

[36] C. Benedetti, P. Londrillo, L. Rossi, and G. Turchetti. Numerical investigation of Maxwell-Vlasov equations – part i: Basic physics and algorithms. *Communications in Nonlinear Science and Numerical Simulation*, 13(1):204 – 208, 2008. Vlasovia 2006: The Second International Workshop on the Theory and Applications of the Vlasov Equation.

[37] C. Benedetti, A. Sgattoni, G. Turchetti, and P. Londrillo. ALaDyn: A high-accuracy PIC code for the Maxwell-Vlasov equations. *IEEE Transactions on Plasma Science*, 36(4):1790 –1798, aug. 2008.

[38] P. Londrillo, C. Benedetti, A. Sgattoni, and G. Turchetti. Charge preserving high order PIC schemes. *Nuclear Instruments and Methods in Physics Research Section A: Accelerators, Spectrometers, Detectors and Associated Equipment*, 620(1):28 – 35, 2010. Coulomb'09 - Ions Acceleration with high Power Lasers: Physics and Applications.

[39] Francesco Rossi, Pasquale Londrillo, Andrea Sgattoni, Stefano Sinigardi, and Giorgio Turchetti. Towards robust algorithms for current deposition and dynamic load-balancing in a GPU particle in cell code. *AIP Conference Proceedings*, 1507(1):184–192, 2012.

[40] G. Grittani, M.P. Anania, G. Gatti, D. Giulietti, M. Kando, M. Krus, L. Labate, T. Levato, P. Londrillo, F. Rossi, and L.A. Gizzi. High energy electrons from interaction with a structured gas-jet at {FLAME}. *Nuclear Instruments and Methods in Physics Research Section A: Accelerators, Spectrometers, Detectors and Associated Equipment*, 2013.

[41] V. Malka. Laser plasma accelerators. *Physics of Plasmas*, 19(5), 2012.

[42] E. Esarey, C. B. Schroeder, and W. P. Leemans. Physics of laser-driven plasma-based electron accelerators. *Rev. Mod. Phys.*, 81:1229–1285, Aug 2009.

[43] A. Pukhov and J. Meyer-ter Vehn. Laser wake field acceleration: the highly non-linear broken-wave regime. *Applied Physics B*, 74(4-5):355–361, 2002.

[44] William I. Linlor. Ion energies produced by laser giant pulse. *Applied Physics Letters*, 3(11):210–211, 1963.

[45] J. A. Stamper and B. H. Ripin. Faraday-rotation measurements of megagauss magnetic fields in laser-produced plasmas. *Phys. Rev. Lett.*, 34:138–141, Jan 1975.

[46] S. J. Gitomer, R. D. Jones, F. Begay, A. W. Ehler, J. F. Kephart, and R. Kristal. Fast ions and hot electrons in the laser–plasma interaction. *Physics of Fluids (1958-1988)*, 29(8):2679–2688, 1986.

[47] James F. Ziegler, M.D. Ziegler, and J.P. Biersack. SRIM : The stopping and range of ions in matter. *Nuclear Instruments and Methods in Physics Research Section B: Beam Interactions with Materials and Atoms*, 268(11-12):1818 – 1823, 2010. 19th International Conference on Ion Beam Analysis.

[48] J.P. Biersack and J.F. Ziegler. The stopping and range of ions in solids. In Heiner Ryssel and Hans Glawischnig, editors, *Ion Implantation Techniques*, volume 10 of *Springer Series in Electrophysics*, pages 122–156. Springer Berlin Heidelberg, 1982.

[49] J.F. Ziegler, J.P. Biersack, and U. Littmark. *The Stopping and Range of Ions in Solids*. Stopping and Range of Ions in Matter, Vol 1. Pergamon Press, 1985.

[50] Isidore Last, Israel Schek, and Joshua Jortner. Energetics and dynamics of coulomb explosion of highly charged clusters. *The Journal of Chemical Physics*, 107(17):6685–6692, 1997.

[51] T. Ditmire, J. W. G. Tisch, E. Springate, M. B. Mason, N. Hay, R. A. Smith, J. Marangos, and M. H. R. Hutchinson. High-energy ions produced in explosions of superheated atomic clusters. *Nature*, 386:54–56, March 1997.

[52] Luís O. Silva, Michael Marti, Jonathan R. Davies, Ricardo A. Fonseca, Chuang Ren, Frank S. Tsung, and Warren B. Mori. Proton shock acceleration in laser-plasma interactions. *Phys. Rev. Lett.*, 92:015002, Jan 2004.

[53] M. S. Wei, S. P. D. Mangles, Z. Najmudin, B. Walton, A. Gopal, M. Tatarakis, A. E. Dangor, E. L. Clark, R. G. Evans, S. Fritzler, R. J. Clarke, C. Hernandez-Gomez, D. Neely, W. Mori, M. Tzoufras, and K. Krushelnick. Ion acceleration by collisionless shocks in high-intensity-laser–underdense-plasma interaction. *Phys. Rev. Lett.*, 93:155003, Oct 2004.

[54] L. Yin, B. J. Albright, B. M. Hegelich, K. J. Bowers, K. A. Flippo, T. J. T. Kwan, and J. C. Fernández. Monoenergetic and GeV ion acceleration from the laser breakout afterburner using ultrathin targets. *Physics of Plasmas (1994-present)*, 14(5), 2007.

[55] B. J. Albright, L. Yin, Kevin J. Bowers, B. M. Hegelich, K. A. Flippo, T. J. T. Kwan, and J. C. Fernández. Relativistic buneman instability in the laser breakout afterburner. *Physics of Plasmas (1994-present)*, 14(9), 2007.

[56] M. Roth, I. Alber, V. Bagnoud, C. R. D. Brown, R. Clarke, H. Daido, J. Fernandez, K. Flippo, S. Gaillard, C. Gauthier, M. Geissel, S. Glenzer, G. Gregori, M. Günther, K. Harres, R. Heathcote, A. Kritcher, N. Kugland, S. LePape, B. Li, M. Makita, J. Mithen, C. Niemann, F. Nürnberg, D. Offermann, A. Otten, A. Pelka, D. Riley, G. Schaumann, M. Schollmeier, J. Schütrumpf, M. Tampo, and A. Tauschwitz. Proton acceleration experiments and warm dense matter research using high power lasers. *Plasma Physics and Controlled Fusion*, 51(12):124039, 2009.

[57] Daniel Jung. *Ion acceleration from relativistic laser nano-target interaction*. PhD thesis, Ludwig-Maximilians-Universität München, Fakultät für Physik, 2012.

[58] Yasuaki Kishimoto, Kunioki Mima, Tsuguhiro Watanabe, and Kyoji Nishikawa. Analysis of fast-ion velocity distributions in laser plasmas with a truncated maxwellian velocity distribution of hot electrons. *Physics of Fluids (1958-1988)*, 26(8):2308–2315, 1983.

[59] Stephen P. Hatchett, Curtis G. Brown, Thomas E. Cowan, Eugene A. Henry, Joy S. Johnson, Michael H. Key, Jeffrey A. Koch, A. Bruce Langdon, Barbara F. Lasinski, Richard W. Lee, Andrew J. Mackinnon, Deanna M. Pennington, Michael D. Perry, Thomas W. Phillips, Markus Roth, T. Craig Sangster, Mike S. Singh, Richard A. Snavely, Mark A. Stoyer, Scott C. Wilks, and Kazuhito Yasuike. Electron, photon, and ion beams from the relativistic interaction of petawatt laser pulses with solid targets. *Physics of Plasmas (1994-present)*, 7(5):2076–2082, 2000.

[60] S. C. Wilks, A. B. Langdon, T. E. Cowan, M. Roth, M. Singh, S. Hatchett, M. H. Key, D. Pennington, A. MacKinnon, and R. A. Snavely. Energetic proton generation in ultra-intense laser–solid interactions. *Physics of Plasmas (1994-present)*, 8(2):542–549, 2001.

[61] A. Pukhov and J. Meyer-ter Vehn. Relativistic magnetic self-channeling of light in near-critical plasma: Three-dimensional particle-in-cell simulation. *Phys. Rev. Lett.*, 76:3975–3978, May 1996.

[62] M. Passoni and M. Lontano. One-dimensional model of the electrostatic ion acceleration in the ultraintense laser-solid interaction. *Laser and Particle Beams*, 22(02):163–169, 2004.

[63] A. Sgattoni. *Theoretical and numerical study of the laser-plasma ion acceleration*. PhD thesis, University of Bologna, 2011.

[64] M. Passoni, V. T. Tikhonchuk, M. Lontano, and V. Yu. Bychenkov. Charge separation effects in solid targets and ion acceleration with a two-temperature electron distribution. *Phys. Rev. E*, 69:026411, Feb 2004.

[65] P. Mora. Plasma expansion into a vacuum. *Phys. Rev. Lett.*, 90:185002, May 2003.

[66] T. Esirkepov, M. Yamagiwa, and T. Tajima. Laser ion-acceleration scaling laws seen in multiparametric particle-in-cell simulations. *Phys. Rev. Lett.*, 96:105001, Mar 2006.

[67] T. Esirkepov, M. Borghesi, S. V. Bulanov, G. Mourou, and T. Tajima. Highly efficient relativistic-ion generation in the laser-piston regime. *Phys. Rev. Lett.*, 92:175003, Apr 2004.

[68] Andrea Macchi, Tatiana V. Liseikina, Sara Tuveri, and Silvia Veghini. Theory and simulation of ion acceleration with circularly polarized laser pulses. *Comptes Rendus Physique*, 10(2–3):207 – 215, 2009. Laser acceleration of particles in plasma - Accélération laser de particules dans les plasmas.

[69] Andrea Macchi and Carlo Benedetti. Ion acceleration by radiation pressure in thin and thick targets. *Nuclear Instruments and Methods in Physics Research Section A: Accelerators, Spectrometers, Detectors and Associated Equipment*, 620(1):41 – 45, 2010. Coulomb'09 - Ions Acceleration with high Power Lasers: Physics and Applications.

[70] Andrea Macchi, Federica Cattani, Tatiana V. Liseykina, and Fulvio Cornolti. Laser acceleration of ion bunches at the front surface of overdense plasmas. *Phys. Rev. Lett.*, 94:165003, Apr 2005.

[71] Andrea Macchi, Silvia Veghini, and Francesco Pegoraro. "Light Sail" acceleration reexamined. *Phys. Rev. Lett.*, 103:085003, Aug 2009.

[72] A.V. Kuznetsov, T.Zh. Esirkepov, F.F. Kamenets, and S.V. Bulanov. Efficiency of ion acceleration by a relativistically strong laser pulse in an underdense plasma. *Plasma Physics Reports*, 27(3):211–220, 2001.

[73] G. A. Askar'yan, S. V. Bulanov, F. Pegoraro, and A. M. Pukhov. Magnetic interaction of self-focusing channels and fluxes of electromagnetic radiation: their coalescence, the accumulation of energy, and the effect of external magnetic fields on them. *Soviet Journal of Experimental and Theoretical Physics Letters*, 60:251, August 1994.

[74] G. Mourou, Z. Chang, A. Maksimchuk, J. Nees, S.V. Bulanov, V.Yu. Bychenkov, T.Zh. Esirkepov, N.M. Naumova, F. Pegoraro, and H. Ruhl. On the design of experiments for the study of relativistic nonlinear optics in the limit of single-cycle pulse duration and single-wavelength spot size. *Plasma Physics Reports*, 28(1):12–27, 2002.

[75] S. V. Bulanov, M. Lontano, T. Zh. Esirkepov, F. Pegoraro, and A. M. Pukhov. Electron vortices produced by ultraintense laser pulses. *Phys. Rev. Lett.*, 76:3562–3565, May 1996.

[76] Tatsufumi Nakamura and Kunioki Mima. Magnetic-dipole vortex generation by propagation of ultraintense and ultrashort laser pulses in moderate-density plasmas. *Phys. Rev. Lett.*, 100:205006, May 2008.

[77] Tatsufumi Nakamura, Sergei V. Bulanov, Timur Zh. Esirkepov, and Masaki Kando. High-energy ions from near-critical density plasmas via magnetic vortex acceleration. *Phys. Rev. Lett.*, 105:135002, Sep 2010.

[78] P. Londrillo, G. Servizi, A. Sgattoni, S. Sinigardi, M. Sumini, and G. Turchetti. *CO_2 laser optimization and applications*, chapter 17. Protons acceleration by CO_2 laser pulses and perspectives for medical applications. Intech, 2011.

[79] H. Wiedemann. *Particle Accelerator Physics*. Advanced Texts in Physics. Springer, 2003.

[80] N. Christofilos. Focussing system for ions and electrons, feb 1956. US Patent 2,736,799.

[81] Ernest D. Courant, M. Stanley Livingston, and Hartland S. Snyder. The strong-focusing synchroton – a new high energy accelerator. *Phys. Rev.*, 88:1190–1196, Dec 1952.

[82] J. P. Blewett. Radial focusing in the linear accelerator. *Phys. Rev.*, 88:1197–1199, Dec 1952.

[83] M. Reiser. *Theory and Design of Charged Particle Beams*. Wiley Series in Beam Physics and Accelerator Technology. Wiley, 2008.

[84] Stefano Sinigardi, Giorgio Turchetti, Francesco Rossi, Pasquale Londrillo, Dario Giove, Carlo De Martinis, and Paul R. Bolton. High quality proton beams from hybrid integrated laser-driven ion acceleration systems. *Nuclear Instruments and Methods in Physics Research Section A: Accelerators, Spectrometers, Detectors and Associated Equipment*, 2013.

[85] Stefano Sinigardi, Giorgio Turchetti, Pasquale Londrillo, Francesco Rossi, Dario Giove, Carlo De Martinis, and Marco Sumini. Transport and energy selection of laser generated protons for postacceleration with a compact linac. *Phys. Rev. ST Accel. Beams*, 16:031301, Mar 2013.

[86] M. Nishiuchi, H. Sakaki, T. Hori, P. R. Bolton, K. Ogura, A. Sagisaka, A. Yogo, M. Mori, S. Orimo, A. S. Pirozhkov, I. Daito, H. Kiriyama, H. Okada, S. Kanazawa, S. Kondo, T. Shimomura, M. Tanoue, Y. Nakai, H. Sasao, D. Wakai, H. Daido, K. Kondo, H. Souda, H. Tongu, A. Noda, Y. Iseki, T. Nagafuchi, K. Maeda, K. Hanawa, T. Yoshiyuki, and T. Shirai. Measured and simulated transport of 1.9 MeV laser-accelerated proton bunches through an integrated test beam line at 1 Hz. *Phys. Rev. ST Accel. Beams*, 13:071304, Jul 2010.

[87] Masahiro Ikegami, Shu Nakamura, Yoshihisa Iwashita, Toshiyuki Shirai, Hikaru Souda, Yujiro Tajima, Mikio Tanabe, Hiromu Tongu, Hiroyuki Itoh, Hiroki Shintaku, Atsushi Yamazaki, Hiroyuki Daido, Akifumi Yogo, Satoshi Orimo, Michiaki

Mori, Mamiko Nishiuchi, Koichi Ogura, Akito Sagisaka, Alexander S. Pirozhkov, Hiromitsu Kiriyama, Shyuhei Kanazawa, Shuji Kondo, Yoichi Yamamoto, Takuya Shimomura, Manabu Tanoue, Yoshimoto Nakai, Atsushi Akutsu, Sergei V. Bulanov, Toyoaki Kimura, Yuji Oishi, Koshichi Nemoto, Toshiki Tajima, and Akira Noda. Radial focusing and energy compression of a laser-produced proton beam by a synchronous RF field. *Phys. Rev. ST Accel. Beams*, 12:063501, Jun 2009.

[88] A. Noda, Y. Iwashita, H. Souda, H. Tongu, A. Wakita, H. Daido, M. Ikegami, H. Kiriyama, M. Mori, M. Nishiuchi, K. Ogura, S. Orimo, A. Pirozhkov, A. Sagisaka, A. Yogo, and T. Shirai. Quality improvement of laser produced protons by phase rotation and its possible extension to higher energies. In *Proton and Ion Accelerators and applications – Proceedings of LINAC08 Victoria BC, Canada (MOP060)*, page 216, 2008.

[89] Shu Nakamura, Masahiro Ikegami, Yoshihisa Iwashita, Toshiyuki Shirai, Hiromu Tongu, Hikaru Souda, Hiroyuki Daido, Michiaki Mori, Masataka Kado, Akito Sagisaka, Koichi Ogura, Mamiko Nishiuchi, Satoshi Orimo, Yukio Hayashi, Akifumi Yogo, Alexander S. Pirozhkov, Sergei V. Bulanov, Timur Esirkepov, Akira Nagashima, Toyoaki Kimura, Toshiki Tajima, Takeshi Takeuchi, Atsushi Fukumi, Zhong Li, and Akira Noda. High-quality laser-produced proton beam realized by the application of a synchronous RF electric field. *Japanese Journal of Applied Physics*, 46(29):L717–L720, 2007.

[90] Toma Toncian, Marco Borghesi, Julien Fuchs, Emmanuel d'Humières, Patrizio Antici, Patrick Audebert, Erik Brambrink, Carlo Alberto Cecchetti, Ariane Pipahl, Lorenzo Romagnani, and Oswald Willi. Ultrafast laser-driven microlens to focus and energy-select mega-electron volt protons. *Science*, 312(5772):410–413, 2006.

[91] D. A. Swenson, D. E. Young, and B. Austin. Comparison of particle motions as calculated by two different dynamics programs. In *Proceedings of the 1966 Linear Accelerator Conference, Los Alamos, New Mexico, USA*, pages 229–232, 1966.

[92] Karl L. Brown and Sam Howry. TRANSPORT/360: A computer program for designing charged particle beam transport systems. 1970.

[93] K. Flöttmann. ASTRA. `http://www.desy.de/~mpyflo`, 2000.

[94] K. Flöttmann, S. M. Lidia, and P. Piot. Recent improvements to the ASTRA particle tracking code. In *Proceedings of PAC03*, pages 3500–3502, 2003.

[95] Y. Fukuda, A. Ya. Faenov, M. Tampo, T. A. Pikuz, Nakamura T., M. Kando, Y. Hayashi, A. Yogo, H. Sakaki, T. Kameshima, A. S. Pirozhkov, K. Ogura, M. Mori, T. Zh. Esirkepov, J. Koga, A. S. Boldarev, V. A. Gasilov, A. I. Magunov, T. Yamauchi, R. Kodama, P. R. Bolton, Y. Kato, T. Tajima, H. Daido, and S. V. Bulanov. Energy increase in multi-MeV ion acceleration in the interaction of a short pulse laser with a cluster-gas target. *Phys. Rev. Lett.*, 103:165002, Oct 2009.

[96] Tatsufumi Nakamura, Motonobu Tampo, Rryosuke Kodama, Sergei V. Bulanov, and Masaki Kando. Interaction of high contrast laser pulse with foam-attached target. *Physics of Plasmas*, 17(11):113107, 2010.

[97] F. Brunel. Not-so-resonant, resonant absorption. *Phys. Rev. Lett.*, 59:52–55, Jul 1987.

[98] T. Z. Esirkepov, J. K. Koga, A. Sunahara, T. Morita, M. Nishikino, K. Kageyama, H. Nagatomo, K. Nishihara, A. Sagisaka, H. Kotaki, T. Nakamura, Y. Fukuda, H. Okada, A. Pirozhkov, A. Yogo, M. Nishiuchi, H. Kiriyama, K. Kondo, M. Kando, and S. V. Bulanov. Prepulse and amplified spontaneous emission effects on the interaction of a petawatt class laser with thin solid targets. *ArXiv e-prints*, October 2013.

[99] T. Utsumi, K. Matsukado, H. Daido, T.Z. Esirkepov, and S.V. Bulanov. Numerical simulation of melting and evaporation of a cold foil target irradiated by a pre-pulse. *Applied Physics A*, 79(4-6):1185–1187, 2004.

[100] Paul Gibbon and A. R. Bell. Collisionless absorption in sharp-edged plasmas. *Phys. Rev. Lett.*, 68:1535–1538, Mar 1992.

[101] P. Gibbon, A. Andreev, E. Lefebvre, G. Bonnaud, H. Ruhl, J. Delettrez, and A. R. Bell. Calibration of one-dimensional boosted kinetic codes for modeling high-intensity laser–solid interactions. *Physics of Plasmas (1994-present)*, 6(3):947–953, 1999.

[102] W. P. Wang, B. F. Shen, H. Zhang, Y. Xu, Y. Y. Li, X. M. Lu, C. Wang, Y. Q. Liu, J. X. Lu, Y. Shi, Y. X. Leng, X. Y. Liang, R. X. Li, N. Y. Wang, and Z. Z. Xu. Effects of nanosecond-scale prepulse on generation of high-energy protons in target normal sheath acceleration. *Applied Physics Letters*, 102(22), 2013.

[103] R. Ramis, R. Schmalz, and J. Meyer-Ter-Vehn. MULTI — a computer code for one-dimensional multigroup radiation hydrodynamics. *Computer Physics Communications*, 49(3):475 – 505, 1988.

[104] V. G. Vaccaro, M. R. Masullo, C. De Martinis, D. Giove, A. Rainò, V. Variale, S. Mathot, R. J. Rush, and M. Iskander. RF high power tests on the first module of the ACLIP linac. In *Proceedings of PAC09, Vancouver, BC, Canada*, 2009.

[105] V. G. Vaccaro, R. Buiano, A. D'Elia, G. De Michele, M. R. Masullo, F. Alessandria, D. Giove, C. De Martinis, E. Di Betta, M. Mauri, A. Rainò, V. Variale, L. Calabretta, and R. J. Rush. ACLIP: A 3 GHz Side Coupled Linac for protontherapy to be used as a booster for 30 MeV cyclotrons. In *Cyclotrons and Their Applications, Eighteenth International Conference*, 2007.

[106] Ingo Hofmann, Jürgen Meyer-ter Vehn, Xueqing Yan, Anna Orzhekhovskaya, and Stepan Yaramyshev. Collection and focusing of laser accelerated ion beams for therapy applications. *Phys. Rev. ST Accel. Beams*, 14:031304, Mar 2011.

[107] I. Hofmann, A. Orzhekhovskaya, S. Yaramyshev, M. Roth, and M. Droba. Laser accelerated ions and their potential for therapy accelerators. In *Proceedings of HIAT09, Venice ITALY*, 2009.

[108] Ingo Hofmann, Jürgen Meyer ter Vehn, Xueqing Yan, and Husam Al-Omari. Chromatic energy filter and characterization of laser-accelerated proton beams for particle therapy. *Nuclear Instruments and Methods in Physics Research Section A: Accelerators, Spectrometers, Detectors and Associated Equipment*, 681:44 – 54, 2012.

[109] W. D. Kilpatrick. Criterion for vacuum sparking designed to include both RF and DC. *Review of Scientific Instruments*, 28(10):824–826, 1957.

[110] A. Gallo, D. Alesini, M. Bellaveglia, G. Gatti, and C. Vicario. Performances of the SPARC laser and RF synchronization systems. In *Proceedings of EPAC08, Genoa, Italy*, pages 3354–3356, 2008.

[111] C. De Martinis, C. Birattari, D. Giove, L. Serafini, P. Berra, E. Rosso, B. Szeless, U. Amaldi, K. Crandall, M. Mauri, D. Toet, M. Weiss, R. Zennaro, M. R. Masullo, V. G. Vaccaro, L. Calabretta, and A. Rovelli. Beam tests on a proton linac booster for hadrontherapy. In *Proceedings EPAC 2002*, pages 2717–2729, 2002.

[112] U. Amaldi, P. Berra, K. Crandall, D. Toet, M. Weiss, R. Zennaro, E. Rosso, B. Szeless, M. Vretenar, C. Cicardi, C. De Martinis, D. Giove, D. Davino, M. R. Masullo, and V. Vaccaro. LIBO: a linac-booster for protontherapy: construction and tests of a prototype. *Nuclear Instruments and Methods in Physics Research Section A: Accelerators, Spectrometers, Detectors and Associated Equipment*, 521(2 - 3):512 – 529, 2004.

[113] C. De Martinis, D. Giove, U. Amaldi, P. Berra, K. Crandall, M. Mauri, M. Weiss, R. Zennaro, E. Rosso, B. Szeless, M. Vretenar, M.R. Masullo, V. Vaccaro, L. Calabretta, and A. Rovelli. Acceleration tests of a 3 GHz proton linear accelerator LIBO for hadrontherapy. *Nuclear Instruments and Methods in Physics Research Section A: Accelerators, Spectrometers, Detectors and Associated Equipment*, 681:10 – 15, 2012.

[114] Koichi Ogura, Mamiko Nishiuchi, Alexander S. Pirozhkov, Tsuyoshi Tanimoto, Akito Sagisaka, Timur Zh. Esirkepov, Masaki Kando, Toshiyuki Shizuma, Takehito Hayakawa, Hiromitsu Kiriyama, Takuya Shimomura, Shyuji Kondo, Shuhei Kanazawa, Yoshiki Nakai, Hajime Sasao, Fumitaka Sasao, Yuji Fukuda, Hironao Sakaki, Masato Kanasaki, Akifumi Yogo, Sergei V. Bulanov, Paul R. Bolton, and Kiminori Kondo. Proton acceleration to 40 MeV using a high intensity, high contrast optical parametric chirped-pulse amplification/Ti:Sapphire hybrid laser system. *Opt. Lett.*, 37(14):2868–2870, Jul 2012.

[115] T. Burris-Mog, K. Harres, F. Nürnberg, S. Busold, M. Bussmann, O. Deppert, G. Hoffmeister, M. Joost, M. Sobiella, A. Tauschwitz, B. Zielbauer, V. Bagnoud, T. Herrmannsdoerfer, M. Roth, and T. E. Cowan. Laser accelerated protons captured and transported by a pulse power solenoid. *Phys. Rev. ST Accel. Beams*, 14:121301, Dec 2011.

[116] M. Schollmeier, S. Becker, M. Geißel, K. A. Flippo, A. Blažević, S. A. Gaillard, D. C. Gautier, F. Grüner, K. Harres, M. Kimmel, F. Nürnberg, P. Rambo, U. Schramm, J. Schreiber, J. Schütrumpf, J. Schwarz, N. A. Tahir, B. Atherton, D. Hab, B. M. Hegelich, and M. Roth. Controlled transport and focusing of laser-accelerated protons with miniature magnetic devices. *Phys. Rev. Lett.*, 101:055004, Aug 2008.

[117] Paul R. Bolton. Developing integrated, laser-driven ion accelerator systems. In *Proceedings of the Coulomb11 Workshop*, pages 17–22, Bologna, IT, 2012. Bononia University Press.

[118] M. Ferrario, D. Alesini, M. Anania, A. Bacci, M. Bellaveglia, O. Bogdanov, R. Boni, M. Castellano, E. Chiadroni, A. Cianchi, S.B. Dabagov, C. De Martinis, D. Di Giovenale, G. Di Pirro, U. Dosselli, A. Drago, A. Esposito, R. Faccini, A. Gallo, M. Gambaccini, C. Gatti, G. Gatti, A. Ghigo, D. Giulietti, A. Ligidov, P. Londrillo, S. Lupi, A. Mostacci, E. Pace, L. Palumbo, V. Petrillo, R. Pompili, A.R. Rossi, L. Serafini, B. Spataro, P. Tomassini, G. Turchetti, C. Vaccarezza, F. Villa, G. Dattoli, E. Di Palma,

L. Giannessi, A. Petralia, C. Ronsivalle, I. Spassovsky, V. Surrenti, L. Gizzi, L. Labate, T. Levato, and J.V. Rau. SPARC-LAB present and future. *Nuclear Instruments and Methods in Physics Research Section B: Beam Interactions with Materials and Atoms*, 309:183–188, 2013. The 5th International Conference Channeling 2012, Charged and Neutral Particles Channeling Phenomena, September 23-28,2012, Alghero (Sardinia), Italy.

[119] G. Battistoni, F. Cerutti, A. Fassó, A. Ferrari, S. Muraro, J. Ranft, S. Roesler, and P. R. Sala. The FLUKA code: description and benchmarking. *AIP Conference Proceedings*, 896(1):31–49, 2007.

[120] Alfredo Ferrari, Paola R. Sala, Alberto Fassó, and Johannes Ranft. FLUKA: A multi-particle transport code. *CERN Reports*, 2005.

[121] J.J. Thomson. Further experiments on positive rays. *The London, Edinburgh, and Dublin Philosophical Magazine and Journal of Science*, 24(140):209–253, 1912.

[122] K. Zeil, S. D. Kraft, S. Bock, M. Bussmann, T. E. Cowan, T. Kluge, J. Metzkes, T. Richter, R. Sauerbrey, and U. Schramm. The scaling of proton energies in ultrashort pulse laser plasma acceleration. *New Journal of Physics*, 12(4):045015, 2010.

[123] J. K. Salmon. *Parallel hierarchical N-body methods*. PhD thesis, California Institute of Technology, Pasadena., 1991.

[124] M. Plum, J. Allen, M. Borden, D. Fitzgerald, R. Macek, and T.S. Wang. Electron clearing in the Los Alamos Proton Storage Ring. In *Proceedings of the 1995 Particle Accelerator Conference*, volume 5, pages 3406–3408 vol.5, 1995.

[125] M. Plum. Electric fields, electron production, and electron motion at the stripper foil in the Los Alamos Proton Storage Ring. In *Proceedings of the 1995 Particle Accelerator Conference*, volume 5, pages 3403–3405 vol.5, 1995.

[126] G. Hoehler (Editor), E. A. Niekisch (Editor), and J. Treusch (Editor). *Particle Induced Electron Emission: v. 1*. Springer Tracts in Modern Physics. Springer-Verlag Berlin and Heidelberg GmbH, 1991.

[127] G. Hoehler (Editor), E. A. Niekisch (Editor), and J. Treusch (Editor). *Particle Induced Electron Emission: v. 2*. Springer Tracts in Modern Physics. Springer-Verlag Berlin and Heidelberg GmbH, 1992.

[128] J. Allison, K. Amako, J. Apostolakis, H. Araujo, P.A. Dubois, M. Asai, G. Barrand, R. Capra, S. Chauvie, R. Chytracek, G. A P Cirrone, G. Cooperman, G. Cosmo, G. Cuttone, G. G. Daquino, M. Donszelmann, M. Dressel, G. Folger, F. Foppiano, J. Generowicz, V. Grichine, S. Guatelli, P. Gumplinger, A. Heikkinen, I. Hrivnacova, A. Howard, S. Incerti, V. Ivanchenko, T. Johnson, F. Jones, T. Koi, R. Kokoulin, M. Kossov, H. Kurashige, V. Lara, S. Larsson, F. Lei, O. Link, F. Longo, M. Maire, A. Mantero, B. Mascialino, I. McLaren, P.M. Lorenzo, K. Minamimoto, K. Murakami, P. Nieminen, L. Pandola, S. Parlati, L. Peralta, J. Perl, A. Pfeiffer, M.G. Pia, A. Ribon, P. Rodrigues, G. Russo, S. Sadilov, G. Santin, T. Sasaki, D. Smith, N. Starkov, S. Tanaka, E. Tcherniaev, B. Tome, A. Trindade, P. Truscott, L. Urban, M. Verderi, A. Walkden, J. P. Wellisch, D.C. Williams, D. Wright, and H. Yoshida. GEANT4 developments and applications. *IEEE Transactions on Nuclear Science*, 53(1):270–278, 2006.

[129] S. Agostinelli, J. Allison, K. Amako, J. Apostolakis, H. Araujo, P. Arce, M. Asai, D. Axen, S. Banerjee, G. Barrand, F. Behner, L. Bellagamba, J. Boudreau, L. Broglia, A. Brunengo, H. Burkhardt, S. Chauvie, J. Chuma, R. Chytracek, G. Cooperman, G. Cosmo, P. Degtyarenko, A. Dell'Acqua, G. Depaola, D. Dietrich, R. Enami, A. Feliciello, C. Ferguson, H. Fesefeldt, G. Folger, F. Foppiano, A. Forti, S. Garelli, S. Giani, R. Giannitrapani, D. Gibin, J.J. Gómez Cadenas, I. González, G. Gracia Abril, G. Greeniaus, W. Greiner, V. Grichine, A. Grossheim, S. Guatelli, P. Gumplinger, R. Hamatsu, K. Hashimoto, H. Hasui, A. Heikkinen, A. Howard, V. Ivanchenko, A. Johnson, F.W. Jones, J. Kallenbach, N. Kanaya, M. Kawabata, Y. Kawabata, M. Kawaguti, S. Kelner, P. Kent, A. Kimura, T. Kodama, R. Kokoulin, M. Kossov, H. Kurashige, E. Lamanna, V. Lara, V. Lefebure, F. Lei, M. Liendl, W. Lockman, F. Longo, S. Magni, M. Maire, E. Medernach, K. Minamimoto, P. Mora de Freitas, Y. Morita, K. Murakami, M. Nagamatu, R. Nartallo, P. Nieminen, T. Nishimura, K. Ohtsubo, M. Okamura, S. O'Neale, Y. Oohata, K. Paech, J. Perl, A. Pfeiffer, M.G. Pia, F. Ranjard, A. Rybin, S. Sadilov, E. Di Salvo, G. Santin, T. Sasaki, N. Savvas, Y. Sawada, S. Scherer, S. Sei, V. Sirotenko, D. Smith, N. Starkov, H. Stoecker, J. Sulkimo, M. Takahata, S. Tanaka, E. Tcherniaev, E. Safai Tehrani, M. Tropeano, P. Truscott, H. Uno, L. Urban, P. Urban, M. Verderi, A. Walkden, W. Wander, H. Weber, J.P. Wellisch, T. Wenaus, D.C. Williams, D. Wright, T. Yamada, H. Yoshida, and D. Zschiesche. GEANT4: a simulation toolkit. *Nuclear Instruments and Methods in Physics Research Section A: Accelerators, Spectrometers, Detectors and Associated Equipment*, 506(3):250 – 303, 2003.

[130] Romuald Duperrier, Nicolas Pichoff, and Didier Uriot. Cea saclay codes review for high intensities linacs computations. In *Proceedings of the International Conference on Computational Science-Part III*, ICCS '02, pages 411–418, London, UK, UK, 2002. Springer-Verlag.

[131] David K. Brice. Stopping powers for electrons and positrons (ICRU report 37; international commission on radiation units and measurements, bethesda, maryland, usa, 1984). *Nuclear Instruments and Methods in Physics Research Section B: Beam Interactions with Materials and Atoms*, 12(1):187 – 188, 1985.

[132] M. J. Berger. ESTAR, PSTAR, and ASTAR: Computer programs for calculating stopping-power and range tables for electrons, protons, and helium ions. Technical report, IBM Research, December 1992.

[133] INFN Collaboration. SL-LILIA INFN project. `http://sl-lilia.mi.infn.it`.

[134] ELI Collaboration. Extreme Light Infrastructure european project. `http://www.extreme-light-infrastructure.eu`.

A Detectors

A.1 CR-39

CR-39, or allyl diglycol carbonate (ADC), is a plastic polymer commonly used in the manufacture of eyeglass lenses. The abbreviation stands for "Columbia Resin #39", because it was the 39th formula of a thermosetting plastic developed by the Columbia Resins project in 1940

It's born as a multipurpose plastic; thanks to its low chromatic aberration, it's an advantageous material for eyeglasses and sunglasses. It's a plastic polymer resistant to most solvents and other chemicals, gamma radiation, can be used continuously in temperature up to 100 °C. Anyway, it is also a great solid state nuclear track detector: CR-39 is used in fact in many laboratories to detect the presence of ionizing radiation. Energetic particles colliding with the polymer structure leave a trail of broken chemical bonds and when immersed in a concentrated alkali solution,hydroxide ions attack and break the polymer structure, etching away the bulk of the plastic at a nominally fixed rate. However, along the paths of damage left by charged particle interaction, the concentration of radiation damage allows the chemical agent to attack the polymer more rapidly than it does in the bulk, revealing the paths of the charged ions.

As this brief description perhaps clearly explain, CR-39 is extremely cheap, but also extremely time-consuming to use as a detector. In fact, simple things like counting the tracks at different material depths is usually done manually.

A numerical model of a CR-39 detector can be fully realized with FLUKA [119, 120], but to correlate depth and energy of the proton simpler programs like SRIM [47, 48, 49] are much more common in laboratories.

A.2 Radiochromic films

Measuring the depth-dose distribution using conventional measuring systems, such as ionization chambers, semiconductors, thermoluminescent detectors (TLDs) and radiographic films, can be very cumbersome.

The difficulties encountered resulted in a search for a radiation dosimeter with high spatial resolution which does not require a special developmental procedure, while giving permanent absolute values and being acceptably accurate and precise.

Some of these features have been achieved with the introduction of radiochromic dosimeters, under the commercial name of GafChromic. They offer very high spatial resolution, relatively low spectral sensitivity variation, they are insensitive to visible light (allowing

handling and preparation of experiments in room light). On top of that, radiochromic dosimeters color directly and do not require chemical processing.

A.3 Thomson Parabola

The Thomson parabola spectrometer, a device built in 1912 by J. J. Thomson to discover the electron [121], is successfully used also in laser-plasma acceleration experiment as charged particles analyzer for studying ion beams ejected. As described in chapter 3.1, it consists of parallel electric and magnetic fields and both perpendicular to the direction of the incident beam. The main feature of this kind of spectrometer is to provide information on energy and charge-to-mass ratio of the deflected ions.

Assuming that both field are uniform over a length L and zero outside, using a small angle approximation by setting $\tan\theta \approx \theta$,it can be shown that the trajectories of non-relativistic ions moving perpendicularly to the electric field is parabolic and the deflection angle at the exit of the electrodes is:

$$\theta_e = \frac{ZeEL}{A\mu v^2} = \frac{ZeEL}{2E_{\text{kin}}}$$

where θ_e is the electric deflection angle in radians, Z is the charge state of the ion, e is the electronic charge, EL is the product of the electric field and its length, A is the ion mass number, μ is the proton mass, v and E_{kin} are the velocity and kinetic energy of the ion.

Similarly, the trajectories of ions moving perpendicularly to the magnetic field is circular and the deflection angle at the exit of the magnets is:

$$\theta_m = \frac{eBL}{A\mu v} = \frac{ZeBL}{\sqrt{2A\mu E_{\text{kin}}}}$$

where θ_m is the magnetic deflection angle in radians and BL is the product of the magnetic field and its length.

Since the fields are parallel, the corresponding deflections are orthogonal each other. The electric and magnetic deflection are proportional to the corresponding deflection angles by:

$$\theta_i = x_i / D$$

where $i = e, m$ stays for electric or magnetic angle and D is the drift length between the electromagnetic device and the detector plane. Thus assuming that the magnetic field deflects on x axis and the electric field deflects on y axis, from the above equations one gets:

$$y = \frac{qELD}{2E_{\text{kin}}} \qquad\qquad x = \frac{qBLD}{\sqrt{2}mv}$$

where $q = Ze$ is the ion charge and $m = A\mu$ is its mass in kilograms.

Solving the second equation for v and replacing it in the first one we get the parabolic equation:

$$y = \frac{mE}{qLDB^2}x^2$$

which means that particles with the same charge-to-mass ratio and different energies are deflected on a parabolic trace on the detector plane. The previous equation shows that

a Thomson spectrometer provides a separation of all ion species and charge state according to their q/m. Every single parabola on the detector belongs to a different ion charge-to-mass state ratio. The information one can obtain from the two-dimensional deflection can be directly derived from previous equations. For instance, the momentum per charge can be found as:

$$\frac{A\mu v}{Ze} = \frac{BL}{\theta_m} \qquad\qquad \frac{mv}{q} = \frac{BLD}{\sqrt{2}x}$$

which is inversely proportional to the magnetic deflection and independent to the electric one. Thus in the plane θ_e vs θ_m any horizontal line θ_m = const. corresponds to a constant momentum per charge.

Similarly, the kinetic energy per charge can be expressed as

$$\frac{1}{2}\frac{A\mu v^2}{Ze} = \frac{1}{2}\frac{EL}{\theta_e} \qquad\qquad \frac{mv^2}{q} = \frac{ELD}{y}$$

which is inversely proportional to the electric deflection and independent to the magnetic one. Thus in the plane θ_e vs θ_m any horizontal line θ_e = const. corresponds to a constant energy per charge.

The ions velocity can be found by taking the ratio of the first two equations as:

$$v = \frac{EL}{BL}\frac{\theta_m}{\theta_e}$$

which is independent on charge or mass. This means that any straight line crossing the origin of the deflection coordinates is a constant velocity line.

Similarly, we can find the charge-to-mass ratio of ions as:

$$\frac{Ze}{A\mu} = \frac{EL}{(BL)^2}\frac{\theta_m^2}{\theta_e}$$

Thus ions of different energies with the same charge-to-mass ratio form a parabolic trace on the deflection plane.

The Thomson spectrometer provides the charge-to-mass ratio of a given parabola using a reference parabola of known q/m ratio.

Thomson spectrometer does not indicate the charge or mass of the parabola separately but the number of intersections of the constant velocity line from the origin to the parabola of interest can give information on the charge state. Thus knowing the charge-to-mass ratio and the charge state it is possible to get the ion mass and to identify the ion species.

An interesting feature of the spectrogram is that the peak energy per charge of each parabolas is constant.

During my PhD I was one of the tutor of F. Schillaci, that wrote his master thesis on this topic.

B

Bunch de-neutralization

B.1 An overview of the problem

Bunches from the TNSA acceleration are charge neutral [122]. Because of these charge-neutrality, all the results that are typically reported in literature for the proton/ion transport along a beamline are not fully valid, since they are ignoring the contribution from the electrons *glued* with them.

As I described in section 3.5, our code cannot deal very well with space-charge. It works just for very few particles. To increase the number, some enhancements to the code must be done: using an octree algorithm instead of a basic N-body one [123], or switching to a PIC are two possibilities.

Another possibility is to tackle the problem from a very different point of view: what about removing electrons from the bunch, since they are also unwanted at the end of the line?

In literature there is a technique known as "Electron Clearing System", that was built at the Los Alamos Proton Storage Ring [124, 125]. The idea is to use a foil (that can be made from different materials, here for example it's made of copper) to strip away electrons and not disturb the protons, thanks to their different interactions with matter and energy deposition.

This foil can be placed right at the beginning of the beamline, as we can see from fig. B.1

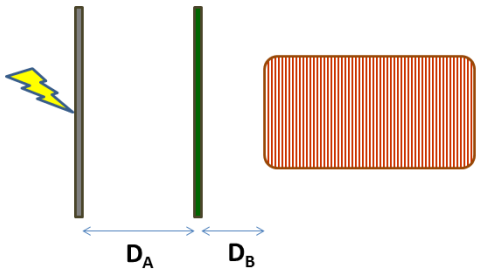

Figure B.1: The foil is at the beginning of the beamline, just after the initial acceleration phase, before the bunch enters the solenoid.

This technique was considered extremely interesting by the PHELIX experimental team at GSI (Darmstadt), so I started a work with them on simulating this topic. Carbon foils

have been already used by their Accelerator Group in previous works, even if it was with very different purpose: to "smooth" original profiles, in energy as well as transverse density, in order to obtain final spectra which are independent from the beam optics as well as from random fluctuations in the laser acceleration output [108]. Of course, in this case, the main problem is not to smooth any proton profile. On the contrary, we hope to get the minimum effects on them. Our goal is to remove effectively electrons (so that the primary electrons do not matter anymore and we do not create too many *secondary electrons* during the process).

The absorption process is well described in literature, but also the electron emission from impinging protons or ions is known, under the name of Ion-Induced Electron Emission (in our case, in particular, Proton-Induced Electron Emission). Some fundamental references [126, 127] may be useful as a basis to counter-check the results obtained. There are many kind of secondary emission due to this process, but the one that's interesting for us in this work is the *knock-on* electron production (also known as δ-rays).

B.2 Numerical simulations

The most important work on this topic has been done on the numerical point of view, because we'd like to know the prospective dependability of this idea before trying to optimize and exploit it at its best with some refinement and theoretical models.

Typically, in laser-plasma laboratories, a common used tool is SRIM [47, 48, 49], since it's designed to calculate the range of protons inside matter and so it is used to obtain the energy-depth relationship for CR39 films. For more information, see appendix A.

But since SRIM does not deal with secondary particles produced by the interaction of the primary beam with the target, just describing the energy straggling and the energy loss of the protons, it's not valid for these calculations. In order to reproduce these effects, we chose `FLUKA` (FLUktuierende KAskade) [119, 120], because it's already extensively used at GSI since it has given in those applications the best results in a benchmark with the other codes like `Geant4` [128, 129]. Unfortunately this is not the main application field of `FLUKA` and in fact we're using the software at the boundaries of its reliability: at the beginning I found some bugs and only recently I was able to circumvent those exploiting some tricks in the input file, regarding to the fact that the threshold energy for electromagnetic calculations in the software is at 1 KeV, very close to the energies that we are considering. This limit is much lower than the one for `Geant4` (10 KeV), which was another point in favor of `FLUKA` , but still it's difficult to say that the results are precise.

Another problem that we found was in the thickness of the foil used. In fact, it was so thin that, if not explicitly stated using some internal flags, the program would describe the interaction between the particles and the foil in a single step, and this, as we can understand, is very bad for statistical effects like those that we're studying.

During this work I got in contact with some `FLUKA` developers, because of the bugs that I encountered.

All of the statistical plots are calculated using the same tools that I use with our PIC and transport code. Input and output distributions are produced so that they can be interchanged between software products, so that direct cross-checking or exchanging data with tools like TraceWin [130] is possible.

In the plots B.2 and B.3 we can see the spectra for the *secondary* emission of electrons obtained by the flow of protons of 20 MeV across a foil of copper of different thicknesses.

The first studies were done checking what happens when an initial distribution of 10^4 20 MeV protons and an equal number of 10 KeV comoving electrons pass through copper

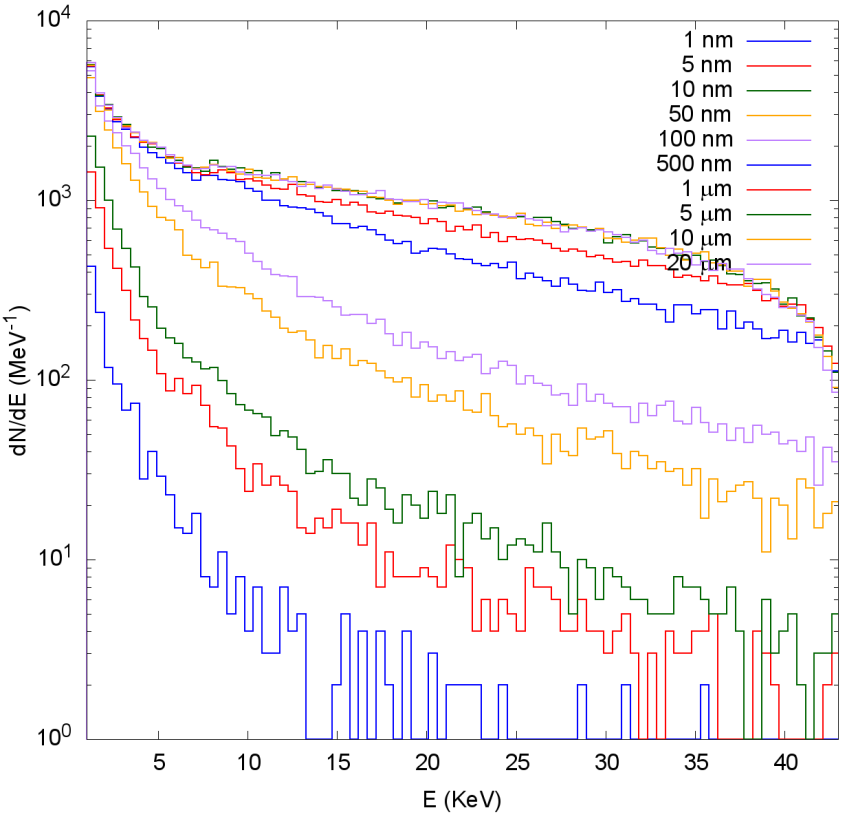

Figure B.2: Energy spectra for δ-electrons at different foil thicknesses. At the beginning, I tried to reproduce the scaling of the number of the electrons with the thickness of the target.

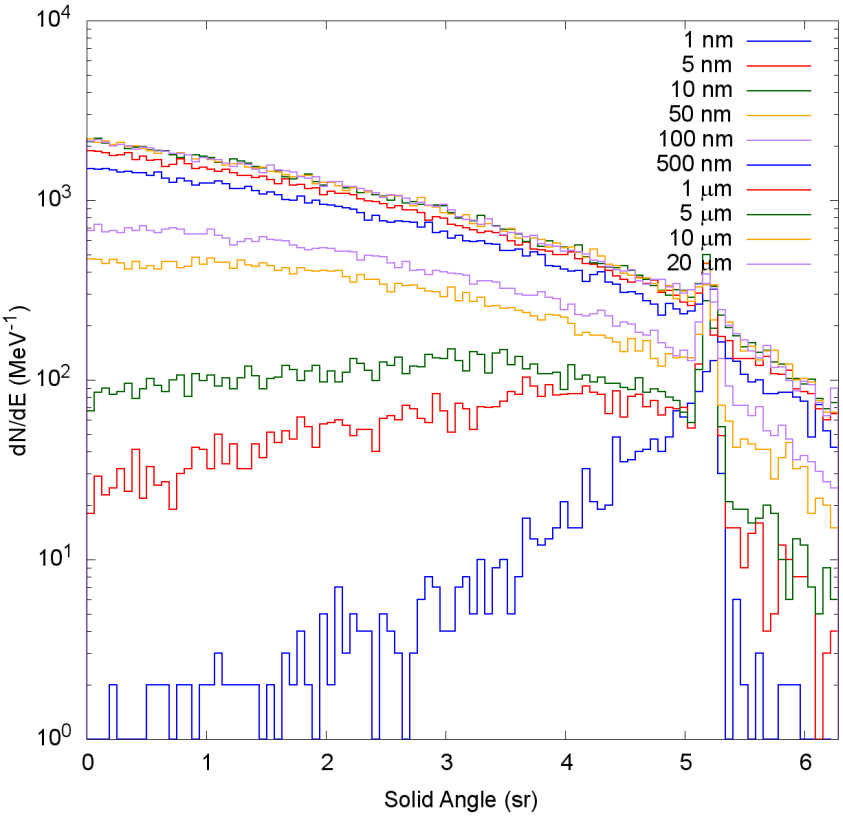

Figure B.3: Angular distribution for δ-electrons.

foils of different thicknesses. Many thicknesses were checked and here we report just those more interesting.

When the thickness increases, of course, we reach a "saturation" limit after which the number of electrons that are able to escape from the rear surface does not increase anymore, because we can have a contribution coming only from the electrons that are produced in a region near enough to the border to be able to exit. This can be seen from figure B.4. We choose the reference thickness as the thickness at which the comoving electrons would have been stopped. From the ICRU Report 37 [131], analyzed through ESTAR and PSTAR [132], we found the stopping range for the electrons and the energy straggling and losses for the protons and used that data to check results from `FLUKA` . Unfortunately, no data is given for electron energies below 10 KeV.

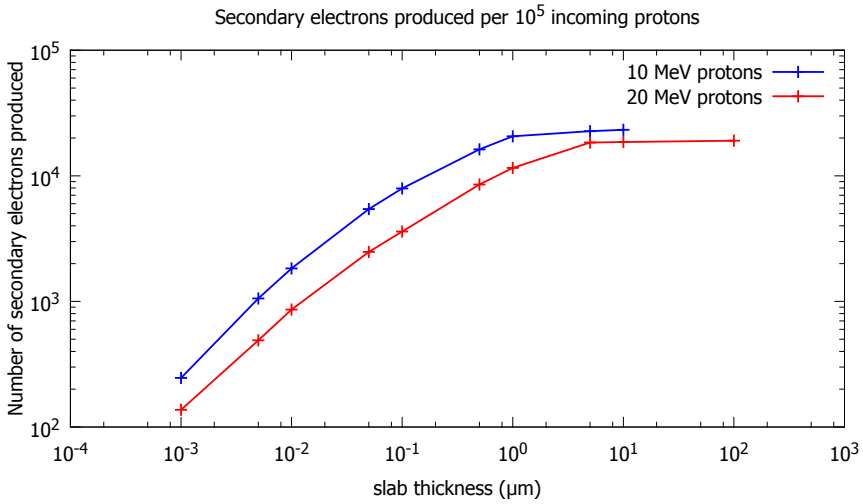

Figure B.4: With a thickness of 1 μm to stop the "primary" electrons, we're very close to the saturation regime. So we're producing nearly the maximum number of secondary electrons possible.

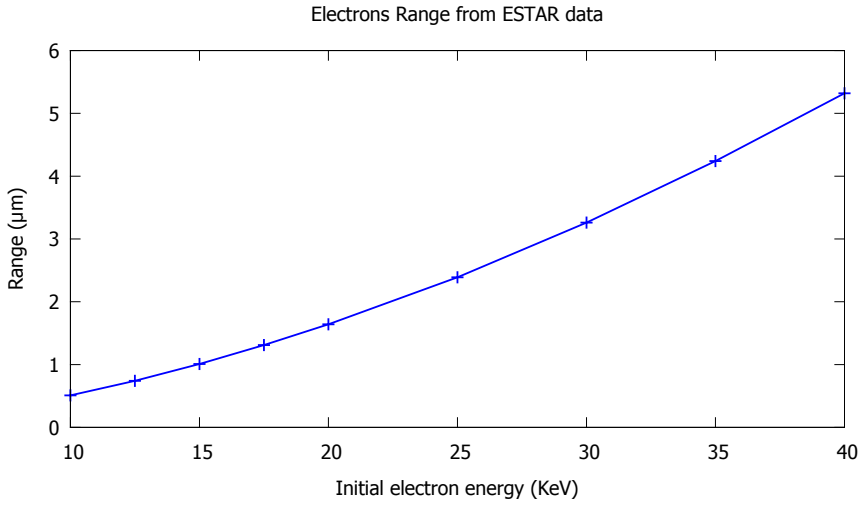

Figure B.5: A comparison between the results given by Fluka and the data plotted here, coming from ESTAR, has been done.

We found that the range for the 10 KeV electrons is $\sim 500nm$, but tuning this value with `FLUKA` we got a number that's close to 1μm.

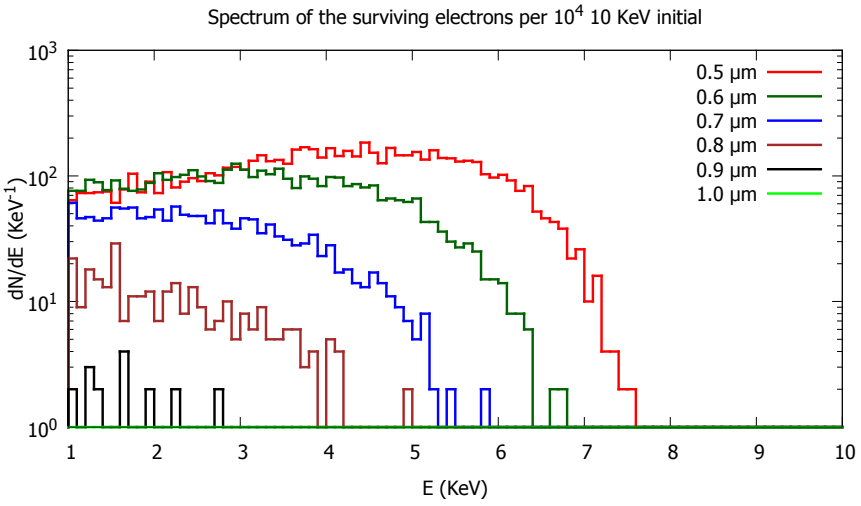

Figure B.6: Kinetic energy spectra of the outcoming electrons, with the initial distribution fixed at 10^4 electrons at 10 KeV.

The range obtained in figure B.6 is compatible with the ESTAR data. In figure B.7 we can see what happens to their angular distribution, with the initial one being a delta on *zero* divergence.

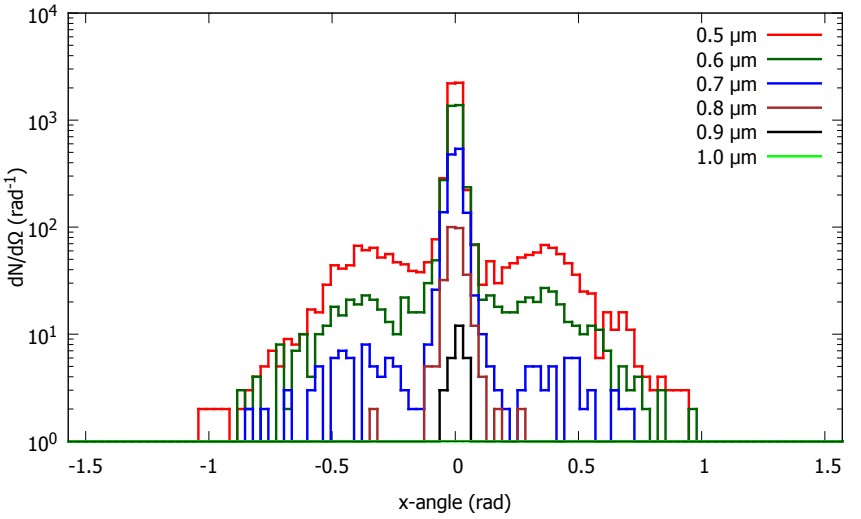

Figure B.7: Angular spectra of the outcoming electrons, with the initial distribution fixed at 10^4 electrons with no angular divergence, all with 10 KeV of kinetic energy.

On another hand we did a number of simulations, with different thicknesses, to check what happens to protons. Their initial distribution was 10^4 protons, at 20 MeV of kinetic energy, with no angular distribution. The results can be seen in figures B.8, B.9.

B.3 Results

After having confirmed the correct results for `FLUKA` for the primary protons and the secondary electrons, we choose a foil thickness of 1 μm and see what happens to a realistic TNSA input proton-electron mixed bunch. As expected to protons nothing happened,

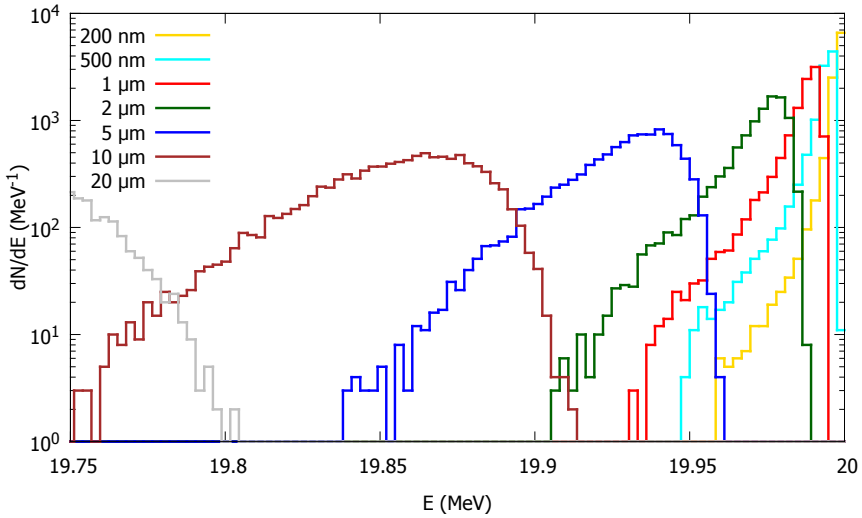

Figure B.8: Kinetic energy spectra of the outcoming protons. Initial kinetic energy is 20 MeV

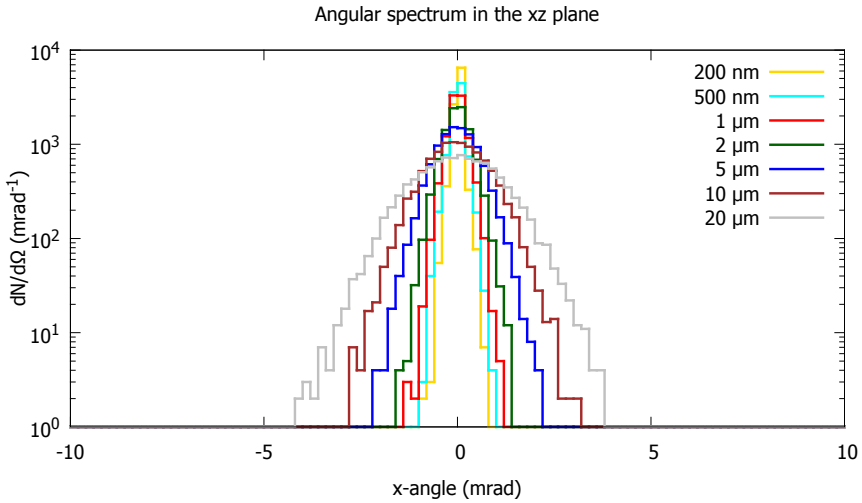

Figure B.9: Angular spectra of the outcoming protons, at 20 MeV.

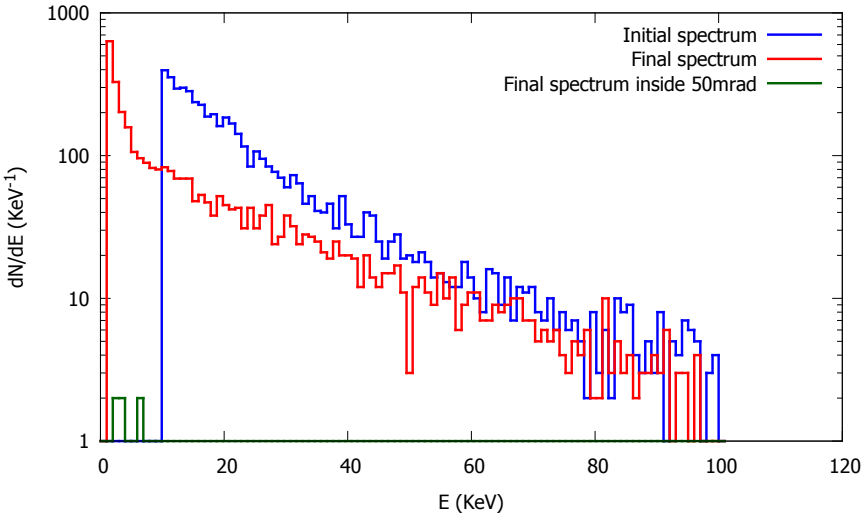

Figure B.10: Electrons energy spectra before and after 1 μm copper foil - the final spectrum is composed of both surviving electrons and newly created ones. The initial spectrum was cut above 10 KeV because from previous results we know that electrons below this threshold would have not survived the foil

while the results on the electron bunch is described in figures B.10 and B.11.

As can be seen from Figure B.10, using this copper foil it's not possible to completely suppress the electrons inside the bunch.

If the collaboration will proceed, we will focus on the electrons that at the exit of the foil still have an energy around the one required to be considered *comoving* with the original bunch. This will be an important point, because if the proton trapping is still very effective, we could see other effects on the bunch which at the moment we had not considered. In fact, what could happen is that electrons get re-accelerated by the protons because of their charge interactions with them, causing another loss in the energy of the original proton bunch.

After this experience, it became absolutely important to better understand the topic of the space-charge for a proton bunch generated by a laser-plasma interaction. It's a strong motivation to continue the work on this routine in our `Propaga` transport code

In this way we will be able to solve the problem of understanding how this co-moving electrons can be modeled and also learn if space-charge effects are really non-trivial also in the region 2 cm away from the target, where we always thought that charge was diluted enough to not matter anymore.

The main result obtained from these simulations is that these foils should at least not degrade the original properties of the proton bunch, while suppressing the undesired co-moving electrons at the interesting energy analyzed and at the same time not release the same numbers of secondary electrons in the same energy range.

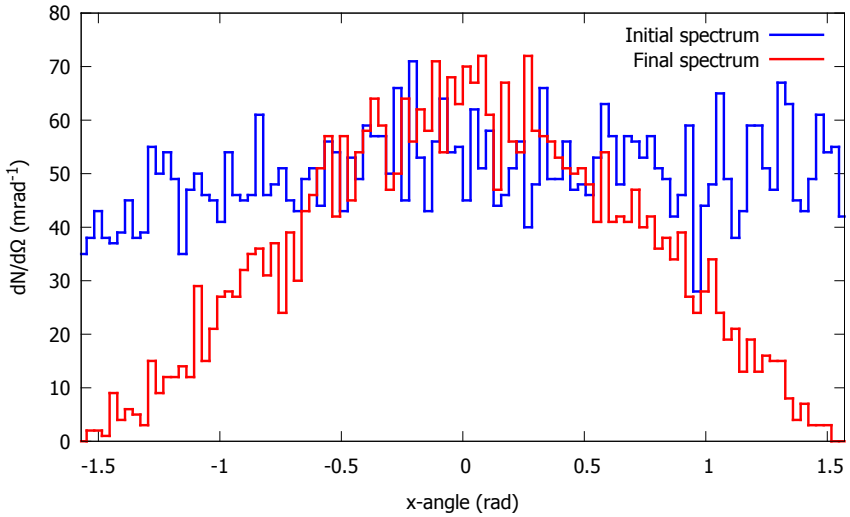

Figure B.11: Electrons angular spectra before and after 1 μm copper foil - the final spectrum is composed of both surviving electrons and newly created ones. The initial spectrum was cut above 10 KeV because from previous results we know that electrons below this threshold would have not survived the foil

C

Proton and ion acceleration at INFN

C.1 LILIA

This activity has been considered of great interest for INFN. At LNF (Laboratori Nazionali di Frascati) three years ago it was decided to install a laser, FLAME (Frascati Laser for Acceleration and Multidisciplinary Experiments), to pursue research on laser-plasma acceleration.

This laser is a Ti:Sa device, with a nominal design maximum power of 300 TW (6 J in a 20 fs pulse). The laboratory in which it has been installed is unique in the world because it eases the possibility to couple the laser with an electron LINAC, SPARC (Sorgente Pulsata Auto-amplificata di Radiazione Coerente), so that the main research tasks revolve around electron acceleration. But since the possibility is there (the intensity can reach 10^{21} W/cm^2, with a contrast up to 10^{10}), an experiment of light ion acceleration through laser acceleration with thin targets has been proposed and funded. The aim of the LILIA (Laser Induced Light Ion Acceleration) experiment is to study, design and verify a scheme which foreseen the production, the characterization and the transport of a proton beam towards a stage of post-acceleration [133]. Much of my PhD work was devoted to this experiment and the first peer-reviewed publication related to this project came out from our group in 2013 [85].

C.2 ELIMED

Recently, at LNF was reinstated that the main research topic with FLAME has to be electron acceleration and so the work for the LILIA project was merged with a newborn ELI-related project inside INFN.

ELI (Extreme Light Infrastructure) will be a new scientific infrastructure devoted to European research in lasers' field, dedicated to the investigation and applications of laser-matter interaction at the highest intensity level [134]. It will be built around four pillars and three local branches:

- Attosecond science, designed to conduct temporal investigation of electron dynamics in atoms, molecules, plasmas and solids at the scale of a billionth of a billionth of a second, to be developed in the Hungarian branch

- Laser-based nuclear physics, to study new nuclear spectroscopy, new photonuclear physics, among many other laser-target models, to be developed at the Romanian branch

- Ultra high field science, where quantum effects could arise from the interaction of the laser beam with the vacuum
- High energy beam science, related to the development and use of ultra-short pulses of high-energy particles and radiation obtained from laser-plasma acceleration methods, that is the most advanced branch, in terms of practical infrastructures already built, and that is being built in Prague.

Inside the ELI-Beamlines that is being built in Prague, there's the ELIMAIA (ELI Multi-disciplinary Applications of laser Ion Acceleration) beamline that will host many different projects. One is ELIMED (ELI-beamlines MEDical and multidisciplinary applications), a project that was born inside INFN-LNS (Laboratori Nazionali del Sud) but that now has become the main research project for laser-driven ion acceleration in Italy and that include many different local section such as, in fact, Bologna.

Papers

An up to date version can be found online[1].

1. Transport and energy selection of laser generated protons and post-acceleration with a compact linac

by S. Sinigardi, G. Turchetti, P. Londrillo, F. Rossi, D. Giove, C. De Martinis, M. Sumini
Published on Physical Review Special Topics-Accelerators and Beams 16 (3), 031301 (2013)
(doi: 10.1103/PhysRevSTAB.16.031301)

2. High quality proton beams from hybrid integrated laser-driven ion acceleration systems

by S. Sinigardi, G. Turchetti, F. Rossi, P. Londrillo, D. Giove, C. De Martinis, P. R. Bolton
accepted for publication on Nuclear Instruments and Methods in Physics Research Section A: Accelerators, Spectrometers, Detectors and Associated Equipment
(doi:10.1016/j.nima.2013.10.080)

3. Post-acceleration of laser driven protons with a compact high field linac

by S. Sinigardi, P. Londrillo, F. Rossi, G. Turchetti, P. R. Bolton
Published on Proc. SPIE 8779, Laser Acceleration of Electrons, Protons, and Ions II; and Medical Applications of Laser-Generated Beams of Particles II; and Harnessing Relativistic Plasma Waves III, 87791J (2013)
(doi:10.1117/12.2017235)

4. Advanced strategies for ion acceleration using high power lasers

by A. Macchi, A. Sgattoni, S. Sinigardi, M. Borghesi, M. Passoni, accepted for publication on Plasma Physics and Controlled Fusion
Published on Plasma Phys. Control. Fusion 55, 124020 (2013)
(doi:10.1088/0741-3335/55/12/124020)

[1] `http://scholar.google.com/citations?user=Pogp61AAAAAJ`

5. The LILIA experiment: Energy selection and post-acceleration of laser generated protons

by G. Turchetti, S. Sinigardi, P. Londrillo, F. Rossi, M. Sumini, D. Giove and C. De Martinis
Published on AIP Conf. Proc. 1507, pp. 820-824 (2012)
(doi:10.1063/1.4773804)

6. Towards robust algorithms for current deposition and dynamic load-balancing in a GPU particle in cell code

by F. Rossi, P. Londrillo, A. Sgattoni, S. Sinigardi and G. Turchetti
Published on AIP Conf. Proc. 1507, pp. 184-192 (2012)
(doi:10.1063/1.4773692)

7. Protons Acceleration by CO2 Laser Pulses and Perspectives for Medical Applications

by P. Londrillo, G. Servizi, A. Sgattoni, S. Sinigardi, M. Sumini and G. Turchetti
Published as a chapter in the "CO2 Laser - Optimisation and Application" book by Dan C. Dumitras, (2012)
(ISBN 978-953-51-0351-6) (doi:10.5772/38882)